Dissertation

Beat-to-Beat Behavior of Atrial Activation Sequences Under Impaired Conduction Conditions - Macroscopic and Microscopic Aspects

submitted by

Dipl.-Ing.
Robert ARNOLD

for the Academic Degree of

Doctor of Medical Science
Dr.scient.med.

at the

Medical University of Graz
Institute of Biophysics

under the supervision of

Ao.Univ.-Prof. Dipl.-Ing. Dr.techn. Ernst HOFER

Graz, June 2013

Eidesstattliche Erklärung

Ich erkläre ehrenwörtlich, dass ich die vorliegende Arbeit selbstständig angefertigt und abgefasst, und jene Personen und Institutionen, die am Zustandekommen der Forschungsdaten beteiligt waren, namentlich genannt habe. Andere als die angegebenen Quellen habe ich nicht verwendet und die den benutzten Quellen wörtlich oder inhaltlich entnommenen Stellen habe ich als solche kenntlich gemacht. Die Arbeit an der Dissertation und daraus entstandener Publikationen wurde gemäß den Regeln der „Good Scientific Practice“ durchgeführt.

Statutory Declaration

I hereby declare that this thesis is my own original work and that I have fully acknowledged by name all of those individuals and organisations that have contributed to the research for this thesis. Due acknowledgement has been made in the text to all other material used. Throughout this thesis and in all related publications I followed the guidelines of “Good Scientific Practice”.

Graz, _____ _____

Date Signature

Abstract

Atrial flutter and atrial fibrillation have evolved to one of the leading cardiovascular diseases over the past decades and their prevalence is expected to strongly increase. The cavotricuspid isthmus (CTI), a subregion in the right atrium, is seen as a potential arrhythmogenic substrate and is therefore a preferential target for clinical catheter ablation procedures. Structure of the CTI is complex at a macroscopic and microscopic level and determines the excitation pathways of electrical activation. These structural complexities lead to characteristic distributions of extracellular potentials and under certain circumstances to fractionation of electrograms within the CTI. At elevated heart rates additionally functional heterogeneities arise, resulting in changes of activation patterns. From a clinical point of view the detection of local conduction block preceding arrhythmias is of particular interest. The aim of this work was to characterize the complex macroscopic structures within the CTI, investigate distribution of extracellular signals and activation spread during normal sinus rhythm of the heart, and to explore the changes of local activation patterns at increased heart rates. Therefore, electrophysiological experiments with tissue preparations from rabbits and guinea pigs were carried out. Comprehensive morphological characterization of the CTI yielded representative topologies comparable to human atria which could facilitate the development of rule-based computer models of electrical excitation spread in this region. Morphology was combined with multisite extracellular recordings to electro-anatomical maps of the CTI. The influence of macroscopic and microscopic structures on excitation spread at varying heart rates was studied by applying electrical pacing with dynamic protocols. The results shown in this work suggest that it is possible to predict upcoming conduction block and to identify substrates of increased heterogeneity of conduction by means of adequate pacing techniques before reaching local conduction block and therefore without inducing atrial flutter or fibrillation.

Kurzfassung

Vorhofflimmern und Vorhofflattern haben sich in den letzten Jahrzehnten zur häufigsten kardialen Herzrhythmusstörung entwickelt. Der cavotricuspidale Isthmus (CTI) des rechten Vorhofes wird als potentiell arrhythmogenes Substrat angesehen und ist daher ein bevorzugtes Ziel für Katheterablation. Der CTI zeigt eine komplexe Mikro- und Makrostruktur, welche die elektrische Erregungsausbreitung bestimmt. Diese Komplexitäten bilden sich in der Verteilung von Leitungsparametern und durch mögliche Fraktionierung von Elektrogrammen ab und charakterisieren die Leitungspfade im CTI. Bei erhöhter Herzfrequenz kommt es durch das Auftreten von zusätzlichen funktionellen Heterogenitäten zu Veränderungen der Erregungsausbreitung. Aus klinischer Sicht ist die Lokalisierungn von Leitungsblock, also das Zusammenbrechen der lokalen Erregungsausbreitung, von großem Interesse. Ziel dieser Arbeit war es, in elektrophysiologischen Experimenten mit Tiergewebepräparaten von Kaninchen und Meerschweinchen die makroskopische Geometrie und Topologie des Fasernetzwerkes im CTI zu beschreiben, die Erregungsausbreitung während des Sinusrhythmus zu charakterisieren und deren Veränderung bei Erhöhung der Herzfrequenz zu untersuchen. Die umfassende makrostrukturelle Untersuchung von Hasenherzen in dieser Arbeit ermöglicht eine regelbasierte Beschreibung des CTI, dessen Topologie näherungsweise der des menschlichen Herzens entspricht. Aus den Morphometriedaten und den korrespondierenden räumlich verteilten Elektrogrammen wurden elektro-anatomische Abbildungen erstellt. Der Einfluss von Mikrostruktur bei steigender Herzfrequenz auf elektrische Signale und die Veränderungen in den lokalen Aktivierungsmustern wurden mittels elektrischer Stimulation von Gewebepräparaten untersucht. Durch unterschiedliche zeitliche Dynamik der Stimulationsprotokolle wurden funktionelle Heterogenitäten hervorgerufen und analysiert. Die Ergebnisse dieser Arbeit legen nahe, dass eine Prognose von lokalem Leitungsblock aus extrazellulären Leitungsparametern und damit eine Identifizierung von potentiell arrhythmogenen Substraten ohne das Auslösen einer Arrhythmie möglich sind.

Contents

Nomenclature

Abbreviations

AP	action potential
APD	action potential duration
AR	anisotropy rate
ATP	adenosine triphosphate
BCL	basic cycle length
CFAE	complex fractionated atrial electrogram
CI	central isthmus
CNF	cardiac near field
CS	coronary sinus
CT	crista terminalis
CTI	cavotricuspid isthmus
DAQ	data acquisition
DD	diagonal distance
EDD	early diastolic depolarization
ER	Eustachian ridge
ERP	effective refractory period
EV	Eustachian valve
FO	fossa ovalis
FOV	field of view
GME	glass microelectrode
GUI	graphical user interface
ILI	infero-lateral isthmus
IVC	inferior vena cava
LAT	local activation time
LP	longitudinal propagation
NCX	Na^{+}-Ca^{2+}-exchanger
NPT	non pectinate tissue
OS	overshoot
PCL	pacing cycle length

(*table continues*)

(*continued*)

PM	papillary muscle
PSI	paraseptal isthmus
PXI	PCI extension for instrumentation
PectM	pectinate muscle
PRD	pacing rate dependency
RAA	right atrial appendage
ROI	region of interest
RP	resting potential
SAN	sinoatrial node
SM	significance matrix
SVC	superior vena cava
TCV	tricuspid valve
TP	transversal propagation
VB	vestibule
VL	vector loop

Constants

R	universal gas constant, $8.3145\,\mathrm{J\,mol^{-1}\,K^{-1}}$
F	Faraday constant, $96\,485.3365\,\mathrm{C\,mol^{-1}}$

Symbols

V_m	transmembrane voltage
C_m	membrane capacitance
I_f	"funny" current
Φ	electric potential
$\mathbf{E}$	vector of cardiac near field strength
E_{max}	magnitude of cardiac near field strength
$\mathbf{LCV}$	vector of local conduction velocity
LCV	magnitude of local conduction velocity
α_{LCV}	propagation angle of local conduction velocity
$\alpha_{E,max}$	angle of magnitude of cardiac near field strength
$\alpha_{E,LAT}$	angle of cardiac near field strength at LAT
a	waveform symmetry
t_{depol}	depolarization duration
V_{rest}	resting membrane potential
V_{OS}	overshoot potential
S_b	index of conduction block
VAR_d	displacement variance

List of Figures

List of Tables

1. Introduction

Atrial flutter and atrial fibrillation have evolved to one of the major cardiac diseases over the past decades because of increasing life expectancy and the associated changes in cardiac microstructure with age. In 2010 over 6 million citizens in the European Union suffered from this disease and numbers are expected to double in the next 50 years (EHRA et al., 2010).

1.1. Motivation

The macroscopic structural complexity of the right atrium with its branching, merging, and crossing of individual muscle fibers determines the excitation pattern of a propagating electrical activation wavefront. Under impaired conditions for propagation of this excitation wavefront, e.g. at elevated heart rate, the excitation pattern can change completely and arrhythmias may arise. Myocardial structure is also complex at a microscopic level and changes in microstructure are altering the excitation patterns. Therefore, the structural complexity at both a macroscopic and a microscopic level, along with functional parameters of the cardiac tissue influence the propagation of electrical activation wavefronts.

1.2. Aim of this work

This work focuses on the modulation of the heart rate by means of electrical stimulation to reproduce impaired conditions for propagation of excitation wavefronts. Of particular interest for arrhythmogenesis is the dispersion of activation patterns with

increasing heart rate. From a clinical point of view the evolution of parameters of conduction before conduction block arises is vitally important since local conduction block is often associated with arrhythmogenesis.
Therefore, sophisticated protocols for modulation of the heart rate were applied in electrophysiological experiments and appropriate signal analysis algorithms for characterization of dispersion and beat-to-beat behavior of activation patterns were implemented.

Hypothesis

1. During sinus rhythm macroscopic and microscopic structures determine the pathways for excitation spread. Hence, these structures generate characteristic excitation patterns in the right atrium.

2. At elevated heart rates functional heterogeneities develop throughout the right atrium and structural heterogeneities gain greater influence on excitation spread. Especially at critical heart rates, i.e close to conduction failure, parameters of excitation spread change dramatically and thus enable the prediction of upcoming conduction block.

Part I.

Electrophysiological Background, Materials, and Methods

2. Cardiac Electrophysiology

This chapter intends to give an overview of basic mechanisms and phenomena in bioelectricity, structure and function of cardiac muscle cells, coupling between cells, propagation of electrical activation in cardiac tissue, and electrophysiological measurement methods.

2.1. Bioelectric Phenomena

If two solutions with different concentrations of a substance are brought together, a flow of particles due to the concentration gradient results. This movement of particles is closely related to Brownian motion and is described by Fick's first law:

$$J_{diff}(x) = -DA\left(\frac{\partial c}{\partial x}\right) \tag{2.1}$$

where $J_{diff}(x)$ is the flow in $\mathrm{mmol\,s^{-1}}$ in direction x, D is the diffusivity constant in $\mathrm{m^2\,s^{-1}}$, A is the regarding cross-section area in $\mathrm{m^2}$, and c is the concentration in mmol. In an electrical field a force is exerted on charged particles. The flow of particles is described by Ohm's law:

$$J_{el}(x) = -cDA\frac{zF}{RT}\frac{d\varphi}{dx} \tag{2.2}$$

where $J_{el}(x)$ is the flow in $\mathrm{mmol\,s^{-1}}$ in direction x, c is the concentration in mmol, D is the diffusivity constant in $\mathrm{m^2\,s^{-1}}$, A is the regarding cross-section area in $\mathrm{m^2}$, z is the valence, F is the Faraday constant, R is the universal gas constant, T is the temperature in K, and φ is the electric potential.
In an arrangement of two compartments with ions at different concentrations separated by a semipermeable membrane (i.e. the membrane is only permeable for one ion species)

the diffusive flow across the membrane is accompanied by a net charge transport. Hence, a potential difference is generated over the membrane which counteracts the ion movement. At steady state the electrochemical potential μ is equal at both sides of the membrane and the potential across the membrane can be described by the Nernst equation:

$$E = \varphi_2 - \varphi_1 = \frac{RT}{zF} \ln \frac{c_1}{c_2} \tag{2.3}$$

where E is the potential difference over the membrane in V, z is the valence of the ion species, and c_1 and c_2 are the ion concentrations in mmol.
Biological membranes are permeable for multiple ion species and therefore the potential difference across the membrane has to be calculated using the Goldmann-Equation:

$$V_m = \frac{RT}{F} \ln \frac{\sum P_\nu c_\nu^o + \sum P_\mu c_\mu^i}{\sum P_\nu c_\nu^i + \sum P_\mu c_\mu^o} \tag{2.4}$$

with P, the permeability coefficient in $\mathrm{cm\,s^{-1}}$. Index ν stands for cations, μ for anions, i for inside, and o for outside. It has to be noted that the Goldmann-Equation does not take into account active transport mechanisms like the $\mathsf{Na^+}$-$\mathsf{K^+}$-pump (see Section 2.2.2).

2.2. Biological Cell

Biological cells are enclosed by a plasma membrane which separates the intracellular cytosol and the extracellular space. The membrane is formed by phospholipids which have a hydrophobic tail and a hydrophilic head. In an aqueous solution these lipids spontaneously form double layers of $4-5\,\mathrm{nm}$ thickness with their hydrophilic heads on the outside and hydrophobic tails in between (see Figure 2.1). The total thickness of the plasma membrane including proteins is $6-10\,\mathrm{nm}$ (Adam et al., 2003). Electrically the plasma membrane represents a parallel plate capacitor with very high capacitance of $\approx 1\,\mu\mathrm{F\,cm^{-2}}$.

Ion concentrations are different between intracellular and extracellular space. Given the concentrations in Table 2.1 and using the Goldmann-equation (2.4) the transmembrane potential can be calculated. The membrane potential under steady state conditions is referred to as resting potential (RP) and is approximately $-90\,\mathrm{mV}$ for cardiac muscle cells. This value roughly corresponds with the Nernst-potential of $\mathsf{K^+}$. Voltage shift

from RP to more positive values is called depolarization whereas shift to more negative potentials is called hyperpolarization.

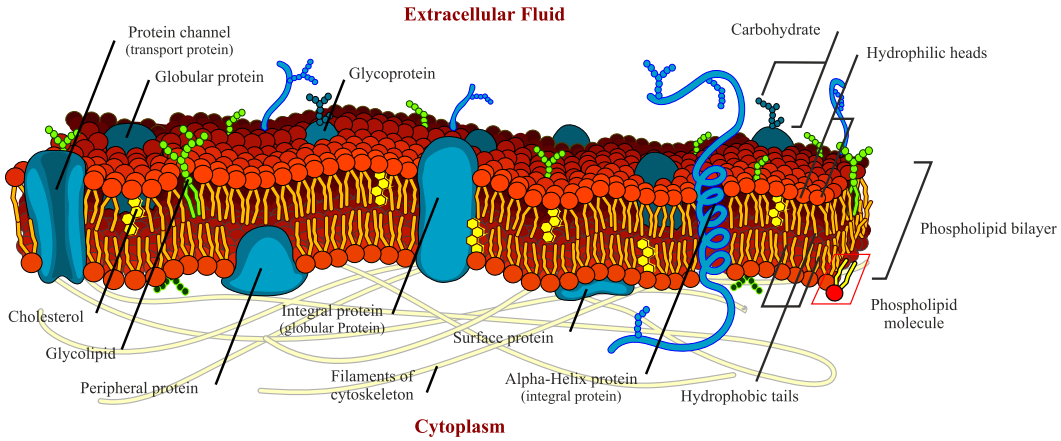

Figure 2.1.: Structure of the cell membrane. A phospholipid double layer encloses the intracellular compartment. Ions are exchanged through protein channels. Adapted from Ruiz (2007).

Table 2.1.: Intra- and extracellular concentrations of ions in a muscle cell. A^- stands for "large anions" in humans. From Schmidt et al., 2000.

Ion	Intracellular	Extracellular
Na^+	$12\,\mathrm{mmol\,l^{-1}}$	$145\,\mathrm{mmol\,l^{-1}}$
K^+	$155\,\mathrm{mmol\,l^{-1}}$	$4\,\mathrm{mmol\,l^{-1}}$
Ca^{2+}	$0.001-0.01\,\mathrm{mmol\,l^{-1}}$	$2\,\mathrm{mmol\,l^{-1}}$
Cl^-	$4\,\mathrm{mmol\,l^{-1}}$	$120\,\mathrm{mmol\,l^{-1}}$
HCO_3^-	$8\,\mathrm{mmol\,l^{-1}}$	$27\,\mathrm{mmol\,l^{-1}}$
A^-	$155\,\mathrm{mmol\,l^{-1}}$	$5\,\mathrm{mmol\,l^{-1}}$
Resting Membrane Potential	$-90\,\mathrm{mV}$	$0\,\mathrm{mV}$

2.2.1. Ion Channels

The cell membrane is essentially permeable only for hydrophobic molecules and dissolved gases like O_2 and CO_2. Charged molecules and ions cannot be exchanged via diffusion but are transported through integral membrane proteins embedded in the cell membrane (Figure 2.2a). These proteins form channels through which ions and molecules can pass down their concentration gradient. This transport is very specific for one ion species per channel.

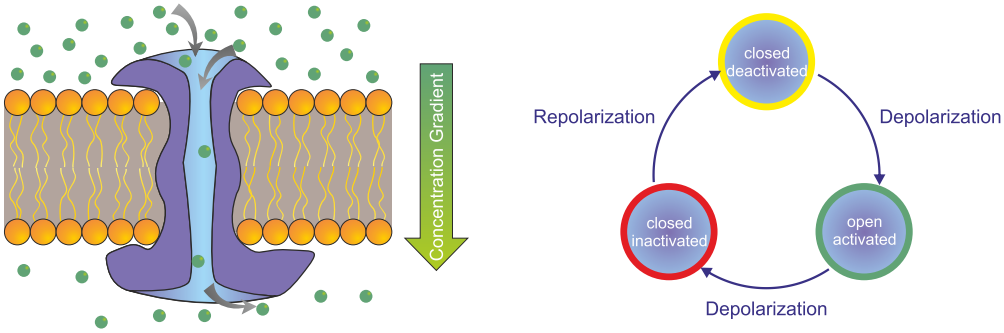

(a) Ion channel **(b)** Ion channel states

Figure 2.2.: Ion channels. (a) Charged ions and molecules can pass the membrane through integral membrane proteins down their concentration gradient. (b) The channels can be in 3 different states: open/activated, closed/deactivated, and closed/inactivated.

Ion channels are gated, i.e. they open or close under specific conditions. Depending on the mechanism that initiates opening or closing of a channel, ion channels can be classified:

- **Voltage-gated:** The membrane proteins are sensitive to the transmembrane voltage and open or close according to it.
- **Ligand-gated:** Channels open or close when a ligand (neurotransmitter) binds to a receptor on the plasma membrane.
- **Stretch-activated:** Important in cardiac tissue are stretch activated channels, which open or close when mechanical force is exerted on the cell (Crozatier, 1996; Hagiwara et al., 1992; Zeng et al., 2000).

Voltage-gated ion channels like the Na^+-channel can be in 3 different states: (i) open and activated, (ii) closed and deactivated, and (iii) closed and inactivated. The ion channels are conducting in the open/activated state and non-conducting in the closed states. In the deactivated state channels are closed but can become conducting. Inactivation refers to a state in which channels are closed and are not perceptible for opening. This is the basic mechanism for refractoriness (cf. Section 2.2.3). Figure 2.2b depicts a simplified scheme of the transition between states. Depolarization enhances transition from closed/deactivated to open/activated. Further depolarization changes the state to closed/inactivated. Transition back to closed/deactivated results from repolarization. The mechanisms and kinetics of transitions varies between ion channels and channel subtypes (Bähring and Covarrubias, 2011). Activation of voltage-gated ion channels

can also be in response to hyperpolarization of the cell membrane like for I_f, a K^+ channel in pacemaker cells (Grant, 2009). Pacemaker cells are described in Section 2.5. Ion channels can further be classified by their temporal characteristics into fast and slow channels and their preferred direction of current flow (rectification).

2.2.2. Active Transport

The RP of a cell is not only maintained by selective permeability of the cell membrane, but also by active transport mechanisms which move ions against their concentration and/or electrical gradient across the cell membrane. The Na^+-K^+-pump moves 3 sodium ions out of the cell and 2 potassium ions into the cell (Figure 2.3). This transport consumes energy in form of adenosine triphosphate, ATP. Secondary active transport mechanisms like the Na^+-Ca^{2+}-exchanger (NCX) do not consume ATP. NCX moves 3 sodium ions into the cell and 1 calcium ion out of the cell by using the potential energy of the Na^+-gradient.

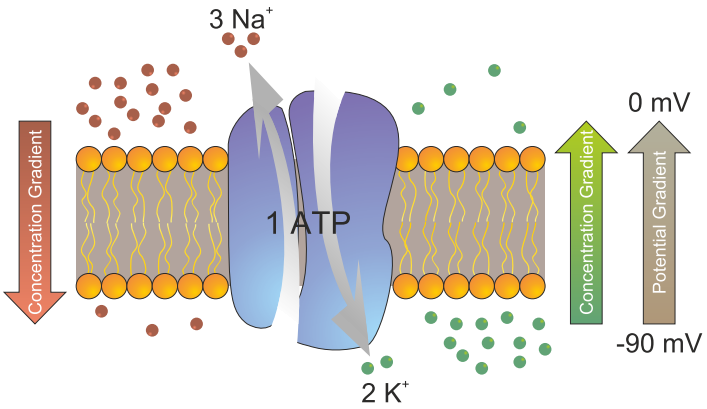

Figure 2.3.: Function of the Na^+-K^+-pump. 3 sodium ions (red) are moved out of the cell and 2 potassium ions (green) are moved into the cell using ATP. Transport is against concentration gradients.

2.2.3. Action Potential

As described above the RP is kept constant in a cell. For cardiac muscle cells (cardiomyocytes) RP typically is $-90\,\text{mV}$. This is roughly the Nernst potential of K^+ since at steady state the cell membrane is essentially permeable for K^+ only. If the membrane is depolarized above a threshold value (typically 20 mV above RP), a cascade of transient

ionic currents is started. The resulting time course of the transmembrane potential has a characteristic shape which is referred to as action potential, AP. Cardiomyocytes have a unique AP because of the presence of Ca^{2+} channels which elongate the AP. Here, only APs of cardiomyocytes are described. Figure 2.4 shows the characteristic time course of a ventricular cardiomyocyte's AP.

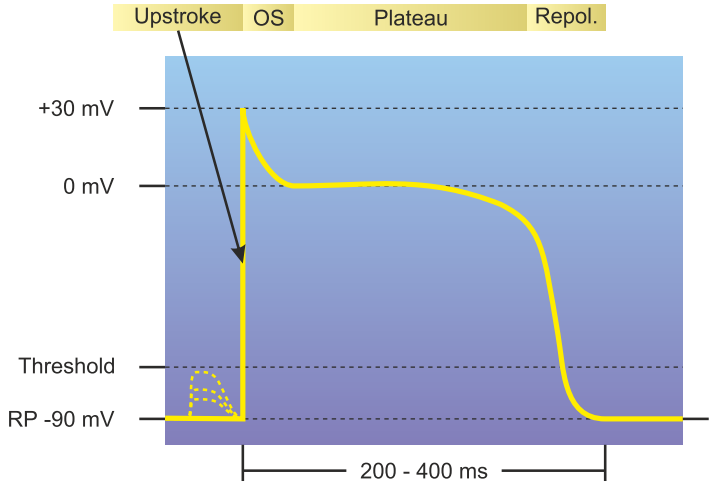

Figure 2.4.: Ventricular action potential. Depolarization above a threshold starts an action potential. The membrane rapidly depolarizes and transmembrane voltage reaches positive values (overshoot OS). Ca^{2+} influx causes the plateau phase. After 200 – 400 ms the membrane has completely repolarized to the resting potential (RP). Only stimuli above the threshold can initiate an action potential (dotted curves).

The AP can be divided into 4 phases:

- **Upstroke:** Sodium channels increase their conductivity and the inward flow of Na^{+} rapidly depolarizes the membrane.
- **Overshoot:** The membrane voltage reaches positives values of approximately 30 mV.
- **Plateau:** After an initial short repolarization phase (transient outward K^{+} currents) Ca^{2+} channels open and the resulting inward current keeps the membrane voltage constant.
- **Repolarization:** Activation of rectifying K^{+} channels repolarizes the membrane to RP.

The characteristic plateau phase of cardiac action potentials evokes an important property of cardiac APs, the refractoriness. Prolonged depolarization leads to inactivation

of Na^+ channels (Ulbricht, 2005) and thus to a phase of non-excitability. This refractory period prevents the cardiac tissue from early re-activation.
It has to be noted that the shape of the AP varies in different regions of the heart and in different species (Shih, 1994).

2.2.4. Cell Coupling

Cells are connected to each other via gap junctions. These channels directly connect the cytoplasm of 2 cells allowing ions and molecules to be exchanged over a low-resistance pathway. Gap junction connexons are made up of 6 subunits (connexins). The majority of connexins expressed in the heart are: connexin43 (Cx43), connexin40 (Cx40), and connexin45 (Cx45). Expression is different for various types of cardiomyocytes, e.g. the sinoatrial node (SAN) mainly expresses Cx45 (Monfredi et al., 2010).

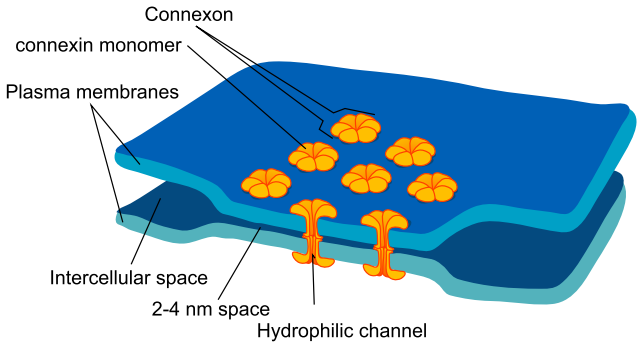

(a) Gap Junction. Adapted from Ruiz (2006b).

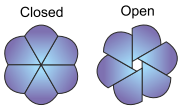

(b) Gap Junction States

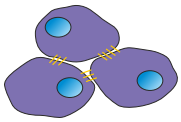

(c) Cell Coupling

Figure 2.5.: Gap Junctions. (a) Adjacent cells are connected by connexons which allow low-resistive flow of ions. (b) Gap junctions can be in two states: open and closed. (c) Neighboring cells are connected with multiple gap junctions.

2.3. Propagation of Activation

2.3.1. Continuous Conduction

In an arrangement of cells, the activation of one cell can depolarize neighboring downstream cells by ionic currents through gap junctions. Classically, a linear arrangement

of cardiomyocytes is seen as electrical syncytium and propagation is described by the cable equation:

$$C_m \frac{\partial V_m}{\partial t} + I_{ion} = \frac{a}{2r_i} \frac{\partial^2 V_m}{\partial x^2} \tag{2.5}$$

where C_m is the membrane capacitance, V_m is the transmembrane potential (function in space and time), I_{ion} is the ionic current, a is the fiber radius, and r_i is the average axial resistance (cytosol plus gap junction resistance).

2.3.2. Discontinuous Conduction

The cellular architecture of the myocardium with individual myocytes coupled via gap junctions requires a more comprehensive model for propagation of activation. A propagating wavefront will interact with boundaries at a macroscopic level (branching and merging of individual muscle fibers, vessels, fibrotic tissue) and a microscopic level (cell boundaries) and impulse propagation therefore will become discontinuous. The following basic principles cause discontinuous conduction:

- **Sites of Collision:** If a propagating wavefront approaches the end of an excitable cable (sealed end) or two wavefronts approach each other (collision), the axial current is reflected at the boundary and therefore is available for depolarizing the local membrane capacitance. This results in increased conduction velocity and changes in the shape of the transmembrane voltage (Goldstein and Rall, 1974; Spach and Kootsey, 1985).
- **Sites of Dispersion:** At sites where the tissue diameter suddenly increases the axial current has to depolarize a large number of downstream cells. Impulse propagation is successful only if the local transmembrane current (current source) is large enough to depolarize the local and the downstream membrane capacitance above threshold (current sink). The dispersion of depolarizing current results in conduction slowing and reduces action potential upstroke velocity. Propagation fails if the number of downstream cells becomes too large (current-to-load mismatch) (Rohr and Salzberg, 1994).
- **Repetitive Sites of Collision and Dispersion:** In the myocardium sites of (partial) collision and sites of dispersion can be repetitive, e.g. repetitive occurrence of gap junctions at a cellular level (Kléber and Rudy, 2004; Wang and Rudy, 2000).

2.3.3. Anisotropic Conduction

In a two dimensional arrangement of cells propagation differs for longitudinal propagation (LP) and transversal propagation (TP). The anisotropy ratio AR, i.e. the ratio of longitudinal conduction velocity CV_L and transversal conduction velocity CV_T, is not uniformly distributed over the heart. AR ranges from ∼10 in the terminal crest to ∼2 in the ventricles (Kléber and Rudy, 2004). The predominant determinants of anisotropy are:

- **Gap Junction Distribution:** In the adult myocardium gap junctions are mainly distributed at the end of the cells and therefore the resistance for impulse propagation is lower in longitudinal direction. (Hoyt et al., 1989; Severs et al., 2008; Spach, Heidlage, et al., 2000).
- **Cell Geometry:** Adult cardiomyocytes have an elongated shape with an relatively constant length-to-width ratio (Valderrábano, 2007). For TP the excitation wavefront has to pass a higher number of cell borders with a low number of gap junctions (c.f. above).
- **Cell Size:** It has been shown by Spach, Heidlage, et al. (2000) that cell size is of great importance for differences in longitudinal and transversal conduction.

2.4. Anatomy of the Heart

The mammalian heart is an electrically driven mechanical pump which pumps blood to the lungs and into the body. It consists of 4 cavities: the right and left atrium and the right and left ventricle. Deoxygenated blood enters the right atrium through the superior caval vein (blood from brain and upper extremities) and the inferior caval vein (blood from lower body). Through the tricuspid valve the blood reaches the right ventricle and from there it is pumped into lungs, where it is re-oxygenated. The oxygen-rich blood then enters the left atrium through the pulmonary veins, passes the bicuspid valve, and enters the left ventricle. From there it is pumped into the aorta and distributed all over the body.

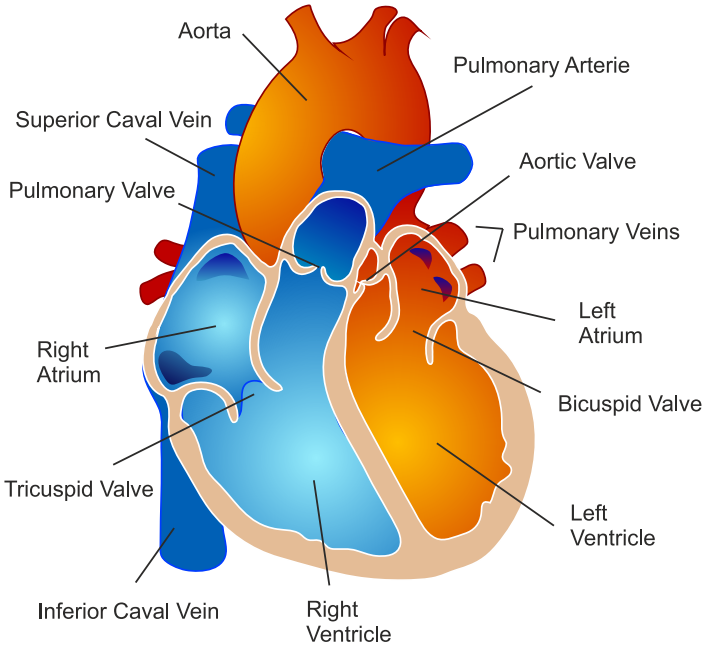

Figure 2.6.: Anatomy of the heart. Adapted from Ruiz (2006a).

2.5. Cardiac Conduction System

The mechanical action, i.e the contraction of the heart, is initiated by an electrical impulse which is generated in the sinoatrial node (SAN). The SAN is crescent-like shaped and consists of densely packed specialized myocytes (pacemaker cells). It cannot be seen as a sharply delimited accumulation of cells but it is a diffuse structure which spans a large area between the superior and inferior caval vein (Monfredi et al., 2010; Sánchez-Quintana, Cabrera, et al., 2005). Cells of the SAN have no stable RP, i.e repolarization is followed by a phase of early diastolic depolarization (EDD) which depolarizes the cell to its threshold potential and triggers a subsequent AP. Two mechanisms for EDD have been proposed, one related to intracellular Ca^{2+} cycling (Bogdanov et al., 2006; Maltsev and Lakatta, 2008) and the other one related to a special ionic current, the funny current I_f (Bucchi et al., 2007; DiFrancesco, 2010). Their importance to pacemaker activity has been intensively discussed (Lakatta and DiFrancesco, 2009). Steepness of EDD determines the firing rate of the SAN and thus the heart rate. In electrophysiological experiments heart rate is usually measured in terms of basic cycle length (BCL), i.e. the time between two consecutive activation events in ms. Electrical activation spreads from the SAN over the right atrium and reaches the atrioventricular node where a time delay is introduced. This time delay allows the ventricle to be filled completely. The bundle of His propagates the electrical

activation into the ventricles where the entire ventricular myocardium is activated. The individual parts of the cardiac conduction system are shown in Figure 2.7.

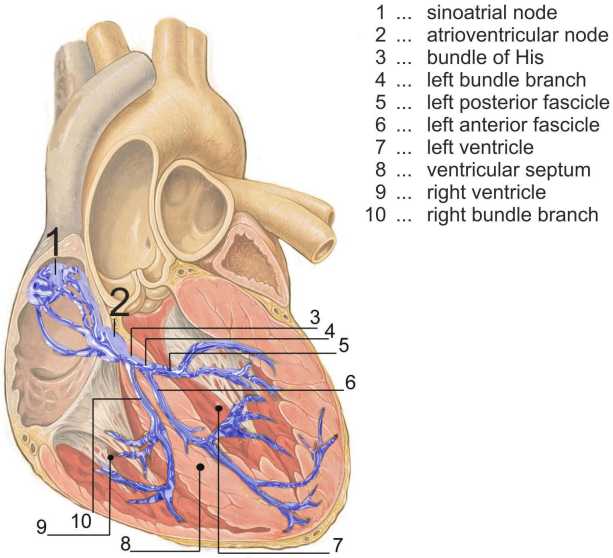

Figure 2.7.: Cardiac conduction system. From Lynch and Jaffe (2007).

2.6. Measuring Electrical Activation

2.6.1. Intracellular Measurements

For direct measurement of transmembrane potential V_m intracellular glass microelectrodes are used. Thin glass capillaries are heated and pulled until they break. Temperature and pulling force determine the length and thickness of the manufactured electrode. Typically tip diameters of less than 0.3 µm are used. This yields electrodes with an resistance of $15-25\,\mathrm{M\Omega}$ (Lavallée et al., 1969). The electrodes are filled with $2-3\,\mathrm{M}$ KCl and electrical connection between the filling solution and downstream signal conditioning hardware is established with an Ag/AgCl wire inserted into the microelectrode. Intracellular potentials are usually derived with respect to an extracellular reference electrode in the tissue bath. Figure 2.8 illustrates the measurement principle. This technique allows direct measurement of absolute values of action potentials like resting membrane potential, upstroke velocity, overshoot, action potential duration, a.s.o. However, one limiting factor is the stability of electrode impalement. In case of contracting tissue preparations, the mechanical movement forces the fine tip of the electrode out of the cell or ruptures the cell membrane.

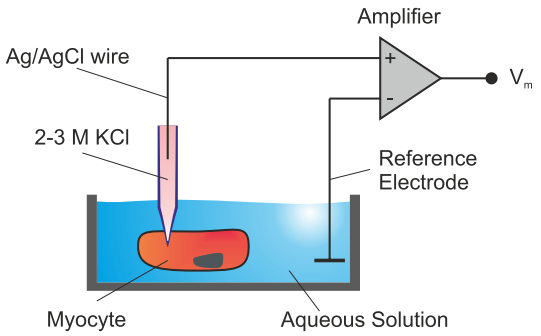

Figure 2.8.: Transmembrane potential V_m can be directly measured with a glass microelectrode penetrating the cell membrane.

2.6.2. Optical Measurements

Membrane voltages can be measured with voltage-sensitive dyes (Efimov et al., 2004). These dyes bind to the cell membrane and change their fluorescence upon changes in membrane voltage. The most widely used dyes in cardiac electrophysiology are di-4-ANEPPS[1] and di-8-ANEPPS. This method enables measurement of membrane voltage with very high spatial and temporal resolution but has some limitations like phototoxicity of the used dyes (Schaffer et al., 1994) and interference with parameters to be measured (e.g. slowing of conduction velocity as shown by Larsen et al. (2012)). Furthermore absolute values for action potentials can not be obtained unless optical signals are calibrated using a microelectrode-derived reference action potential.

2.6.3. Extracellular Measurements

As described in sections 2.2.4 and 2.3, cardiac cells are connected through gap junctions and ionic currents can pass from activated cells to downstream cells at rest via these low resistance pathways. The ionic current circuit is closed via the extracellular space. The extracellular space (called volume conductor) has a resistivity and therefore generates an extracellular voltage difference i.e. an electrical field (de Bakker and Wittkampf, 2010).
There are basically two methods to measure extracellular potentials: (i) unipolar and (ii) bipolar recordings. Unipolar recordings[2] are derived with respect to a reference

[1] ANEPPS ... AminoNaphthylEthenylPyridinium
[2] Clinicians speak of potential measurements without specifying a reference potential. In this work the reference potential is located in the tissue bath (see 3.2). Although physically not correct this nomenclature will be used throughout the thesis for consistency with the literature.

electrode considered to be "far" away. Bipolar recordings are derived between two measurement sites. The disadvantage of bipolar recordings is the directional dependence, i.e. a spreading electrical excitation perpendicular to the recording electrodes results in no signal.
As for optical measurements absolute values of the transmembrane potential cannot be obtained by extracellular measurements but intracellular parameters can be estimated from extracellular signals. The action potential duration (APD) can be estimated from extracellular recordings but this is challenging and has some limitations since repolarization currents are much smaller than depolarization currents (Vigmond et al., 2009).

Signal Waveforms

Electric potentials measured in the extracellular volume conductor have characteristic signal waveforms as shown in Figure 2.9. For a free-running activation wavefront, i.e. in the middle of a cable-like muscle strand, the waveform shows biphasic deflections with equal positive and negative fractions. At the beginning of the cable where activation is initiated the positive portion of the signal is reduced and at the end of the cable (sealed end) the negative portion is absent (Spach and Kootsey, 1985).

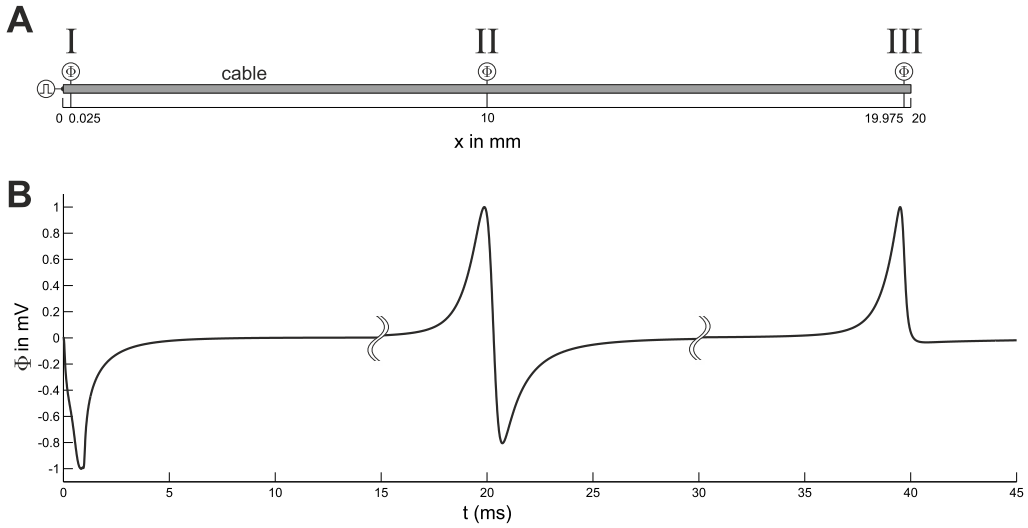

Figure 2.9.: (**A**) Computer simulation of a cable-like structure with stimulus site on the left. (**B**) Extracellular potentials Φ_e at recording sites I (starting), II (free-running), and III (ending/colliding). Adapted from Wiener (2012) with permission.

3. Measurement Setup

This chapter describes the overall measurement setup as well as animal species and the region of interest for this work. Theoretical principles of cardiac near field measurements are treated, including sensors and data acquisition hardware. Intracellular measurements and generation of pulse sequences for stimulation purposes is described. Documentation of measurement positions as well as documentation of macroscopic structure of specimen is outlined. Off-line data retrieval as an important part of the measurement system is described in the final section.

3.1. Tissue Preparations

3.1.1. Region Of Interest

The region of interest (ROI) in this work is the cavotricuspid isthmus (CTI) of the right atrium. This region is seen, among others, as potential arrhythmogenic substrate and target for catheter ablation therapy (Pérez et al., 2009). The CTI extends anteriorly from the tricuspid valve (TCV) to the Eustachian valve (EV) and ridge (ER) posteriorly and superiorly from the paraseptal isthmus (PSI) to the infero-lateral isthmus (ILI) anteriorly (Cabrera, Sánchez-Quintana, et al., 2005; Gami et al., 2010).

3.1.2. Atrial Dissection

Atrial preparations were obtained from guinea pigs and rabbits. Animals were heparinized (0.3 ml intravenously for rabbit and 1 ml intramuscularly for guinea pig) and anesthetized 5 minutes after administration.

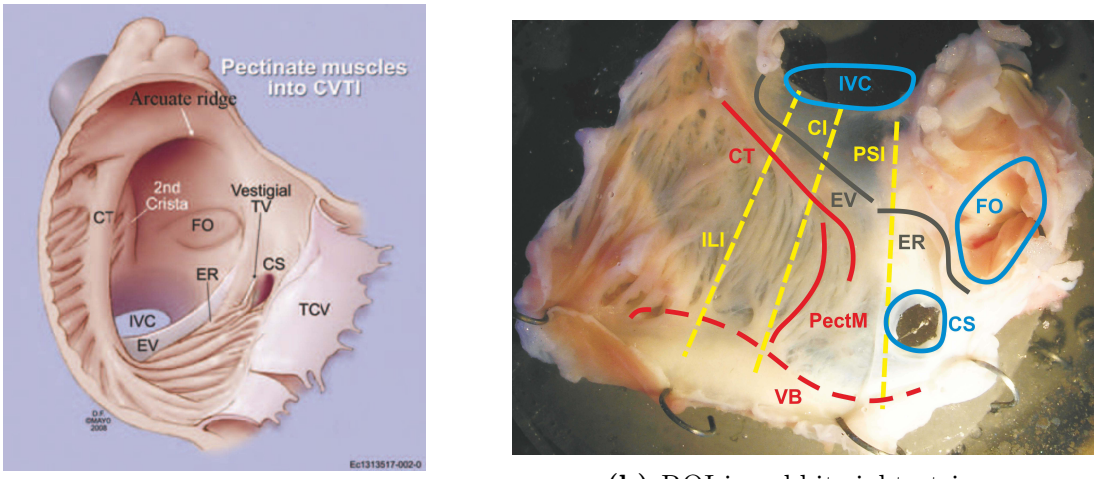

(a) ROI illustration in human heart.

(b) ROI in rabbit right atrium

Figure 3.1.: Region of interest. IVC, inferior vena cava; FO, fossa ovalis; CS, coronary sinus; EV, Eustachian valve; ER, Eustachian ridge; CT, crista terminalis; PectM, pectinate muscle; VB, vestibule; ILI, infero-lateral isthmus; CI, central isthmus; PSI, paraseptal isthmus; TCV, tricuspid valve. **(a)** from Gami et al. (2010), ©2010 Wiley Periodicals, Inc.

Anesthetic for rabbit was $5-10\,\mathrm{mg\,kg^{-1}}$ Propofol and $20\,\mu\mathrm{g\,kg^{-1}}$ Fentanyl intravenously. For guinea pig anasthetic was $0.4\,\mathrm{ml\,kg^{-1}}$ Ketasol and $0.4\,\mathrm{ml\,kg^{-1}}$ Domidor intramuscularly. Hearts were quickly removed and placed in cold ($4-8\,^{\circ}\mathrm{C}$) and oxygenated Tyrode solution to stop contraction and to lower oxygen consumption. Atrial preparations were dissected by cutting open the right ventricle from apex to the TCV and on to the superior vena cava (SVC). After opening the atrium it was completely detached from the rest of the heart by cutting along the interatrial and atrio-ventricular septum. The right atrial appendage (RAA) was opened and the preparation was pinned down with tungsten needles on a transparent silicone carrier.

3.1.3. Papillary Muscle Dissection

Papillary muscles (PM) were dissected preferentially from the right ventricle. PMs with diameters larger than approximately 1 mm were not dissected and used because of possible insufficient supply by superfusion. After dissection PMs were pinned down with tungsten needles on silicone carriers. Length of PMs on the carrier was maintained as originally seen in the ventricle.

3.2. Tissue Bath

After the atrial tissue preparation was pinned down on a transparent silicone carrier (cf. Section 3.1.2), it was transferred from the preparation bath to the experiment bath. This tissue bath was custom-designed and is shown in Figure 3.2.

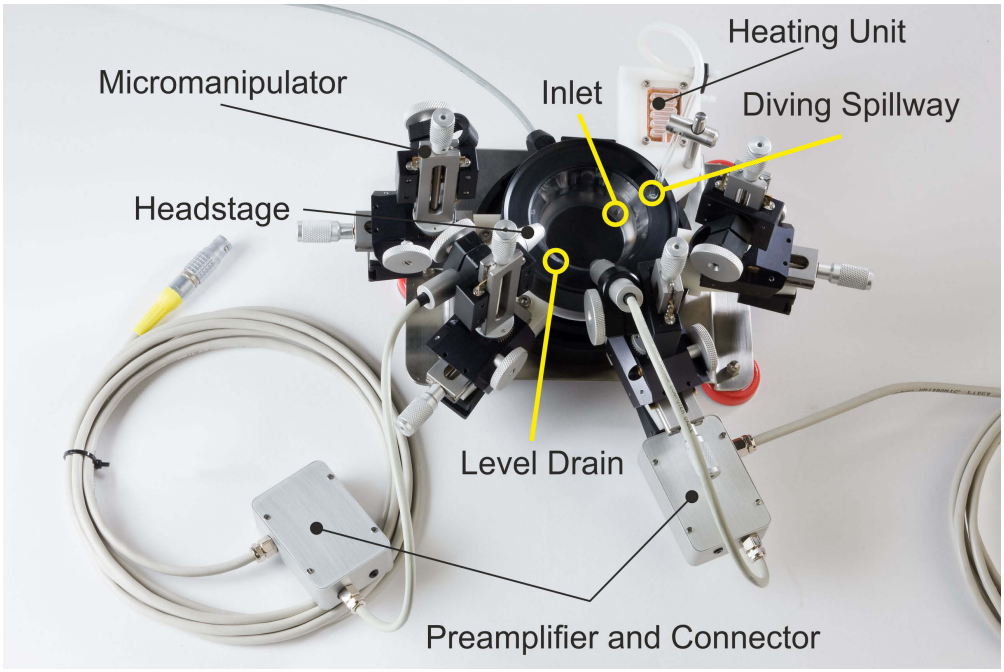

Figure 3.2.: Tissue Bath. Nutrition solution was heated to 36.4 °C and entered the tissue bath via an inlet the bottom. Liquid level was adjusted with a diving spillway. Preamplifiers were mounted on 3D-micromanipulators and positioned around the tissue bath.

To minimize interferences while performing electrical measurements the tissue bath was placed in a Faraday cage. The superfusate (Tyrode solution, see Appendix A.1) was pumped with a peristaltic pump (outside the Faraday cage) through a heating unit into the tissue bath. Temperature of the solution was regulated by a 2-point PID-controller and was maintained at 36.4 °C. Liquid level was adjusted with a diving spillway. Potential sensors (see Section 3.3.2) and headstages were mounted on 3D-micromanipulators attached around the tissue bath. The inner surface of the bath was transparent with incorporated LED-lights for illumination of the tissue preparation. At the bottom of the tissue bath a circular Ag/AgCl reference electrode for electrical measurements was installed.

3.3. Cardiac Near Field Measurements

3.3.1. Definition of the Cardiac Near Field

A propagating electrical excitation wave produces a potential gradient in the extracellular volume conductor (cf. Section 2.6.3). The potential gradient of the extracellular potential $\Phi_e(t)$ therefore describes a time-dependent electrical field, the cardiac near field, CNF. With an arrangement of two closely spaced extracellular potential electrodes the spatial discrete approximation $\tilde{\mathbf{E}}(t)$ of the CNF strength $\mathbf{E}(t)$ parallel to and in the vicinity of the tissue surface can be estimated:

$$\mathbf{E}(\mathbf{x}_F, t) = -\nabla\Phi_e(\mathbf{x}_F, t) \tag{3.1a}$$

$$\tilde{\mathbf{E}}(t) = -\frac{1}{D}\Big[\Phi_{e2}(t) - \Phi_{e1}(t)\Big] \tag{3.1b}$$

where $\mathbf{x}_F$ is the point of observation and D is the distance between the two recording electrodes. Accuracy of $\tilde{\mathbf{E}}(t)$ is determined by the interelectrode spacing and the temporal sampling rate f_S. Given an interelectrode spacing of 70 µm sampling rates of 100 kHz are required (Plank and Hofer, 2000).

3.3.2. CNF Sensors

To characterize microconduction low-weight miniature sensor arrays were designed (Hofer, Keplinger, et al., 2006). These needle-like sensors are made of polyimide film and comprise 4 Ag/AgCl electrodes at the tip. Unipolar electrograms Φ_e are recorded with respect to a reference electrode (cf. Section 3.2). Spacer pillars keep the electrodes at a specific distance to the tissue surface (70 µm) and thus allow non-contact recordings of extracellular potentials Φ_e. Spacing also allows the perfusate to flow beneath the sensor and therefore protect the underlying tissue from suffering local ischemia. Sensor dimensions and electrode configuration are shown in Figure 3.3a.

The four electrodes at the tip of the sensors are quadratically arranged with a diagonal distance (DD) of 70 µm and therefore enable the estimation of the CNF strength $\tilde{\mathbf{E}}$ at the central point of the electrodes by calculating the CNF components $\tilde{\mathbf{E}}_{\mathbf{x}^*}$ and $\tilde{\mathbf{E}}_{\mathbf{y}^*}$ along two electrode axes. These axes are depicted in Figure 3.3b. To align the electrode coordinate system x*y* with the sensor coordinate system xy (i.e. the reference

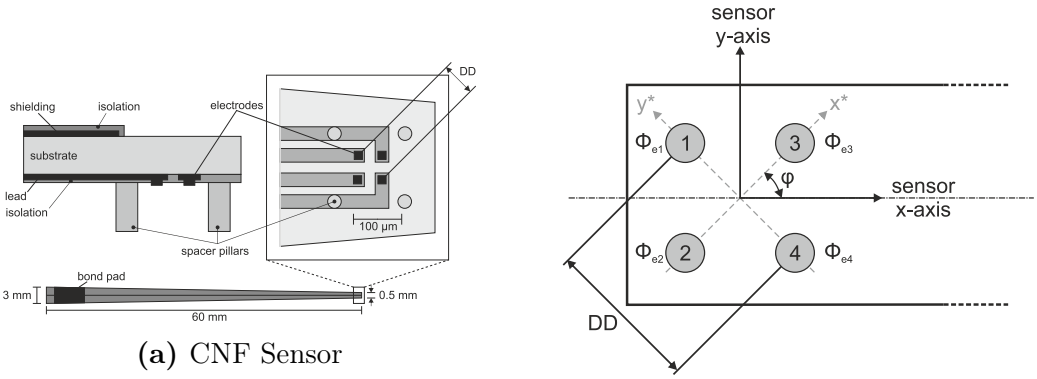

(a) CNF Sensor

(b) Sensor Axes Orientation

Figure 3.3.: Cardiac near field sensor. (a) At the tip 4 Ag/AgCl electrodes are placed in a quadratically arrangement. (b) The sensor axes and the electrode axes are not aligned and therefore have to be corrected.

coordinate system) the components of $\tilde{\mathbf{E}}$ have to be rotated by 45° in mathematically positive sense. The CNF strength $\tilde{\mathbf{E}}$ can hence be obtained by:

$$\tilde{\mathbf{E}}(t) = \begin{bmatrix} \tilde{\mathbf{E}}_{\mathbf{x}} \\ \tilde{\mathbf{E}}_{\mathbf{y}} \end{bmatrix} = \frac{1}{DD}\mathbf{A}(\varphi) \begin{bmatrix} \Phi_{e3}(t) - \Phi_{e2}(t) \\ \Phi_{e1}(t) - \Phi_{e4}(t) \end{bmatrix} \tag{3.2a}$$

$$\mathbf{A}(\varphi) = \begin{bmatrix} \cos\varphi & -\sin\varphi \\ \sin\varphi & \cos\varphi \end{bmatrix} \tag{3.2b}$$

where $\mathbf{A}(\varphi)$ is the rotation matrix and $\Phi_{e1\ldots e4}$ are unipolar extracellular electrograms.

3.3.3. Parameters obtained from CNF

Local Activation Time

Local activation time (LAT) refers to the instant in time at which a cardiomyocyte is in its upstroke phase, i.e. the cell is activated. It has been shown by Spach and Kootsey (1985) that LAT closely coincides with the maximum negative deflection in the extracellular potential Φ_e. Equivalently LAT can be determined from the negative peak in $\dot{\Phi}_e$ which was used in this work. Assuming a sampling rate of 100 kHz (standard value) accuracy of peak detection lies within ±5 µs.

A spreading electrical activation wavefront reaches the individual electrodes of a CNF sensor at different instances of time and therefore 4 distinct activation times $LAT_{1\ldots4}$ can be determined for each electrode.

Local Conduction Velocity

From the latencies between $LAT_{1\ldots4}$ the magnitude of local conduction velocity LCV, as well as the direction α_{LCV} of the electrical wavefront with respect to the sensor axis can be estimated with a finite differences approach (Plank and Hofer, 2000):

$$\nabla LAT\,(x,y) = \begin{bmatrix} gt_x \\ gt_y \end{bmatrix} = \frac{1}{DD}\begin{bmatrix} LAT_3 - LAT_2 \\ LAT_1 - LAT_4 \end{bmatrix} \tag{3.3a}$$

$$\mathbf{LCV} = \begin{bmatrix} v_x \\ v_y \end{bmatrix} = \frac{1}{{gt_x}^2 + {gt_y}^2}\begin{bmatrix} gt_x \\ gt_y \end{bmatrix} \tag{3.3b}$$

$$LCV = \sqrt{{v_x}^2 + {v_y}^2} \tag{3.3c}$$

$$\alpha_{LCV} = \arctan\frac{v_x}{v_y} + \varphi \tag{3.3d}$$

The direction α_{LCV} is corrected by φ to compute the angle of propagation relatively to the sensor axes and not to the electrode axes (cf. Figure 3.3b). Estimation of α_{LCV} fails if direction of propagation is not parallel to the sensor axis. In the worst case, i.e if the direction of propagation is perpendicular to the sensor axis, estimation yields infinite LCV and therefore α_{LCV} is inaccurate.
Accuracy in determination of LCV can be improved by interpolation. For estimation of LCV in this work a window of 1 ms around LAT in $\dot{\Phi}_e$ was selected and interpolated with a factor $I = 100$. Latencies between electrode pairs were calculated by cross-correlation function as described by Wiener (2012).

Fractionation Index

Fractionation is referred to the presence of multiple deflections in Φ_e and $\dot{\Phi}_e$ and indicates multiple independent activation wavefronts delayed to each other. Electrograms with one prominent deflection are denoted non-fractionated or uniform and fractionated otherwise. In clinical applications areas characterized by complex fractionated atrial electrograms (CFAEs) are targets for catheter ablation interventions to terminate atrial fibrillation (Calkins et al., 2012). Time scale of fractionation largely differs between its definition in clinical applications (up to 100 ms) and in CNF signals (1 – 10 ms).
It has been shown by de Bakker and Wittkampf (2010) and Jacquemet and Henriquez (2009) that fractionation arises due to the complex microstructure of cardiac tissue amongst other factors. Fractionation measured by CNF recordings can be considered local events related to microstructure due to the small interelectrode distance used

for recording. The fractionation index (FI) is an integer value reflecting the number of underlying independent activation events superimposed in Φ_e. In this work FI was determined by a cross-correlation based method which uses a signal model of Φ_e as introduced by Wiener (2012).

Vector Loop of CNF

Plotting the components of $\tilde{\mathbf{E}}$ in an XY-diagram yields a vector loop (VL) comparable to classical vectorcardiography. Morphology of the obtained VL reflects local excitation properties, i.e. wavefront curvature ("open" or "narrow"), fractionation (multiple loops), and direction of excitation spread (Plank, Vigmond, et al., 2003). For uniform electrograms of a planar wavefront the loop degenerates to a single line and the vector of maximum amplitude $\tilde{\mathbf{E}}_{\mathbf{max}}$ points in opposite direction of the spreading wavefront. Direction of excitation spread can be determined from VL either by estimating $\alpha_{E,max}$ at $\tilde{\mathbf{E}}_{\mathbf{max}}$ or by estimating $\alpha_{E,LAT}$ at $\tilde{\mathbf{E}}(LAT)$. Estimation of $\alpha_{E,max}$ fails in case of large wavefront curvature (open vector loop) since the maximal CNF strength lies at the side lobes. The most robust estimation of excitation direction turned out to be calculation of $\alpha_{E,LAT}$ and therefore was used throughout this thesis.

Waveform Symmetry

The symmetry of an extracellular potential Φ_e, i.e. the ratio of positive portion to negative portion, is characteristic at recording sites along a cable-like structure as shown in Section 2.6.3. To describe the different shapes a symmetry factor a as proposed by Jacquemet and Henriquez (2009) was used:

$$a = \frac{\Phi_{max} - |\Phi_{min}|}{\Phi_{max} - \Phi_{min}} \tag{3.4}$$

Depolarization Duration

The depolarization time t_{depol} characterizes the spatial extent of the spreading electrical excitation wavefront. It is defined as:

$$t_{depol} = t\big|_{\Phi_{min}} - t\big|_{\Phi_{max}} \tag{3.5}$$

Equivalently t_{depol} can be estimated from $\dot{\Phi}_e$ by determining the time elapsed between the zero crossing before LAT and after LAT. Determination of t_{depol} fails for signals at the beginning and the end of a cable where signal waveforms lack either the positive or negative deflection (cf. Section 2.6.3).

3.3.4. Measurement Chain

CNF sensors record unipolar extracellular signals Φ_e with respect to a Ag/AgCL reference electrode at the bottom of the tissue bath (cf. Section 3.2). The sensors were connected to unity gain impedance converter (headstage) and a preamplifier. The preamplifier introduced a gain of factor 10. After preamplification signals were transmitted via shielded cables to a main amplifier. An additional gain of factor 10 was introduced resulting in an overall amplification of $A = 100$. After amplification signals were filtered with a 4^{th}-order Bessel anti-aliasing filter with cutoff frequency $f_{cut} = 20\,\text{kHz}$. Thus sampling rates of 50 kHz are required to satisfy Shannon's sampling theorem (Oppenheim et al., 1999). The pre-processed signals were digitized with a sampling rate of $f_s = 100\,\text{kHz}$ using industry-standard DAQ hardware[1] based on PXI-standard[2] (National Instruments, Austin, Texas, USA). The PXI system was connected to a standard desktop PC running a custom-written LabVIEW™ software application. The overall measurement system has been described in more detail earlier (Arnold, 2009b).

3.4. Intracellular Measurements

Within the right atrium and the ROI functional heterogeneities of the cell membrane exist (Feng et al., 1998; Sidorov et al., 2011). These heterogeneities can be measured from intracellular APs and are related to maximum upstroke velocity $\dot{V}_{m,max}$ during depolarization, APD, RP, and OS (cf. Section 2.2.3).

3.4.1. Fabrication of Glass Microelectrodes

Standard pulled glass microelectrodes (GME) were fabricated using a DMZ Universal Puller (Zeitz-Instruments, Munich, Germany) and borosilicate capillaries with fil-

[1] DAQ ... data acquisition
[2] PXI ... PCI extension for instrumentation

ament of 1.5 mm outer diameter, and 0.86 mm inner diameter (GC150F-15, Harvard Apparatus, Holliston, Massachusetts, USA). After pulling (for detailed protocol see Appendix A.2) the microelectrodes were filled with 2.5 M KCl. The resistance of the fabricated microelectrodes was 10 – 20 MΩ.

3.4.2. Parameters obtained from Intracellular Measurements

Recording transmembrane potential V_m with GME enables determination of absolute values of action potentials i.e. resting membrane potential V_{rest} and overshoot potential V_{OS}, directly. Maximum upstroke velocity of the action potential can be determined from $\dot{V}_m$. There are several definitions for estimation of action potential duration APD: APD_{90} and APD_{50} are determined from time instance of maximum upstroke in V_m (activation) to 90 % repolarization or 50 % repolarization, respectively.

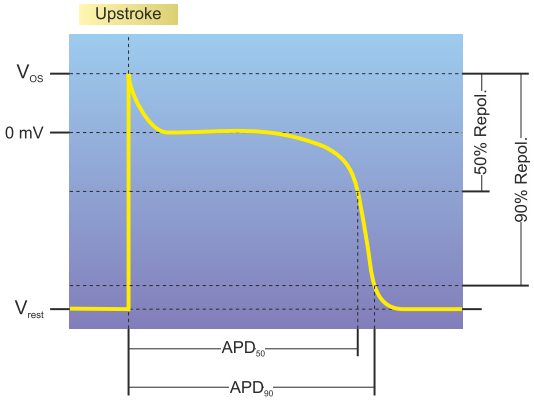

Figure 3.4.: Different definitions of APD.

3.4.3. Measurement Chain

Electrolyte filled GMEs were inserted into electrode holders which contained a Ag/AgCl half cell (Harvard Apparatus, Holliston, Massachusetts, USA) and were filled with the same 2.5 M KCl solution as the GME to provide electrical contact. The electrode holder was connected to an active probe which was mounted on a 3D-micromanipulator. Intracellular signals Φ_i were recorded with respect to a reference electrode in the tissue bath (cf. Section 3.2) using an electrometer preamplifier (Electro 705, Harvard Apparatus, Holliston, Massachusetts, USA). Signals were digitized using the same PXI-based DAQ hardware as described above in Section 3.3.4.

3.5. Electrical Pacing

To modulate heart rate and mimic tachyarrhythmias electrical pacing of tissue preparations was used. Therefore, a pacing unit was developed based on a FPGA[3] module and a custom-written LabVIEW™ application. Hardware and software architecture were described in an earlier work (Arnold, 2009b).

3.5.1. Pacing Protocols

Timing characteristics of pacing protocols were specified in terms of pacing cycle length (PCL), i.e. the time interval between two consecutive pacing pulses. Timing was either static or dynamic: static pacing generated a stimulus pulse train with constant PCL whereas for dynamic pacing protocols PCL was modulated with three different timing characteristics. In ramp-like protocols PCL was reduced after each stimulus by Δt. Similarly in a stair-like protocol PCL was reduced by Δt after a defined number of pulses at constant PCL was generated. In premature beat or S1S2 protocols a basic rhythm is specified and after a number of stimuli at this basic frequency (S1 pulses) one early stimulus is generated (S2 pulse). The interval of S2 pulses is decreased for consecutive S2 pulses by Δt. Timing characteristics of the different pacing protocol types are shown in Figure 3.5 and listed in Table 3.1.

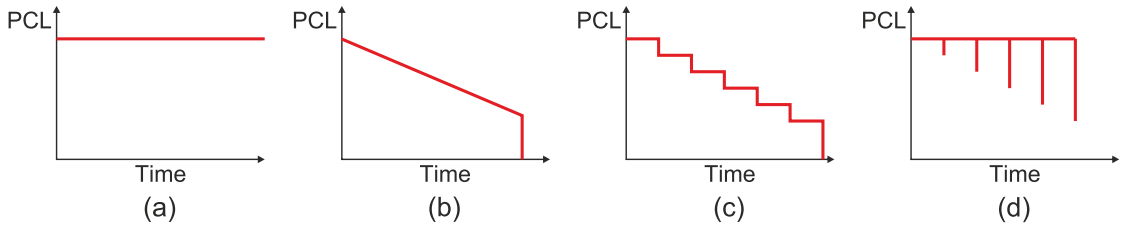

Figure 3.5.: Implemented types of pacing protocols. (a) Static pacing with fixed PCL, (b) ramp-like dynamic pacing, (c) stair-like dynamic pacing, (d) premature beat (S1S2) pacing.

In atrial tissue preparations overdrive pacing was used, i.e. PCL_{start} was set to values higher than sinus rhythm to achieve stable capture of stimulus response. If no conduction block occurred until PCL_{end}, the protocol was repeated with PCL_{end} set to 20 ms.

[3] Field-Programmable-Gate-Array, a configurable integrated circuit

Table 3.1.: Standard timing characteristics for pacing protocols. If no conduction block occurred PCL_{end} was reduced to 20 ms.

Parameter	Ramp	Stair	S1S2
PCL_{start} (ms)	350	350	350
Δt (ms)	5	5	5
stimuli at PCL	1	15	9
PCL_{end} (ms)	50	50	50

For all dynamic protocols pre-pacing was enabled, i.e. a configurable number of stimuli (typically 100) with constant PCL was generated before a protocol was started to achieve steady state conditions. PCL was set to the start PCL of the protocol. Also post-pacing was configurable where the program automatically switched to static pacing after the protocol had finished. This was important for papillary muscle preparations since they should be paced continuously to prevent irreversible contracture of the muscle.

Stimulus pulses were applied to the tissue using a constant current source (WPI A360, World Precisions Instruments Inc., Sarasota, FL) and a single lead tungsten wire. Pacing stimuli were applied at twice the threshold current.

3.5.2. Parameters obtained from Pacing Protocols

For each pacing protocol the index of the pacing impulse S_b which first failed to trigger a stimulus response was determined. If no conduction block occurred until the end of the pacing protocol the recording was excluded from analysis. CNF parameters of n beats prior to S_b were selected for beat-to-beat analysis. n depended on the dynamic of the pacing protocol and was 15 for ramp-like dynamics, 30 for stair-like dynamic, and 15 for S1S2 protocols in which only S2 pulses were analyzed. Hence, from k recordings of the same pacing dynamics n pre-block groups each comprising k elements were obtained.

Each pre-block group S_{b-m} with $m = 1 \ldots n$ was analyzed for normal distribution of parameters using a Kolmogorov-Smirnov test with $\alpha \leq 0.05$. Differences between pre-block groups were tested using a Mann-Whitney U-test with a significance level of $\alpha \leq 0.05$. Results from Mann-Whitney U-test were plotted as color-coded matrix (SM, significance matrix) where red indicates

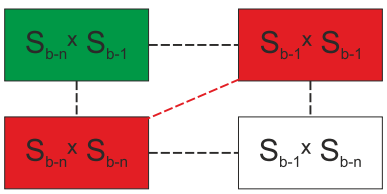

Figure 3.6.: Significance Matrix.

no statistically significant differences and green indicates statistically significant differences. Matrix element $a_{i,j}$ is the result of comparison of pre-block group S_{b-i} with pre-block group S_{b-j} with $i, j = 1 \ldots n$ resulting in a $n \times n$ matrix. The scheme is illustrated in Figure 3.6.

3.6. Documentation of Structure and Recording Positions

Documentation of recording positions was essential for this work since the characterization of excitation spread was done time-serial. Thus, documentation means for high-resolution images have been integrated into the measurement system. Images of the tissue preparation in the tissue bath were taken with a digital SLR camera (Canon EOS 5D Mark II, Canon, Japan) mounted on a XY-support on the ceiling of the Faraday cage. The camera was positioned and its position was fixed prior to the experiment so that the field of view (FOV) covered the tissue bath. The used lens (Canon EF 180mm f/3.5L USM, Canon, Japan) enabled a resolution of 10.6 µm/Pixel and therefore accurate determination of individual recording positions.

3.6.1. Transillumination

To improve allocation of recording positions and resolution of small fiber strands a transillumination device was developed. This plug-shaped device was placed in the tissue bath with the tissue preparation on top (Hofer, Wiener, et al., 2011). The LED module (GW5BWC15L02 normal white, Sharp, Japan) was mounted on a heat sink inside a metal case. The case was filled with transparent silicone. Temperature sensors were integrated to ensure that the tissue preparation, which was placed on top of the device, is not exposed to too high temperatures. Electrical circuits were protected by cable break detectors in case the housing was leaky.

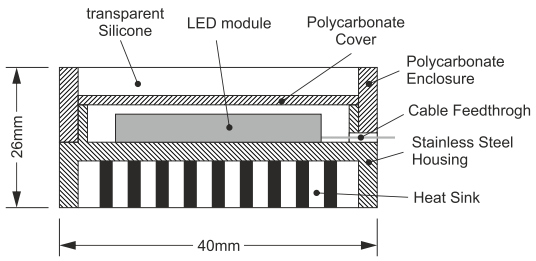

Figure 3.7.: Transillumination device.

3.6.2. Macrophotography

Post experimentum high-resolution images of the tissue preparation were taken. The camera (Canon EOS 5D Mark II, Canon, Japan) was mounted on a vertically adjustable stand. The tissue preparation (immersed into cold Tyrode solution) was placed on a holder on a stepping motor driven XY-table.

Figure 3.8.: Macrophotography unit.

Illumination was either done with a macro-flash unit (Macro Twin Lite MT-24EX, Canon, Japan) or with a transillumination unit (based on LED, GW5BWC15L02 normal white, Sharp, Japan) integrated in the system. The lens (Canon MP-E 65mm, Canon, Japan) enabled a resolution of 1.2 µm/Pixel. The macrophotography unit was controlled by a custom-written LabVIEW™ application and automatically scanned the tissue preparation. After scanning the individual images were stitched using freely available software (e.g. Autostitch).

3.6.3. Parameters obtained from Digital Images

To characterize atrial tissue morphology, classification of the ROI in digital images was performed. Images were expert reviewed and borders of the CTI, i.e ILI, PSI, CT, and VB, were identified. Within the CTI individual pectinate muscles (PectM) were identified. Each PectM was further divided into 3 segments: proximal (PectMp), central (PectMc), and distal (PectMd) with respect to the CT. The proximal segment was defined as continuous structure emerging from the CT until first branching into multiple central segments. Accordingly the distal segment was defined as continuous structure from lowest merging area of multiple central segments down to the VB. In case the proximal segment did not show a branching site (single muscle strand emerging from the CT and ending in distal segment) no proximal segment was defined.

Distal segments ("stems" of PectM) were labeled with uppercase letters starting at the ILI towards the PSI. Parallel central segments leading to the same PectMd were numbered (c1, c2, etc.) starting with the segment closest to the ILI continuing towards

the PSI. Thus for each PectM strand a unique label was assigned, e.g. Ap1c3d1 for a PectM along segment p1-c3-d1 ending in stem A.
For each structure within the CTI area, diameter, and length were determined using CorelDraw© (Corel Corporation, Ottawa, Ontario, Canada) with freely available macros (e.g. getArea12c). Diameter of the VB was calculated as mean value of three measurements at the ILI, CI, and PSI. Diameter of the CT was determined in the central part of the CT. Lengths of structures were calculated along the central line of the structures.

From recording sites located in the proximal sections of PectMs, the initiation sequence of neighboring PectMs was determined. Therefore LAT_p of the recording site closest to the CT was determined for all proximal segments. Accordingly the arrival sequence in the VB was determined from LAT_d at recording sites in the distal segment closest to the VB. To quantify the initiation sequence the "Displacement Variance" VAR_d was introduced and calculated according to following formula:

$$VAR_d = \frac{1}{N} \sum_{i=1}^{N} \left(I_{i,M} - I_{i,E}\right)^2 \tag{3.6}$$

with VAR_d the displacement variance, N the number of proximal segments in the CTI, $I_{i,M}$ the measured initiation index of proximal segment i, and $I_{i,E}$ the expected initiation index of proximal segment i. The expected initiation sequence is sorted starting from the PSI to the ILI (cf. Figure 5.15). A value of $VAR_d = 0$ refers to a perfectly sorted initiation sequence. VAR_d has a maximum if the initiation sequence is reversed. It can be shown that for a sequence of length N the maximal displacement variance can be calculated by:

$$VAR_{d,max} = \frac{1}{3}N^2 - \frac{1}{3} \tag{3.7}$$

3.7. Statistical Analysis

Parameters were tested for normal distribution using a Kolmogorov-Smirnov test with a significance level of $\alpha \leq 0.05$. Parameters were compared using a Mann-Whitney U-test and were considered statistically significant with $\alpha \leq 0.05$.
Parameters expressed as $mean \pm std$ in single experiments were pooled to overall results

using:

$$\overline{x} = \frac{\sum_{i=1}^{N} n_i \overline{x}_i}{\sum_{i=1}^{N} n_i} \qquad s^2 = \frac{\sum_{i=1}^{N} n_i {s_i}^2 + \sum_{i=1}^{N} n_i \left(\overline{x}_i - \overline{x}\right)^2}{\sum_{i=1}^{N} n_i} \tag{3.8}$$

where $\overline{x}$ is the pooled mean of all experiments, s is the pooled standard deviation of all experiments, $\overline{x}_i$ is the mean value for experiment i, s_i is the standard deviation for experiment i, n_i is the sample number for experiment i, and N is the number of experiments.

Results are shown as boxplots when appropriate. MATLAB™ was used to create boxplots with the central mark as median, the edges of the box as the 25^{th} percentile q_1 and 75^{th} percentile q_3, the whiskers extending to the most extreme data points not considered outliers, and outliers plotted individually. Outliers were defined as values larger than $q_3 + 1.5(q_3 - q_1)$ or smaller than $q_1 - 1.5(q_3 - q_1)$. This corresponds roughly with $\pm 2.7\sigma$ or $\pm 99.3\,\%$ coverage if the data are normally distributed (MathWorks, 2013).

3.8. Data Retrieval

During the experiments a vast amount of data (signal data plus image data) was recorded. On the one hand data from a large number of recording positions (∼100) had to be saved and on the other hand individual files were very large (several 100 MB for long streams of data). To ease data retrieval for off-line analysis a software application was developed utilizing LabVIEW™, DIAdem™, and MATLAB™ (Arnold, 2009a; Arnold, Wiener, and Hofer, 2010).

3.8.1. Framework

A GUI[4] was developed in LabVIEW™. After selecting an experiment repository, images of all recording positions (cf. Section 3.6) were displayed. Upon selection of one recording position, all data files corresponding to the selected recording position were listed. Data files were opened and viewed in DIAdem™. In DIAdem™ an interface for executing MATLAB™-code was implemented for data analysis and data manipulation (digital filters, parameter estimation, export functions, a.s.o.).

[4] Graphical User Interface

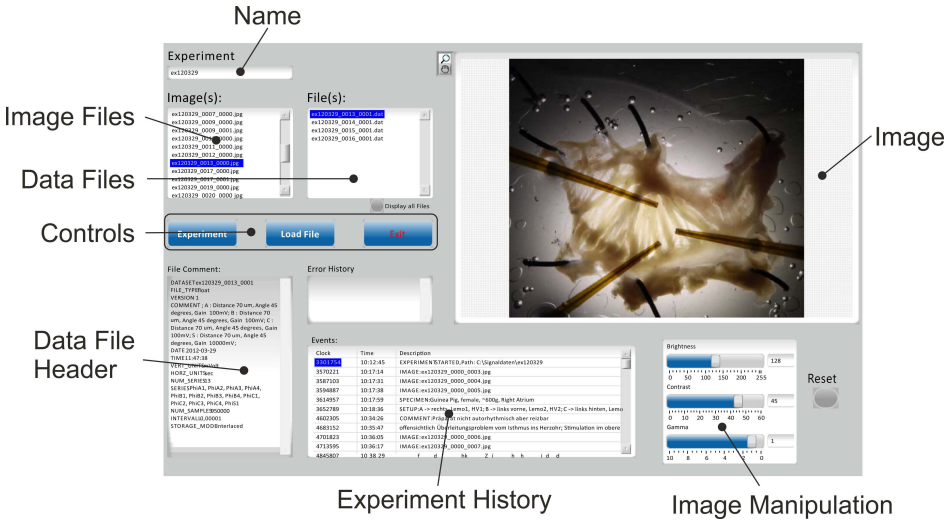

Figure 3.9.: GUI of the data retrieval application developed in LabVIEW™.

3.8.2. Event-Structure

For documentation of experiment history an event-driven approach was used. For each experiment a text file was created containing time and type of actions performed during the experiment. Types of events were e.g. recording data, taking images, running pacing protocols, or custom events (free text). The event structure therefore enabled reconstruction of any experiment performed by creating a thorough timeline.

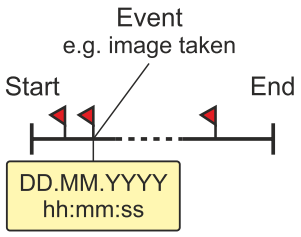

Figure 3.10.: Event-Structure.

Part II.

Experiments and Results

4. Morphometry

Morphometry was performed for 13 rabbit atria. Figure 4.1 illustrates the classification of the ROI as described in Section 3.6.3.

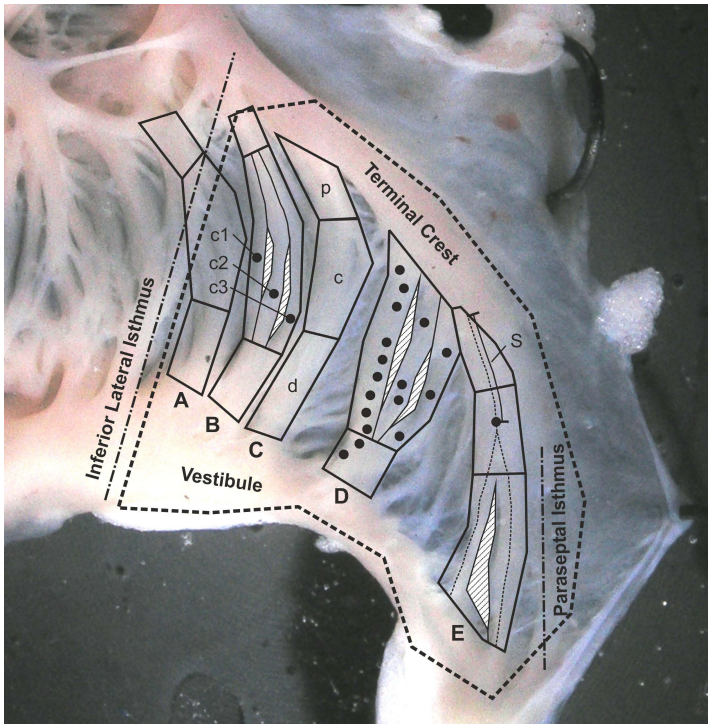

Figure 4.1.: Classification of ROI. Stems of PectM were labeled with uppercase letters. Individual PectMs were divided into segments: proximal (p), central (c), and distal (d). Parallel muscles were indexed. Full circles, recording positions; S, central line of PectM. From Arnold, Wiener, Sanchez-Quintana, et al., 2011 ©2011 IEEE

Weight of the rabbits was 4.11 ± 1.20 kg with a range of $2.75 - 6.20$ kg.

The ILI delimiting the CTI was 14.8 ± 2.2 mm long and CTI narrowed to 7.3 ± 1.8 mm at the PSI. Diameter of the CT at the central part was 1.70 ± 0.41 mm. The VB

measured 2.43 ± 0.98 mm in diameter (mean of all measurements along VB). The VB was thicker at the ILI (3.07 ± 0.90 mm) and progressively decreased to 2.21 ± 0.69 mm at the CI and 2.01 ± 0.70 mm at the PSI.

Total area of the CTI was $114.2 \pm 35.7\,\mathrm{mm}^2$. The area covered by the PectM network was $40.8 \pm 15.1\,\mathrm{mm}^2$ and CT plus VB covered $41.2 \pm 13.0\,\mathrm{mm}^2$. By subtracting the areas of CT, VB, and PectM from CTI, the area of non pectinate tissue (NPT) was calculated. NPT comprises thin muscle fibers and connective tissue of the epicardium and was $32.2 \pm 14.0\,\mathrm{mm}^2$. Thus PectM covered $35 \pm 7\,\%$ of the total CTI area and NPT covered $28 \pm 6\,\%$ of the total CTI area.

To characterize excitation pathways within the CTI, PectMs were further subclassified into segments as described in Section 3.6.3. In the examined preparations the number of segments varied markedly: 4 (1 – 9) proximal segments, 7 (4 – 12) central segments, and 4 (2 – 6) distal segments were found. Numbers of segments are given as *median (range)*.
Lengths of the segments were 2.09 ± 1.12 mm, 5.02 ± 1.80 mm, and 2.12 ± 0.79 mm for PectMp, PectMc, and PectMd respectively. Total length of pectinate muscles along the central line was 8.81 ± 2.27 mm.
Diameters of PectM were 0.85 ± 0.46 mm in the proximal segment, 0.68 ± 0.32 mm in the central segment, and 1.15 ± 0.48 mm in the distal segment.
Calculated areas of the segments were $1.58 \pm 1.04\,\mathrm{mm}^2$ for PectMp, $3.30 \pm 2.06\,\mathrm{mm}^2$ for PectMc, and $2.29 \pm 0.86\,\mathrm{mm}^2$ for PectMd.

Detailed results are shown in Appendix A.3.

5. Autorhythm

In this chapter an overview of all experiments carried out is given and results obtained during autorhythmic activation of atrial tissue preparations are presented. The autonomous activation patterns and findings are the basis for hypotheses investigated by pacing techniques in Chapter 6.

5.1. Experiment Duration

Depending on the species (rabbit or guinea pig) and tissue under examination (right atrium or papillary muscle) the experiments lasted for 21 – 312 min. Experiment duration was determined from time of inserting the tissue into the tissue bath until removing the tissue from the tissue bath. Removing of the tissue was done for following reasons: completion of the scheduled experiment protocol, developing arrhythmias, loss of autorhythmicity, or inability to pace. An overview of number of animals and duration of experiments is shown in Table 5.1 and in Figure 5.1.

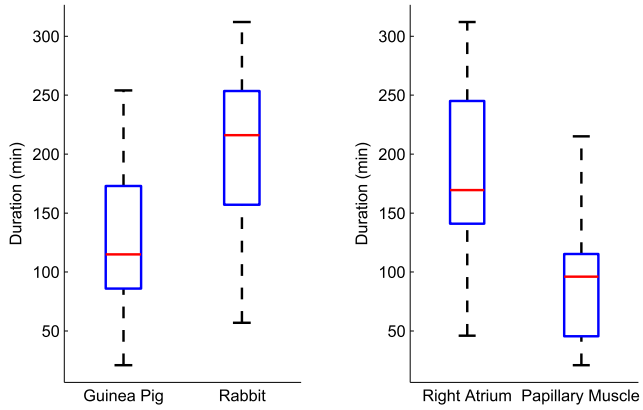

Figure 5.1.: Duration of Experiments.

Table 5.1.: Experiments.

Type	Number
Animals	53
Guinea Pig	25
Rabbit	28
Right Atrium	46
Papillary Muscle	11

5.2. Accommodation of BCL in Atrial Preparations

After preparing right atrial tissue preparations in cold Tyrode solution (cf. Section 3.1) the tissue was placed in the tissue bath with oxygenated and warmed Tyrode solution at 36.4 °C where they immediately started contracting. Accommodation until a stable BCL was reached lasted for approximately 30 – 60 min and was accompanied by episodes of tachyarrhythmias in 7 experiments (5 × rabbit, 2 × guinea pig). For analysis of arrhythmia episodes see Section 5.3. In 10 preparations arrhythmias were persistent (4 × rabbit, 6 × guinea pig). These preparations were electrically paced if possible or excluded from analysis otherwise. Atrial tissue preparations were further excluded from analysis if they did not develop autorhythm or if the preparation was damaged during dissection (5 preparations: 2 × rabbit, 3 × guinea pig). An overview of atrial tissue preparations is listed in Table 5.2.

Table 5.2.: Overview of atrial tissue preparations. PA, persistent arrhythmia; AE, arrhythmia epsiode.

	Total	Rabbit	Guinea Pig
Atria	51	28	23
Excluded	5	2	3
PA	10	4	6
AE(s)	7	5	2

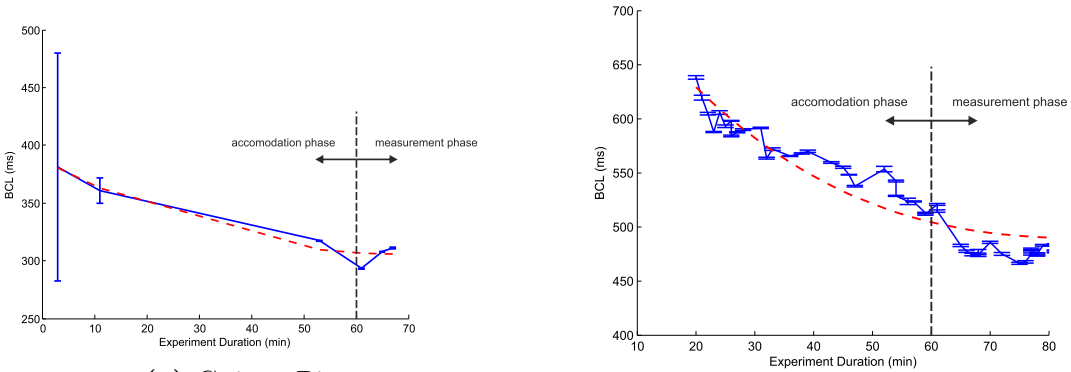

(a) Guinea Pig

(b) Rabbit

Figure 5.2.: Accommodation of BCL. Results shown in blue is BCL as $mean \pm std$ for consecutive recordings. Red curve is a fitted polynomial of 3^{rd}-order.

For experiments without early intervention (pacing, drugs), overall BCL was calculated as $mean \pm std$ from all signal recordings obtained during the experiment. Mean BCL over all experiments was calculated separately for rabbit and guinea pig using

equation (3.8). Pooled mean BCL from 19 rabbit atria was 468.25 ± 99.99 ms and 366.34 ± 170.80 ms for guinea pig atria. Large standard deviation in guinea pig atria results from a small sample number (only 3 included, rest excluded because of intervention) with one very bradycard specimen (BCL $= 579.32 \pm 74.74$ ms). Detailed results are listed in Appendix A.5. Typical accommodation behavior obtained from 2 experiments is shown in Figure 5.2.

5.3. Arrhythmic Episodes During Accommodation

In 5 preparations paroxysmal episodes of tachyarrhythmias were observed. These episodes terminated themselves within minutes without any intervention (see Figure 5.3). In one experiment the arrhythmic episode revealed alternans and possibly reentry during the accommodation phase.

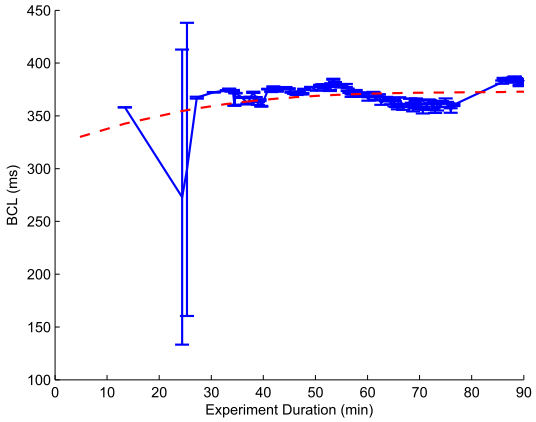

Figure 5.3.: Arrhythmic episode during BCL accommodation. Between 24 min and 26 min an arrhythmic episode occurred. The episode terminated spontaneously.

Two sensors were placed in the ROI, one in the proximal section of a pectinate muscle (recording position P) and one in the lower central section of a neighboring pectinate muscle (recording position C). During the arrhythmic episode BCL alternated between a long interval $LI = 449.1 \pm 0.9$ ms and a short interval $SI = 157.6 \pm 1.1$ ms. Direction of conduction was estimated from the vector loop VL at time instant LAT. $\alpha_{E,LAT}$ showed retrograde conduction in the ROI during the short interval. This is consistent with the local activation times at both recording positions, i.e. at LI position P is activated prior to position C and vice versa for SI. Recording positions and signal waveforms are shown in Figure 5.4.

All signal parameters showed alternating behavior between long and short BCL interval. Results are listed in Table 5.3. After approximately 2 minutes the arrhythmic episode spontaneously terminated and BCL remained at 370.9 ± 9.1 ms for the next 120 minutes (preparation was electrically paced afterwards).

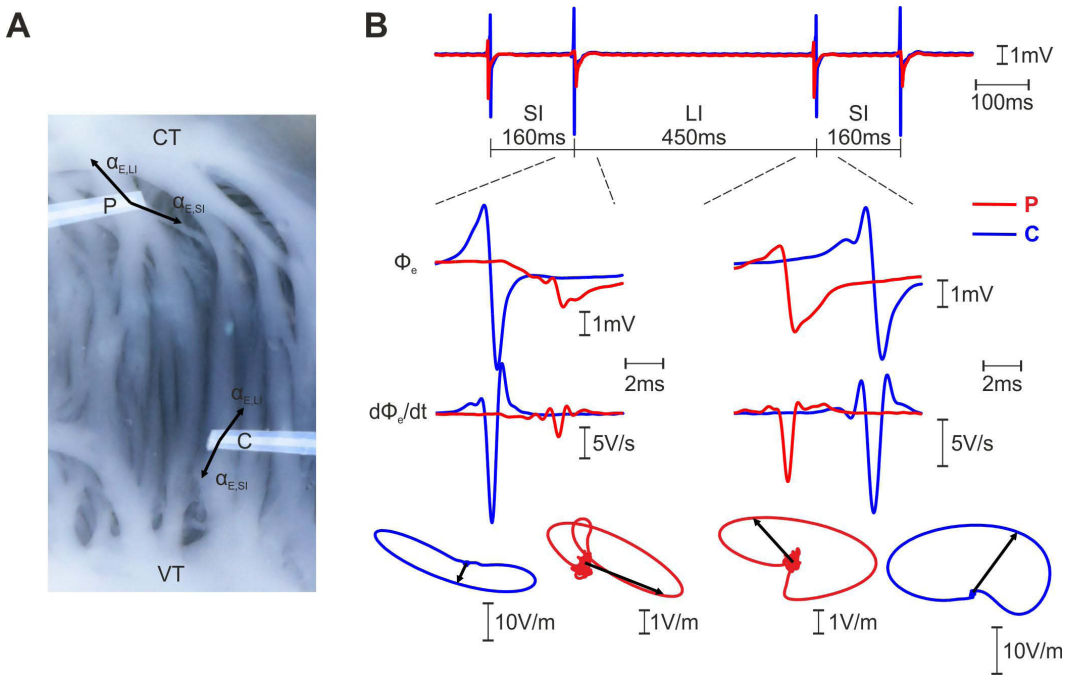

Figure 5.4.: Arrhythmic episode. (**A**) Signals were recorded at positions C (central) and P (proximal). (**B**) BCL alternated between a short interval SI and a long interval LI. At SI latency between P and C and $\alpha_{E,LAT}$ in VL (black arrows) revealed retrograde conduction.

Table 5.3.: Signal parameters evaluated from 32 consecutive beats during arrhythmic episode. Values are *mean* $\pm$ *std.* LI, Long Interval; SI, Short Interval

Parameter		**proximal**		**central**	
		LI	**SI**	**LI**	**SI**
Φ_{PP}	mV	3.21 ± 0.05	2.01 ± 0.03	5.78 ± 0.05	7.25 ± 0.08
$\dot{\Phi}_{min}$	$\mathrm{V\,s^{-1}}$	-7.27 ± 0.15	-3.64 ± 0.13	-10.80 ± 0.13	-18.01 ± 0.23
E_{max}	$\mathrm{V\,m^{-1}}$	3.57 ± 0.13	4.57 ± 0.17	19.68 ± 0.31	26.92 ± 0.49
LCV	$\mathrm{m\,s^{-1}}$	1.79 ± 0.05	1.02 ± 0.03	0.58 ± 0.01	1.63 ± 0.03
t_{depol}	ms	0.82 ± 0.01	0.59 ± 0.01	0.88 ± 0.01	0.70 ± 0.01
a		-0.48 ± 0.01	-0.72 ± 0.02	-0.18 ± 0.01	-0.24 ± 0.01
$\alpha_{E,LAT}$	°	138.10 ± 2.60	-19.10 ± 2.10	50.10 ± 1.00	-73.30 ± 3.60
		LI		**SI**	
ΔLAT_{CP}	ms	4.58 ± 0.07		-3.61 ± 0.04	

5.4. Beat-to-Beat Behavior During Sinus Rhythm

A prerequisite for time-serial activation mapping as performed in this work is the stability of excitation spread and conduction parameters during the mapping procedure. Signal analysis showed that extracellular parameters have a highly accurate beat-to-beat behavior for consecutive beats (short term stability). Table 5.4 shows short term stability of signal parameters from 255 beats (111.7 s) recorded at 2 positions after an experiment duration of 130 min in a rabbit atrial tissue preparation.

Stability of extracellular parameters for an extended period of time strongly depends on oxygen supply of the tissue preparation. For tissue preparations with sufficient small diameter superfusion as performed in our laboratory is an adequate method to keep the tissue viable. Early studies (Wilensky et al., 1986) have shown that myocytes are unaffected in depths of 100 – 600 µm but suffer from ischemia in greater depths. A recent computer simulation study (Campos, Prassl, et al., 2012) showed that extracellular potentials Φ_e in a pectinate muscle fiber of 1 mm diameter with an ischemic core of 0.250 mm diameter change only by a few percent. Therefore, it is assumed that in typical atrial tissue preparations (diameter of PectM 0.68 ± 0.32 mm in rabbit, much smaller in guinea pig) extracellular parameters remain stable even if the core of muscle fibers suffer from ischemia.

Table 5.4.: Short term stability of extracellular parameters. 255 consecutive beats were analyzed after 130 min experiment duration. Values are $mean \pm std$. For BCL the range is indicated in square brackets.

Parameter	Recording Position A		Recording Position B	
Φ_{PP}	3.60 ± 0.11	mV	3.65 ± 0.21	mV
$\dot{\Phi}_{min}$	-9.54 ± 0.34	$\mathrm{V\,s^{-1}}$	-9.68 ± 0.57	$\mathrm{V\,s^{-1}}$
LCV	0.98 ± 0.01	$\mathrm{m\,s^{-1}}$	1.25 ± 0.09	$\mathrm{m\,s^{-1}}$
$\alpha_{E,LAT}$	342.57 ± 0.46	°	220.27 ± 4.63	°
E_{max}	13.81 ± 0.38	$\mathrm{V\,m^{-1}}$	16.14 ± 1.45	$\mathrm{V\,m^{-1}}$
LAT	15.92 ± 0.07	ms	19.11 ± 0.04	ms
t_{depol}	0.64 ± 0.01	ms	0.64 ± 0.01	ms
a	0.31 ± 0.05		0.05 ± 0.05	
BCL	438.18 ± 10.97	ms	[420.43 ms	459.92 ms]

5.5. Conduction within the ROI

5.5.1. Representative Signal Waveforms and Histology

For illustration representative types of signal waveforms from recording sites in the pectinate muscle network were selected: Figure 5.5a shows a non-fractionated, symmetrical electrogram recorded in the central segment of PectM. VL is very narrow indicating almost planar excitation wavefront. The electrogram shown in Figure 5.5b was recorded in the proximal section of PectM and clearly shows two distinct activation wavefronts in $\dot{\Phi}_e$. Arrows drawn in VL at the two distinct LATs reveal different directions of activation wavefronts. A highly fractionated electrogram from the proximal section of PectM is shown in Figure 5.5c.

A representative histological section is shown in Figure 5.6. Myocytes in PectM are oriented parallel with aligned fibrotic inlays. Transition from PectM into VB is characterized by complex microstructure with sudden changes in fiber orientation and crossing fibers.

Merging areas of distinct pectinate muscles are of particular interest because they represent collision sites for independently spreading excitation wavefronts. Figure 5.7 shows signal recordings taken at a merging area which revealed 2 activation events. The earlier event was dominant with deflections around LAT. These deflections most likely were artifacts since peak differences lie within the noise level ϵ. Therefore, a mean value for LAT_1 was determined. The later event was separated more clearly and also was present as side lobe in the VL. Direction of excitation spread $\alpha_{E,LAT}$ of the 2 activation events agreed with macroscopic structures, i.e. the earlier event approaching from the larger pectinate muscle above the recording site and the later event approaching from one of the smaller muscle fibers on the right of the recording site.

5.5.2. Statistical Analyses

All signal recordings from 17 rabbit atrial tissue preparations were classified into their corresponding region of recording site: Crista Terminalis (CT), Pectinate Muscle (PectM), or Vestibule (VB). Signal recordings from PectM were further classified into sections: proximal (p), central (c), and distal (d). The number of recordings for each area are listed in Table 5.5. For each recording within the ROI signal parameters were

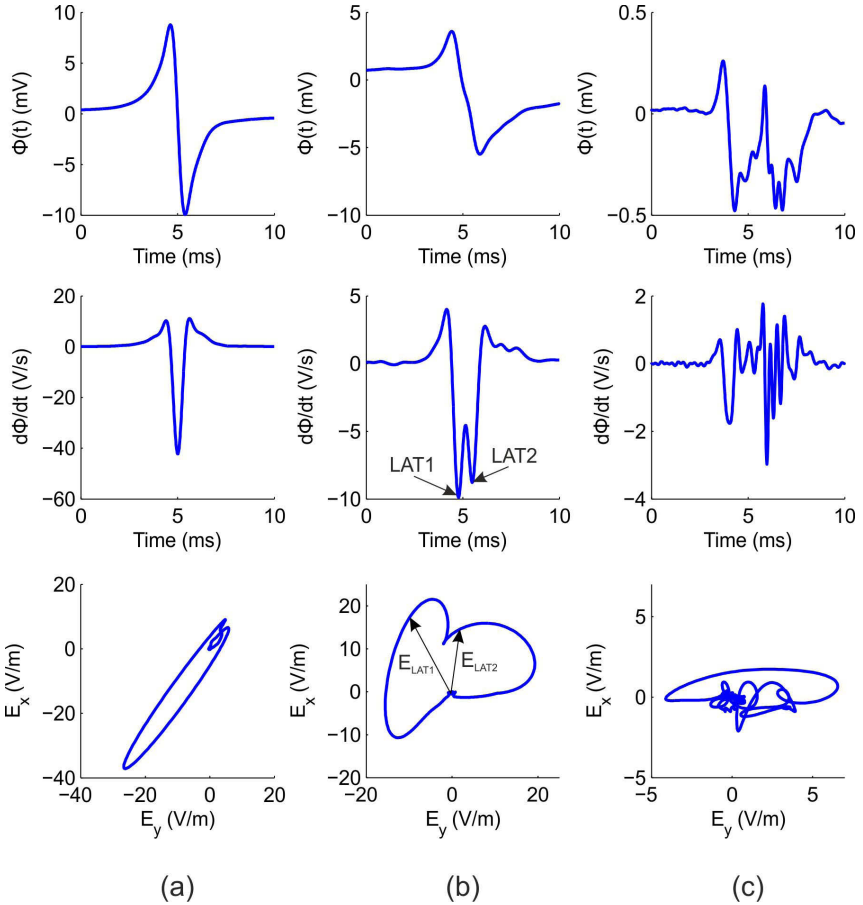

Figure 5.5.: Representative signal waveforms. (a) Uniform Φ_e with $FI = 1$, (b) wavefront segmentation with $FI = 2$, (c) complex fractionated Φ_e.

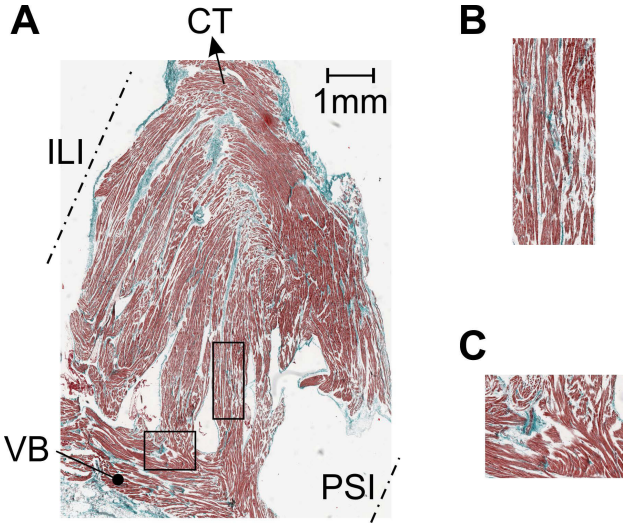

Figure 5.6.: Representative histology of a rabbit atrium with Masson's trichrome staining. (**A**) Histological section of the CTI. Rectangles are shown in detail on the right. (**B**) In PectM cells are parallel oriented with aligned fibrotic inlays. (**C**) Microstructure of VB is complex with sudden changes in fiber direction and crossing fibers.

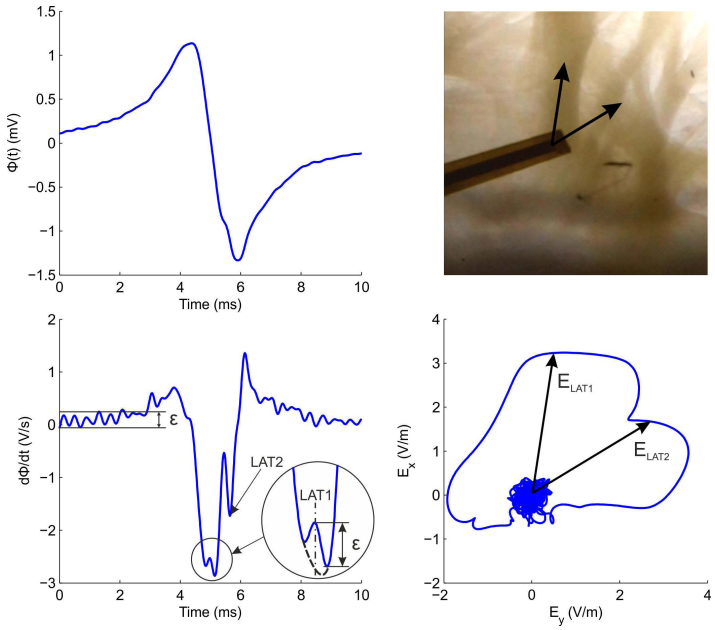

Figure 5.7.: Characteristic electrogram at a merging area in the distal section of a PectM. First peak in $\dot{\Phi}_e$ shows fractionation but peak difference lies within noise ϵ.

calculated. LCV was calculated only for recordings with $FI = 1$. $LCV > 5$ was not included and $FI > 10$ was coerced to $FI = 10$. For FI and a results are plotted as histograms in Figure 5.9 and 5.10. For a bins in histograms were selected to range from -1 to -0.3 for starting potentials, -0.3 to $+0.3$ for free running potentials, and $+0.3$ to $+1$ for ending or colliding potentials as described in Section 2.6.3. Statistical analysis was performed in MATLAB™. Boxplots of parameter distribution are shown without outliers for better readability. Original plots can be found in Appendix A.5.

Table 5.5.: Number of recording positions in regions of the CTI and in subregions of PectM.

Region	Quantity
CT	205
PectM	837
VB	248

Section	Quantity
proximal	162
central	468
distal	207

Regions within CTI

No evaluated parameter showed normal distribution in any region of the CTI. Hence, parameters were compared using a Mann-Whitney U-test as described in Section 3.7.

All parameters showed statistically significant differences between the CTI regions. LCV was statistically significant different only between CT and PectM. Largest signal amplitudes of Φ_{PP}, $\dot{\Phi}_{min}$, and E_{max} were found in PectM. LCV was highest in CT and t_{depol} was longest in VB. Variance was large in all evaluated parameters, especially in PectM where exceptionally large amplitudes in Φ_{PP}, $\dot{\Phi}_{min}$, and E_{max} were observed. Results are shown in Figure 5.8.

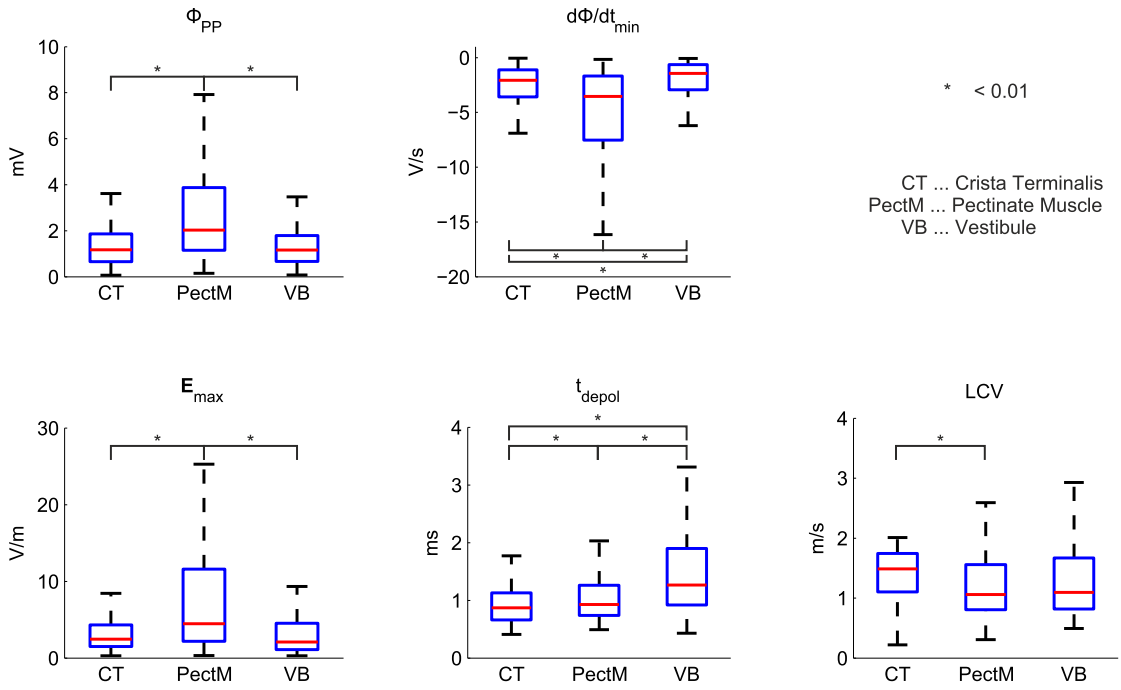

Figure 5.8.: Distribution of parameters in regions of CTI. All parameters except LCV showed statistically significant differences between CTI regions.

FI distribution (Figure 5.9) revealed characteristic differences between regions of CTI. In CT most recordings showed $FI = 1 - 5$. In PectM non-fractionated signals were predominant (52.4 %). In VB a large fraction of recordings showed $FI = 1$, but percentage of extremely high fractionated recordings with $FI \geq 10$ was the largest of all regions (9.27 %). Waveform symmetry a (Figure 5.10) indicated equal numbers of free running activation wavefronts in all regions of CTI. However, in CT fraction of starting wavefronts and in VB fraction of ending/colliding wavefronts were largest.

Sections within PectM

No parameter showed normal distribution in the sections of PectM. Hence, parameters were compared using a Mann-Whitney U-test as described in Section 3.7. Statistically

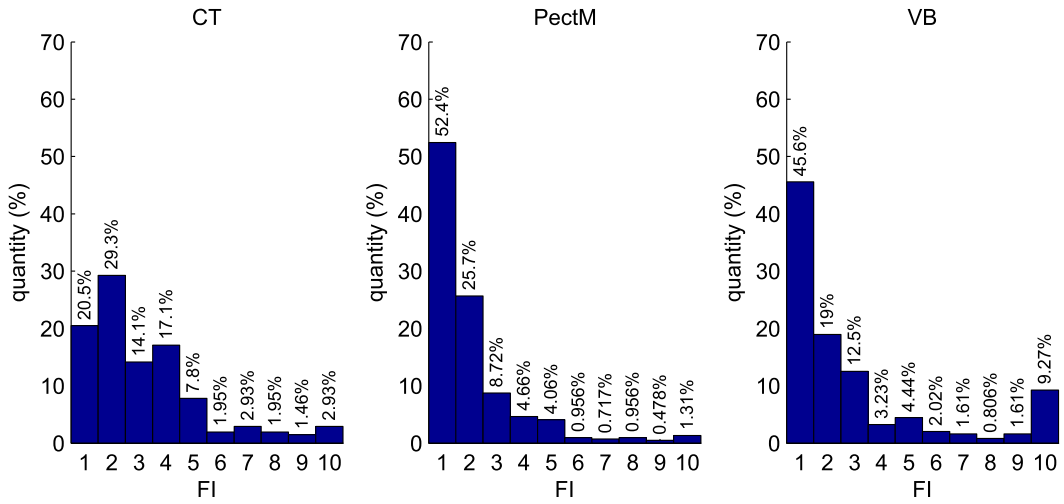

Figure 5.9.: Distribution of FI in regions of CTI. In PectM $FI = 1 - 2$ was dominant. In VB the percentage of highly fractionated waveforms with $FI \geq 10$ was largest.

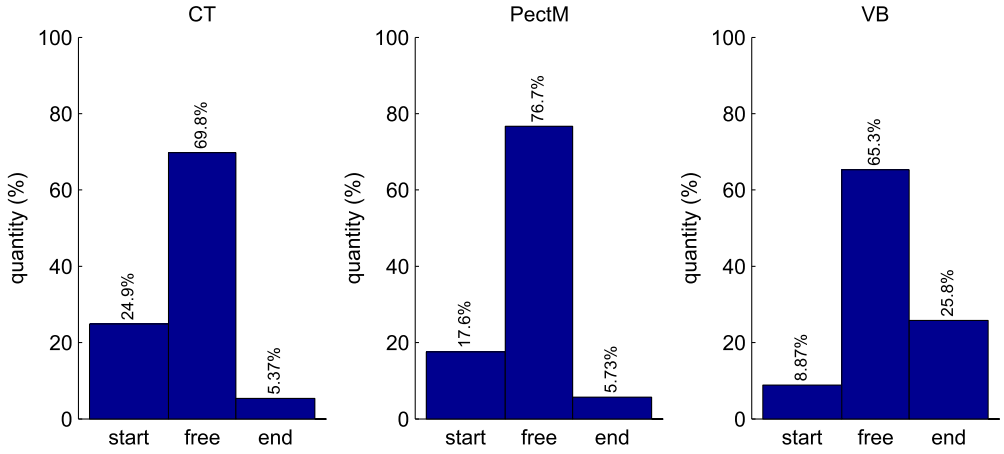

Figure 5.10.: Distribution of waveform symmetry a in regions of CTI. In CT the fraction of starting potentials and in VB the fraction of ending or colliding potentials was highest.

significant differences were only found for $\dot{\Phi}_{min}$ between central and distal section and for t_{depol} between central and distal and proximal and distal sections. Maximum amplitudes of Φ_{PP}, $\dot{\Phi}_{min}$, and E_{max} were found in the central section. t_{depol} was longest in the distal section. LCV was almost equally distributed in the different sections. Results are shown in Figure 5.11.

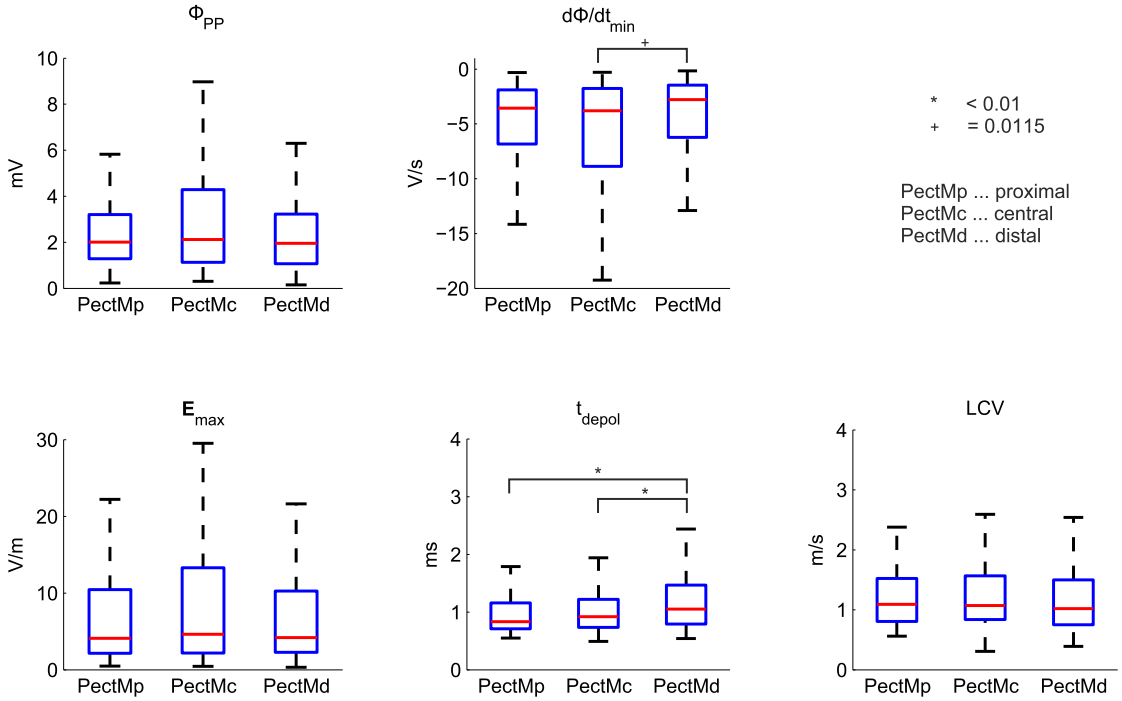

Figure 5.11.: Distribution of parameters in PectM sections. Only t_{depol} and $\dot{\Phi}_{min}$ showed statistically significant differences.

Distribution of FI was almost identical in the PectM sections as shown in Figure 5.12. In the proximal section the fraction of starting wavefronts was largest (32.7 %). Apart from that distibution of a was comparable between sections.

5.6. Signals in Macroscopic Uniform Structures

Figure 5.14 illustrates the case of a small pectinate muscle merging with a larger one. Signal recordings along the larger PectM showed electrograms with pronounced different characteristics, ranging from uniform with $FI = 1$ to fractionated with $FI \geq 2$, despite the macroscopic well defined cable-like structure. At the left border of the PectM electrograms are mainly uniform suggesting well coupled underlying myocytes.

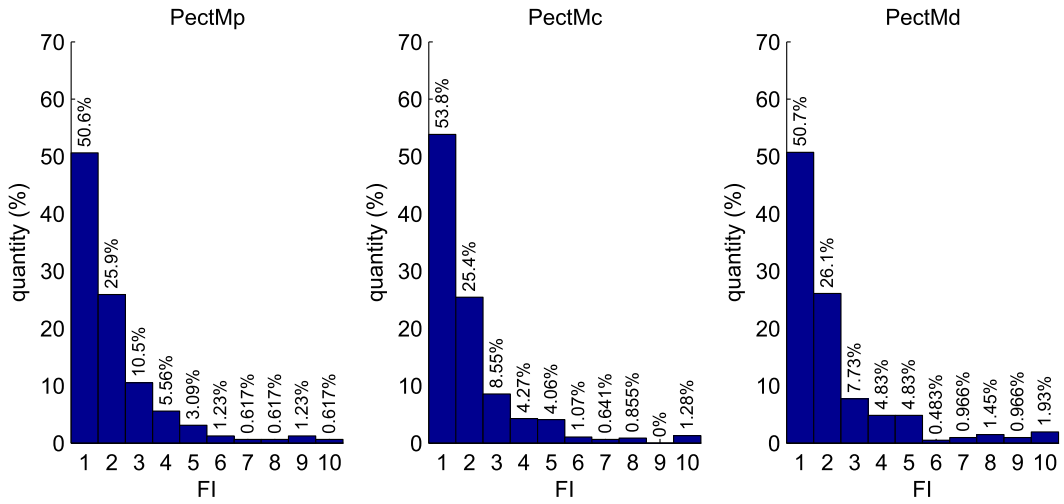

Figure 5.12.: Distribution of FI in sections of PectM. In all sections $\approx 75\,\%$ of the recordings showed $FI = 1 - 2$.

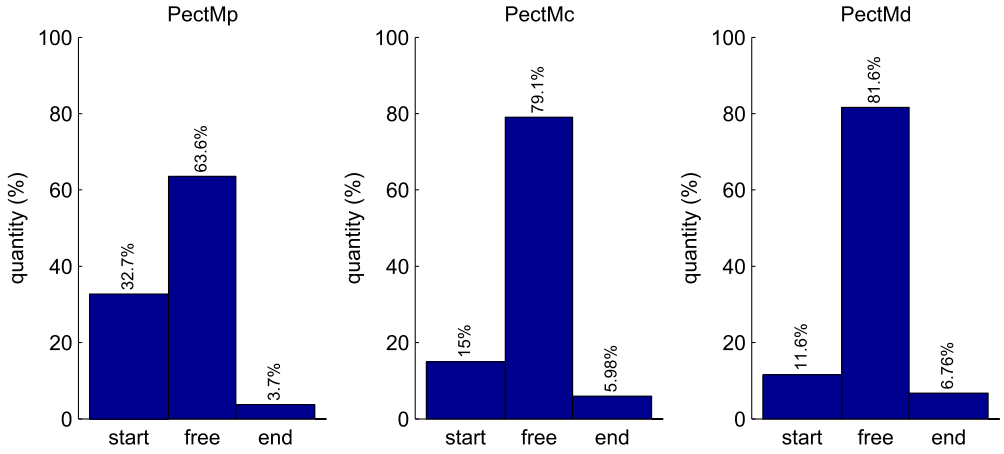

Figure 5.13.: Distribution of waveform symmetry a in sections of PectM. In the proximal section fraction of starting potentials was highest.

Towards the right border electrograms become increasingly fractionated, indicating complex underlying microstructure and wavefront collision due to the oblique merging of the smaller PectM from the right.

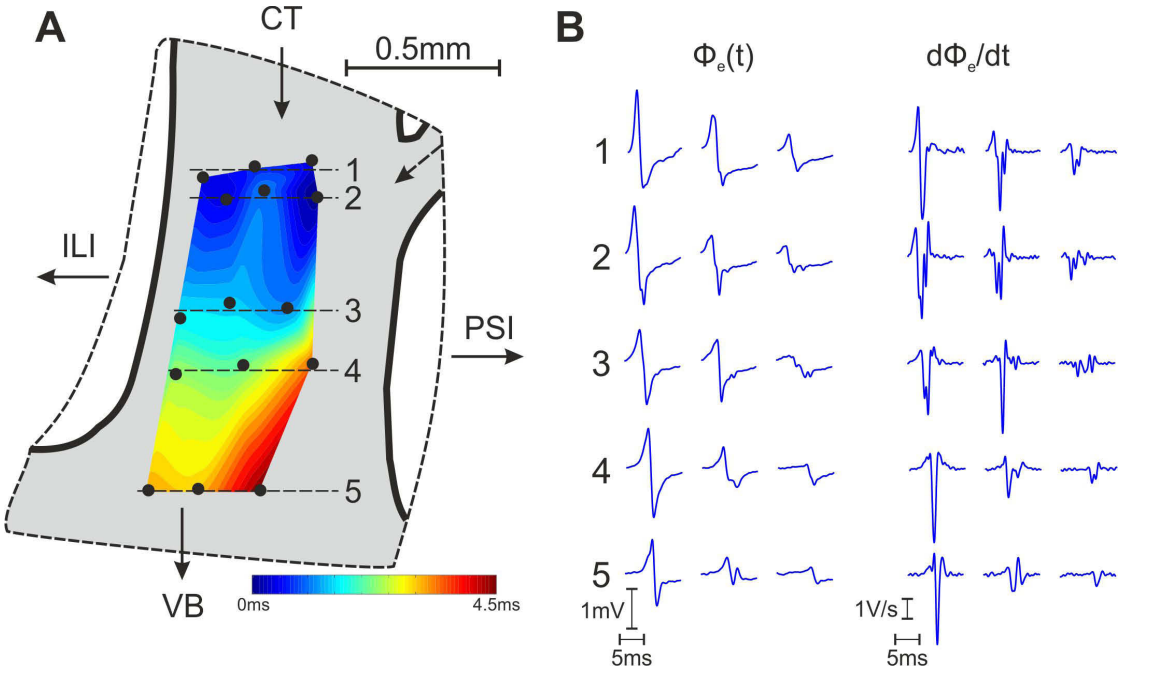

Figure 5.14.: Conduction in a macroscopic uniform structure. A merging pectinate muscle (dashed arrow) causes wavefront collision and fractionation of Φ_e. (**A**) Geometry and activation map. Recording sites were along 5 lines across the PectM. (**B**) Φ_e and $\dot{\Phi}_e$ at lines 1 – 5. ILI, inferolateral isthmus; PSI, paraseptal isthmus; CT, Crista Terminalis; VB, Vestibule.

5.7. Initiation Sequence of the Pectinate Network

In 5 rabbit atrial tissue preparations the initiation sequence of neighboring PectMs was determined as described in Section 3.6.3. The obtained activation and arrival sequences were not ordered in any form but rather seemed to be arbitrary. The arrival time in the VB is a function of activation sequence, PectM length, and conduction velocity in the PectM and can therefore be related to the initiation sequence.

Table 5.6 shows an evaluation of the initiation sequence in a rabbit atrial tissue preparation. With activation time LAT_p, PectM length along the center line l, and mean conduction velocity CV along PectM the transition time through the PectM, Δt, was calculated. CV was evaluated with linear regression from LATs along the PectM as

shown in Arnold, Wiener, Sanchez-Quintana, et al. (2011).
Calculated and measured arrival sequence, $A_{i,C}$ and $A_{i,M}$, agreed to each other although calculated and measured activation times $LAT_{d,C}$ and $LAT_{d,M}$ differed by a few ms. This is presumably because of inaccuracy of mean conduction velocity CV.
The initiation sequence was quantified by calculating the displacement variance VAR_d according to equation (3.6). VAR_d together with the maximum displacement variance for the according initiation sequence $VAR_{d,max}$ is listed in Table 5.7.

Table 5.6.: Evaluation of initiation sequence in a rabbit atrial tissue preparation. I, initiation index; A, arrival index; p, proximal; d, distal; E, expected; M, measured; C, calculated.

$\mathbf{I_{i,E}}$	$\mathbf{I_{i,M}}$	$\mathbf{LAT_p}$ ms	**l** mm	**CV** $\mathrm{m\,s^{-1}}$	$\mathbf{\Delta t}$ ms	$\mathbf{LAT_{d,C}}$ ms	$\mathbf{A_{i,c}}$	$\mathbf{LAT_{d,M}}$ ms	$\mathbf{A_{i,M}}$
1	4	10.0	11.3	1.20	9.4	19.4	4	16.60	4
2	2	4.8	7.5	0.71	10.6	15.4	2	15.05	2
3	1	3.4	5.8	0.45	12.9	16.3	3	15.80	3
4	3	6.2	5.7	0.63	9.0	15.2	1	13.69	1

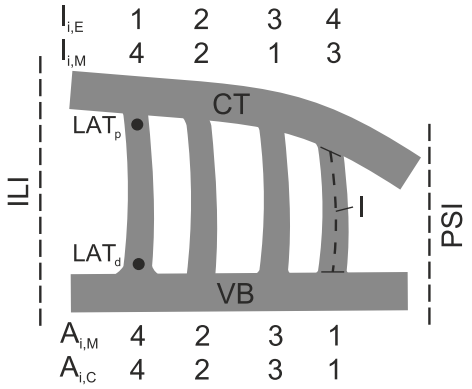

Figure 5.15.: Initiation sequence and parameters as shown in Table 5.6.

Table 5.7.: VAR_d for 5 rabbit atria according to equation (3.6).

Sequence	$\mathbf{VAR_d}$	$\mathbf{VAR_{d,max}}$
2431	3.5	5
312	2.0	2.67
2 374 516	6.3	16
4213	3.5	5
54 213	6.8	8

5.8. Retrograde Conduction During Sinus Rhythm

In 6 rabbit atrial preparations retrograde conduction in individual PectMs during sinus rhythm was observed. In 3 preparations retrograde conduction was persistent, in 1 preparation it occurred during accommodation of BCL (between 0 – 50 min, preparation was paced afterward, no follow-up measurements), and in 2 preparations retrograde conduction was caused by arrhythmic episodes (tachycardia). Figure 5.16 illustrates this phenomenon in a preparation with persistent retrograde conduction. Macroscopic structure showed several very thin ($\approx 100 - 200\,\mu m$) parallel pectinate muscles within

the ROI. Recording sites were arranged along 2 parallel PectM branches as shown in Figure 5.16B.

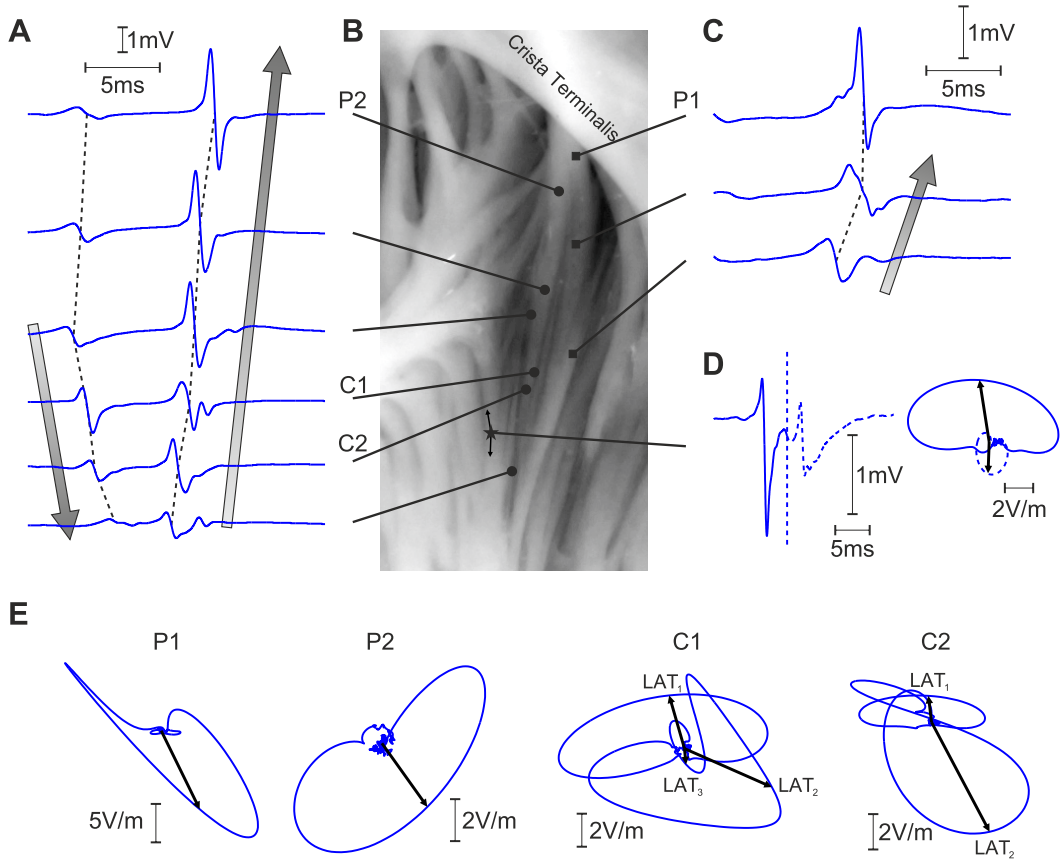

Figure 5.16.: Retrograde conduction during sinus rhythm. (**A**) Φ_e recorded in left fiber branch showed retrograde conduction. Remote antegrade activation events were present. (**B**) Tissue preparation and recording positions. (**C**) Φ_e recorded in right fiber branch again showed retrograde conduction. (**D**) Neighboring pectinate muscles clearly showed antegrade and retrograde conduction. (**E**) VL at proximal recording sites P1, P2 and in central section C1, C2. Arrows point towards $\alpha_{E,LAT}$.

Signal recordings in the PectM branch on the left (Figure 5.16A) comprised two separated activation events. Appearance of the two events in recordings along the PectM revealed antegrade conduction for the earlier event and retrograde conduction for the later. Signal recordings in the PectM branch on the right (Figure 5.16C) showed one activation event with retrograde conduction.

At a recording site to the left of the branches (asterisk in Figure 5.16B) Φ_e again showed two separated activation events. VL revealed two distinct loops with opposite direction of wavefront spread. The earlier deflection in Φ_e (larger in Φ_e and VL and

therefore most likely a local event) described antegrade conduction whereas the later deflection described retrograde conduction (most likely a remote event from the PectM to the right).
Figure 5.16E illustrates VLs from the proximal and central parts of the measured parallel PectM strands. VLs in the proximal sections P1 and P2 clearly showed retrograde conduction. VLs at C1 and C2 exhibited multiple loops with different directions. In both recordings the earlier activation at LAT_1 showed antegrade conduction which is in accordance to signal recordings shown in Figure 5.16A. The later events at $LAT2$ (and LAT_3 in C1) showed retrograde conduction again in accordance to the direction of excitation spread determined in Figure 5.16A.

5.9. Intracellular Measurements

Intracellular recordings of APs were performed as described in Section 3.4. In one rabbit right atrial tissue preparation transmembrane voltage V_m was recorded along the CT at the ILI, CI, and PSI. The number of recorded and evaluated beats was 6 at ILI, 15 at CI, and 8 at PSI. At the CI motion artifacts are present and determination of APD_{90} becomes inaccurate. APD_{90} was highest at CI and lowest at ILI. APD_{50} was almost identical at all 3 recording sites. V_{rest} and $\dot{V}_{max}$ differed largely between recording sites from -50 to $-90\,\mathrm{mV}$ and from 100 to $200\,\mathrm{V\,s^{-1}}$, respectively.
In the same tissue preparation V_m was recorded in the VB. APD_{90} and APD_{50} were significantly shorter than in CT. Signals recorded in the area of the SAN (different rabbit right atrial tissue preparation) showed diverse signal waveforms and spontaneous diastolic depolarization. Signal waveforms shown in Figure 5.17 were averaged over recorded beats. In Table 5.8 parameters obtained from V_m are listed.

Table 5.8.: AP parameters along CT from signal recordings in Figure 5.17. Number of evaluated beats were: ILI 6, CI 15, PSI 8, VB 15, and SAN 25.

Parameter	**Location**				
	ILI	**CI**	**PSI**	**VB**	**SAN**
V_{rest} (mV)	-52.87 ± 2.05	-66.09 ± 1.50	-90.26 ± 1.03	-73.78 ± 1.05	-70.75 ± 0.35
V_{OS} (mV)	13.29 ± 0.59	18.88 ± 0.49	23.15 ± 0.97	10.38 ± 1.85	22.55 ± 0.32
$\dot{V}_{max}$ ($\mathrm{V\,s^{-1}}$)	102.28 ± 7.93	125.39 ± 3.26	199.64 ± 0.84	135.96 ± 4.09	66.28 ± 0.39
APD_{90} (ms)	80.53 ± 8.92	126.39 ± 26.87	110.58 ± 2.40	44.47 ± 2.55	116.29 ± 0.52
APD_{50} (ms)	25.52 ± 0.36	25.49 ± 0.23	24.89 ± 0.27	12.63 ± 0.15	75.47 ± 0.40
BCL (ms)	365.38 ± 1.60	360.38 ± 0.76	365.17 ± 1.32	359.30 ± 2.16	401.90 ± 1.37

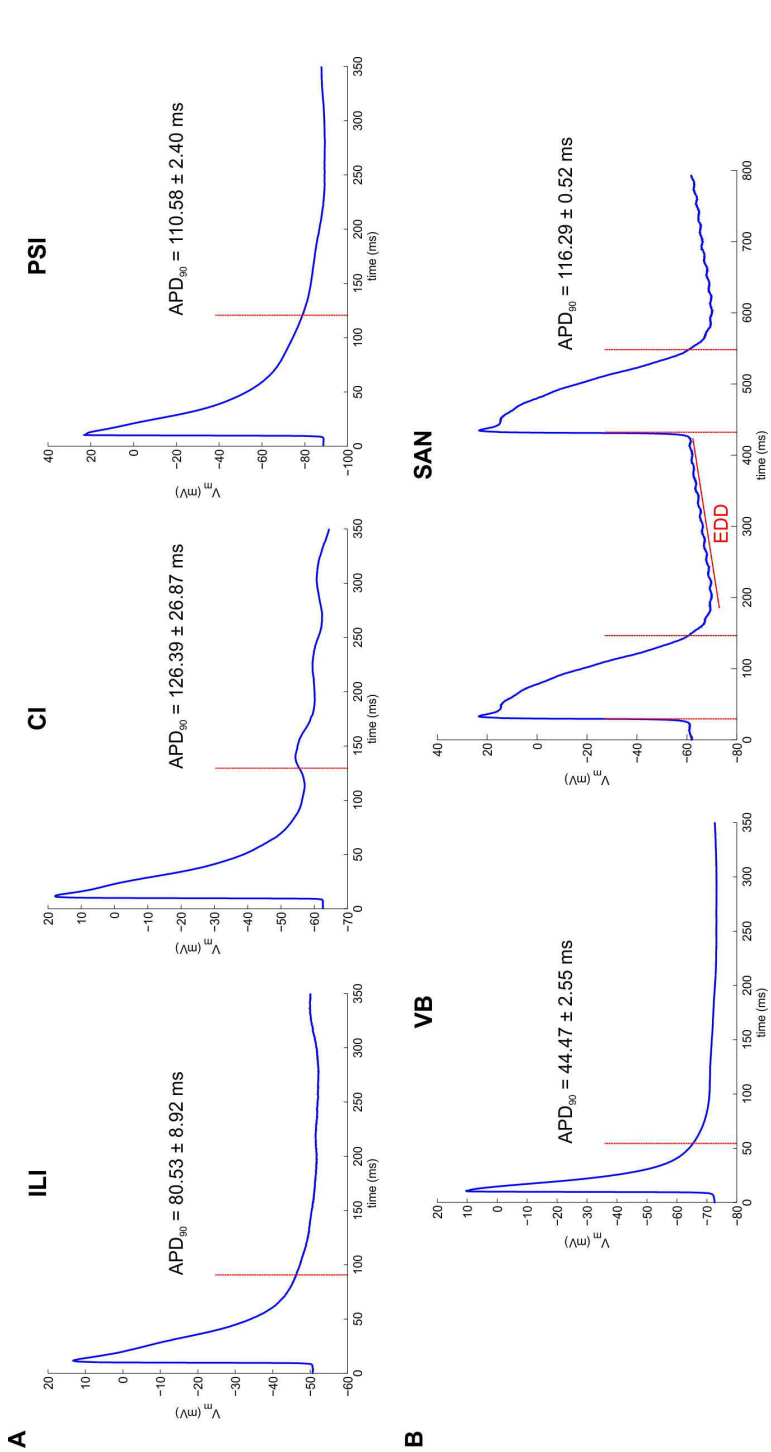

Figure 5.17.: **(A)** AP recordings along CT at ILI, CI, and PSI. **(B)** Recordings in VB and SAN. ILI, infero-lateral isthmus; CI, central isthmus; PSI, paraseptal isthmus; VB, vestibule; SAN, sinoatrial node. Note motion artifacts in CI and spontaneous early diastolic depolarization (EDD) in SAN.

6. Pacing

In this chapter results from electrical stimulation of tissue preparations are presented. The different dynamics of pacing protocols and principles of electrical impulse delivery were described in Section 3.5.1.

Different types of pacing protocols were applied: ramp-like (Ramp), stair-like (Stair), and premature beat (Premature). Altogether protocols were applied 165 times. Pacing was applied in antegrade and retrograde direction which refers to direction of excitation spread during sinus rhythm, i.e from CT towards VB in atrial tissue preparations. For papillary muscle preparations antegrade refers to pacing at the basis and retrograde to pacing at the head. 33 recordings had to be excluded because of autorhythmic activity interfering with pacing.

6.1. Determination of Conduction Block

For all 132 recordings included in analysis the index of earliest occurrence of conduction block S_b and the corresponding PCL which failed to trigger activation was determined. The value of PCL is equivalent to the effective refractory period, ERP. In 24 recordings no conduction block occurred down to a minimum PCL of 50 ms. These protocols were additionally excluded and the pacing protocol was repeated with PCL_{end} set to 20 ms. In Table 6.1 number and type of included and excluded recordings are listed.

Figure 6.1 shows results for the earliest occurrence of conduction block divided into type and direction of pacing protocol (concatenated for guinea pig and rabbit). No dataset showed normal distribution and thus datasets were compared using a Mann-Whitney U-test as described in Section 3.7. The only statistically significant difference

Table 6.1.: Number of recordings and type of pacing protocols included in analysis. RA, right atrium; PM, papillary muscle; dir, direction; a, antegrade, r, retrograde; num, number of recordings; excl, number of excluded recordings.

Type	Rabbit tissue	dir	num	excl	Guinea Pig tissue	dir	num	excl	Total
Ramp	RA	a	18	1	RA	a	11	6	22
		r	11	2		r	11	2	18
	PM	a	0	0	PM	a	13	2	11
		r	0	0		r	2	1	1
			29	3			37	11	**52**
Stair	RA	a	9	3	RA	a	4	0	10
		r	6	1		r	3	0	8
	PM	a	0	0	PM	a	14	0	14
		r	0	0		r	4	0	4
			15	4			25	0	**36**
Premature	RA	a	4	1	RA	a	3	0	6
		r	4	1		r	0	0	3
	PM	a	0	0	PM	a	13	4	9
		r	0	0		r	2	0	2
			8	2			18	4	**20**
Total			**52**	**9**			**80**	**15**	**108**

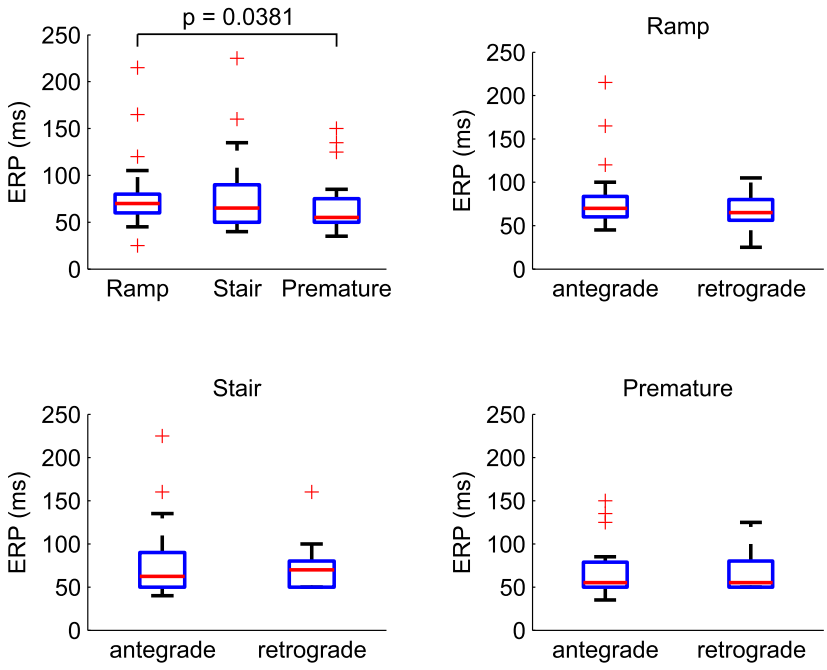

Figure 6.1.: Occurrence of conduction block analyzed for all types of tissue preparations.

was present between overall occurrence of conduction block in ramp-like pacing protocols and premature beat pacing protocols ($p = 0.0381$). Between species statistically significant differences were only found for application of ramp-like pacing protocols. Results separated for species are shown in Appendix A.6.

6.2. Beat-to-Beat Behavior of Pacing Protocols

Beat-to-beat behavior of the applied pacing protocols showed different characteristics and thus was classified into three types of responses: (i) nonlinear, (ii) alternating, and (iii) spontaneous block.
Ramp-like pacing protocols typically resulted in nonlinear beat-to-beat changes whereas stair-like pacing protocols exhibited alternans during the final phase close to conduction block. S2 stimuli of premature beat pacing protocols developed in a similar manner as ramp-like protocols, i.e. nonlinear. Spontaneous conduction block occurred mostly during stair-like pacing. 4 pacing protocols could not be uniquely classified. Responses are listed in Table 6.2.

Table 6.2.: Responses of applied pacing protocols. NL, nonlinear; A, alternans; S, spontaneous; N, not classified.

Type	**NL**	**A**	**S**	**N**
Ramp	52	0	0	0
Stair	4	21	8	3
Premature	18	0	2	0
Sum	**74**	**21**	**10**	**3**

6.2.1. Analysis

Parameter development was comparable between rabbit tissue and guinea pig tissue and therefore was analyzed combined (species-independent). Results for species-dependent evaluation are shown in Appendix A.7.

For each pacing protocol n beats before conduction block S_b arises were selected for analysis. CNF parameters estimated from extracellular signal recordings were standardized to the first beat of the pacing protocol. Results are shown as deviation from first beat in percent for Φ_{PP}, $\dot{\Phi}_{min}$, E_{max}, LAT, LCV, and t_{depol}. For a and $\alpha_{E,LAT}$ deviations were calculated in absolute values (in degree for $\alpha_{E,LAT}$).

CNF parameters from all corresponding pacing responses were grouped according to their position relative to conduction block S_b as described in Section 3.5.2. Thus n pre-block parameter groups were gathered. No parameter cluster showed normal distribution (Kolmogorov-Smirnov test, $\alpha \leq 0.05$) and therefore pre-block beats were compared using a Mann-Whitney U-test with $\alpha \leq 0.05$.

6.2.2. Pre-block Behavior of Ramp-like Pacing Protocols

52 ramp-like pacing protocols were applied (cf. Table 6.2). The final phase of all ramp-like pacing protocols showed nonlinear beat-to-beat changes of signal parameters. The majority of development curves showed weak pacing rate dependency (PRD) for the first stimuli of the applied pacing protocol and strong PRD for the last 15 – 20 beats. During the early phase (EP) of pacing protocols parameters exhibited excursions from weak PRD in some cases. Figure 6.2 shows two parameter development curves with strong nonlinear PRD in the final phases and parameter excursions in the EP of one parameter development curve.

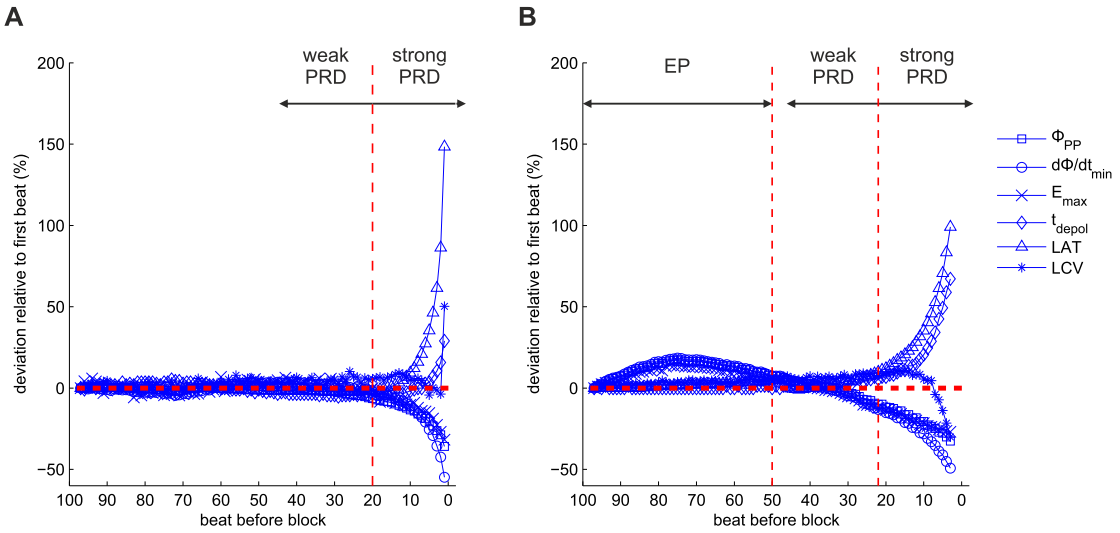

Figure 6.2.: Pacing rate dependency (PRD) for 2 ramp-like pacing protocols. Both protocols showed strong PRD for the last 20 beats before conduction block. (**A**) During EP only weak PRD was present. (**B**) EP with excursion from weak PRD was present for Φ_{PP}, $\dot{\Phi}_{min}$, and E_{max}.

Development of signal waveforms during a typical nonlinear final phase are shown in Figure 6.3. Signal parameters were affected distinctly by decreased PCL: Φ_{PP}, $\dot{\Phi}_{min}$, and E_{max} decreased while LAT and t_{depol} increased. $\alpha_{E,LAT}$ changed only minor by

$< 6°$. Waveform symmetry a of the last beat before conduction block dropped by 0.15 to a more negative value, suggesting increased sink-source mismatch. LCV was almost constant for the entire pacing protocol but suddenly increased by 50 % at the last beat. This is most likely a calculation error because the negative peak in $\dot{\Phi}_e$ flattens, indicating upcoming fractionation and thus LAT determination is ambiguous.

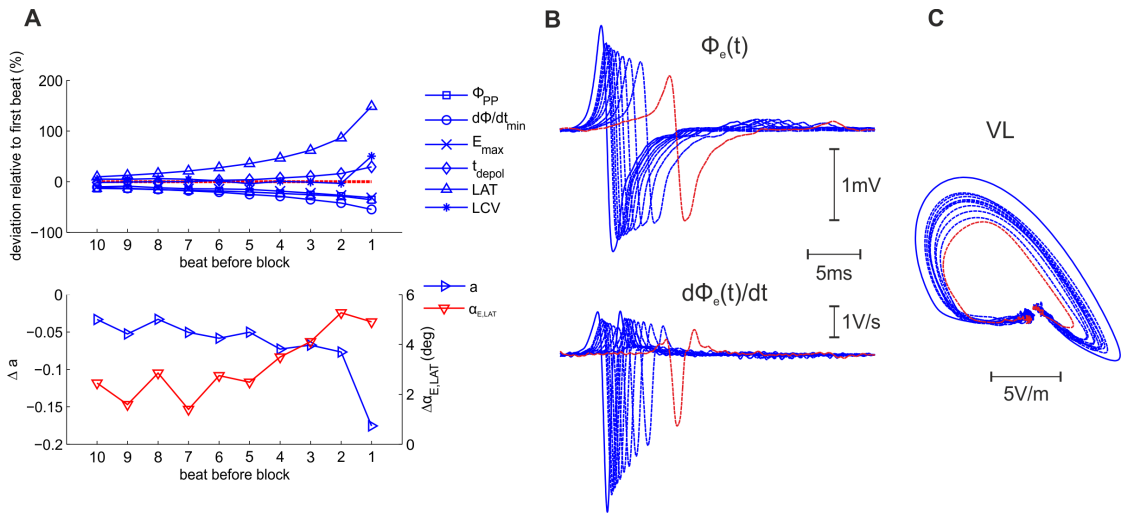

Figure 6.3.: Nonlinear response of a ramp-like pacing protocol. (**A**) Typical nonlinear parameter development during the last 10 beats before conduction block. (**B**, **C**) Evolution of Φ_e, $\dot{\Phi}_e$, and VL of CNF. First beat is drawn as solid lines, last beat before conduction block is shown in red.

For statistical analysis of beat-to-beat behavior $n = 15$ beats prior to conduction block S_b were analyzed. Taking into account multiple recording sites per pacing protocol a total number of $k = 105$ parameter development curves were gathered. Boxplots of parameter development shown in Figure 6.4a are drawn without outliers for better readability. Full graphs are shown in Appendix A.7.1. Major changes in beat-to-beat behavior occurred in E_{max}, LAT, Φ_{PP}, and $\dot{\Phi}_{min}$. Waveform symmetry a shifted slightly to more negative values (ending/colliding wavefronts). $\alpha_{E,LAT}$ and LCV remained almost constant and t_{depol} showed minor increase.

Pre-block clusters of all parameter development curves were statistically compared using a Mann-Whitney U-test. Results of comparison are shown in Figure 6.4b as significance matrix SM as described in Section 3.5.2. E_{max}, LAT, Φ_e, and $\dot{\Phi}_e$ were statistically significant different $9-11$ beats before conduction block occurs. a and t_{depol} showed significant differences $6-7$ beats before conduction block. $\alpha_{E,LAT}$ showed no statistically significant differences and LCV showed few intermittent significant differences between single beats.

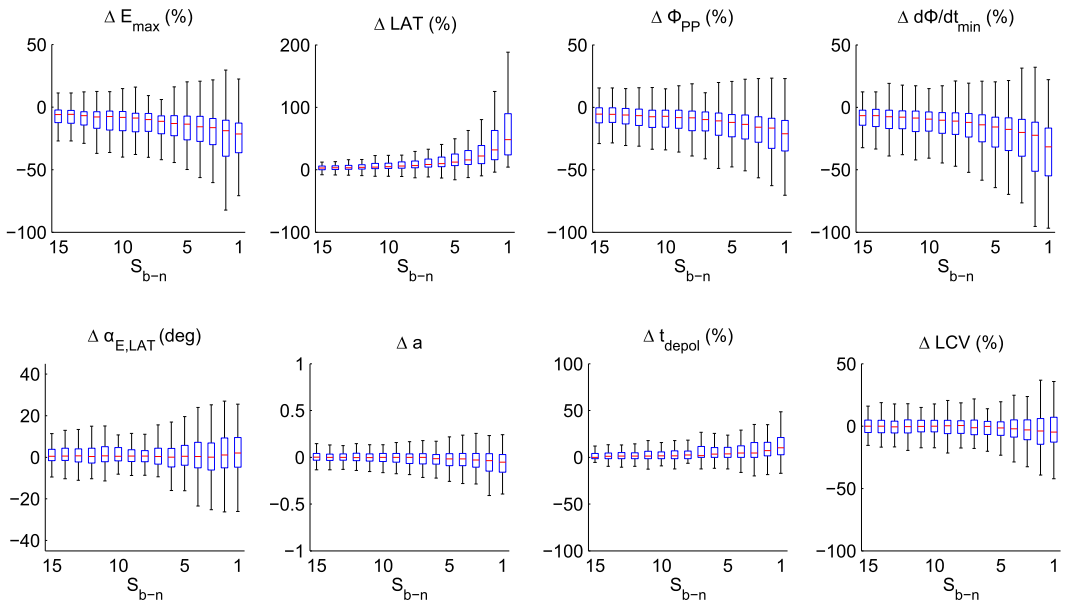

(a) Development of last 15 pre-block beats during ramp-like pacing. Parameters in top row showed distinct deviations from first beat of the pacing protocol. Parameters in bottom row showed only minor or no differences between consecutive beats.

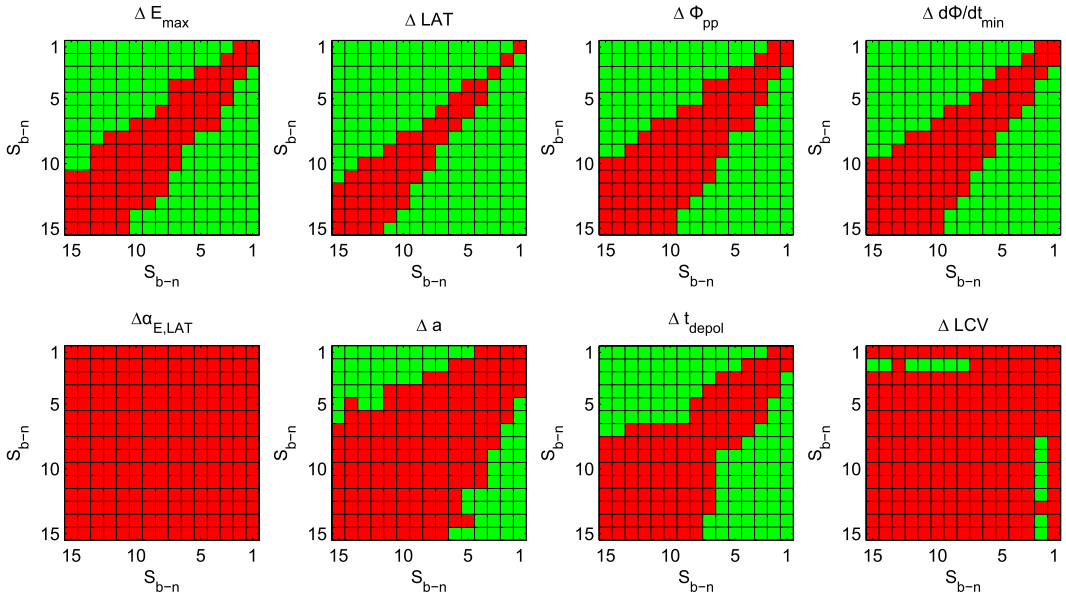

(b) Significance Matrix SM. Pre-block beats were compared using a Mann-Whitney U-test. Matrix element $a_{i,j}$ is the result of comparison of pre-block beat S_{b-i} with pre-block beat S_{b-j} from **(a)**. Red, no statistically significant difference; green, statistically significant difference.

Figure 6.4.: Pre-block behavior of ramp-like pacing protocols.

6.2.3. Pre-block Behavior of Stair-like Pacing Protocols

A total number of 36 stair-like pacing protocols were applied (cf. Table 6.2). 21 recordings resulted in alternans response. As for ramp-like pacing, parameter development showed weak PRD for the first stimuli of the pacing protocol followed by strong PRD in the final phase close to conduction block. In 8 cases an early phase with characteristic parameter deviations was present. Figure 6.5 illustrates the two cases.

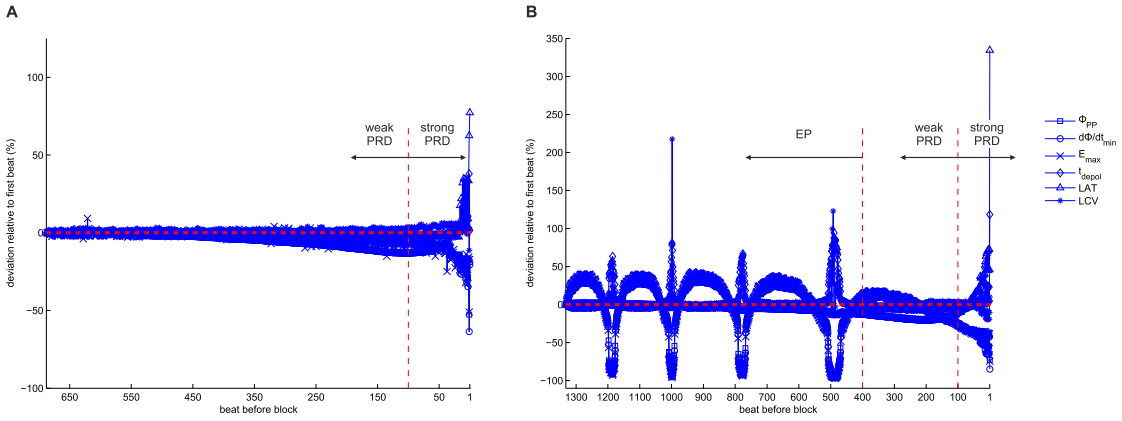

Figure 6.5.: Pacing rate dependency (PRD) for 2 stair-like pacing protocols. Both protocols showed alternans for the last beats before conduction block. (**A**) During EP only weak PRD was present. (**B**) EP with excursion from weak PRD was present for all parameters except LAT.

Typical alternans during the final phase of stair-like pacing protocols is shown in Figure 6.6. Slight alternans starts 60 beats before conduction block. At the transitions to higher pacing rates amplitude of alternans gradually increases. The last stimulus response is triggered after the transition from 65 ms to 60 ms PCL with complete distortion of the extracellular signal waveforms and large delay.
Details for parameter development during the last step of the pacing protocol with $PCL = 65\,\text{ms}$ is shown in the lower panels of Figure 6.6A. Parameters alternated between two distinct values for consecutive beats. Wavefrom symmetry a shifted from almost perfectly free-running signal waveform with $a \approx 0$ to $a \approx 0.15$ indicating partial ending/collision of the wavefront. $\alpha_{E,LAT}$ was least affected by alternans with beat-to-beat changes of $\approx 5°$. Amplitude of alternans, i.e parameter change in percent between consecutive beats, is shown in Figure 6.6D. For Φ_{PP}, $\dot{\Phi}_{min}$, E_{max}, t_{depol}, and LAT amplitude of alternans is at $\approx 20\,\%$ for the last step of the pacing protocol. Alternans amplitude for LCV is lower at $\approx 10\,\%$.

Statistical analysis was performed similarly to ramp-like pacing protocols as described

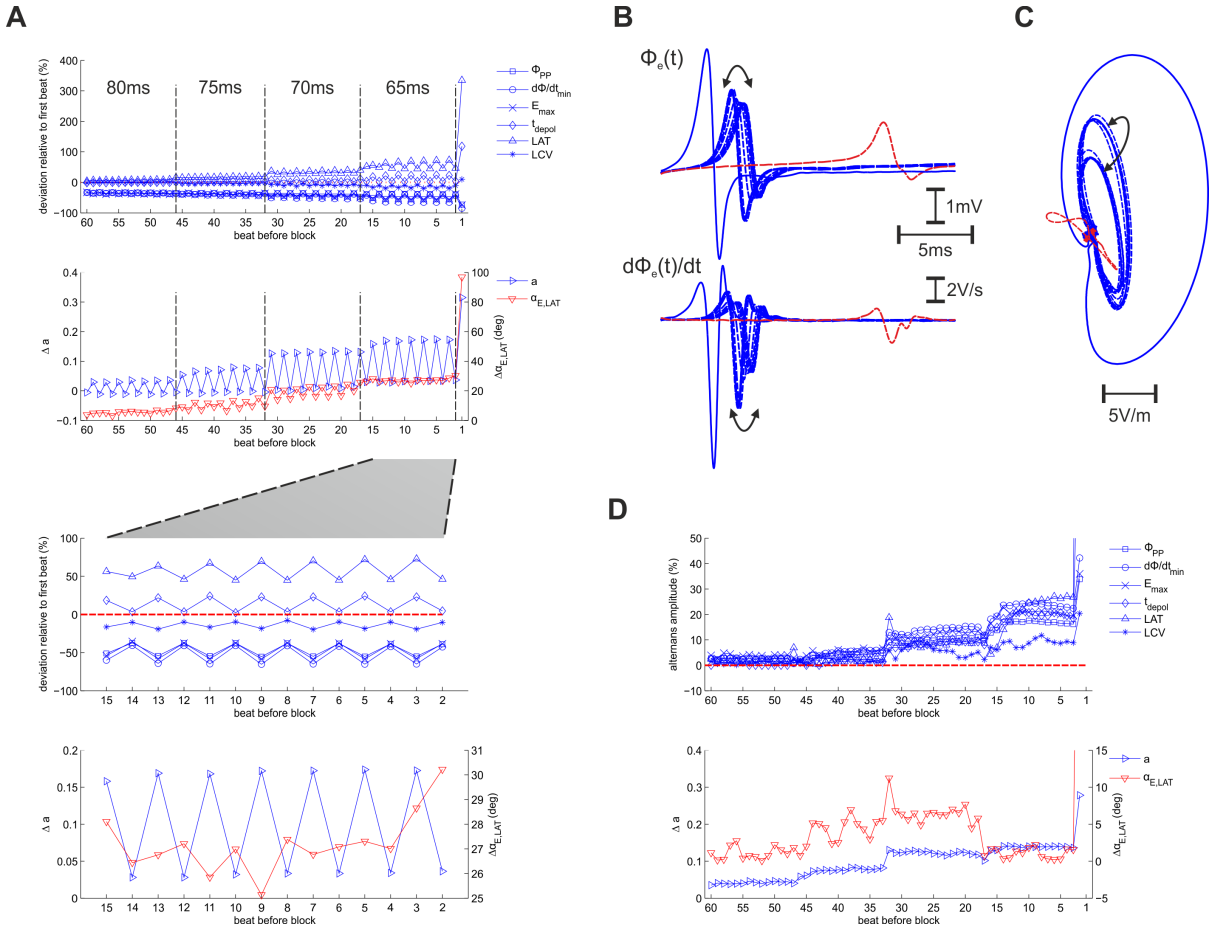

Figure 6.6.: Alternans response of a stair-like pacing protocol. (**A**) Typical alternating parameter development last 60 beats before conduction block. Lower graphs show last 15 beats before conduction block in detail. (**B**, **C**) Φ_e, $\dot{\Phi}_e$, and VL of CNF. Solid blue line is the first beat of the protocol, solid red line is the last beat before conduction block, and dashed lines are 15 beats before last beat. Note alternation of extracellular signal waveforms between two distinct morphologies. (**D**) Amplitude of alternans shown as beat-to-beat change in percent.

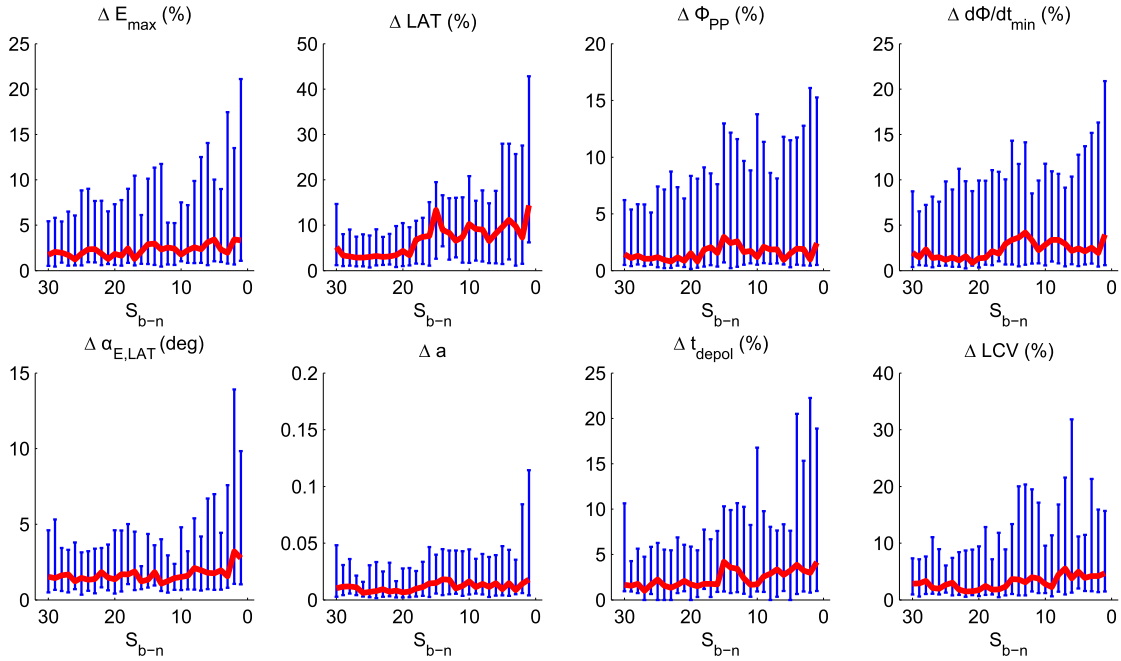

Figure 6.7.: Pre-block behavior of alternans amplitude. Last 30 beats of stair-like pacing protocols were evaluated. Red, development of amplitude median; blue, 25^{th} and 75^{th} percentiles.

above. Taking into account multiple recording sites per pacing protocol a total of 32 parameter development curves showing alternans were gathered. Pre-block beats were compared using a Mann-Whitney U-test. Due to the irregular nature of alternans in several recordings, i.e different direction of deflections (comparable with a phase shift), beat-to-beat changes showed no statistically significant differences between pre-block beats since changes are averaged out. Hence, amplitude of alternans was evaluated. Figure 6.7 shows amplitude of alternans as parameter change in percent between consecutive beats. Median of alternans amplitude slightly increases for all parameters by less than 10 %.

6.2.4. Pre-block Behavior of Premature Beat Protocols

A total number of 20 premature beat (S1S2) pacing protocols were applied. 18 of them resulted in nonlinear evolution of signal parameters for the premature (S2) beats similarly to ramp-like pacing protocols. Parameter development again showed strong PRD for the final phase of the pacing protocols. In 6 recordings parameter development showed periodic excursions from weak PRD during the EP of the pacing protocol. Figure 6.8 shows two typical parameter development curves.

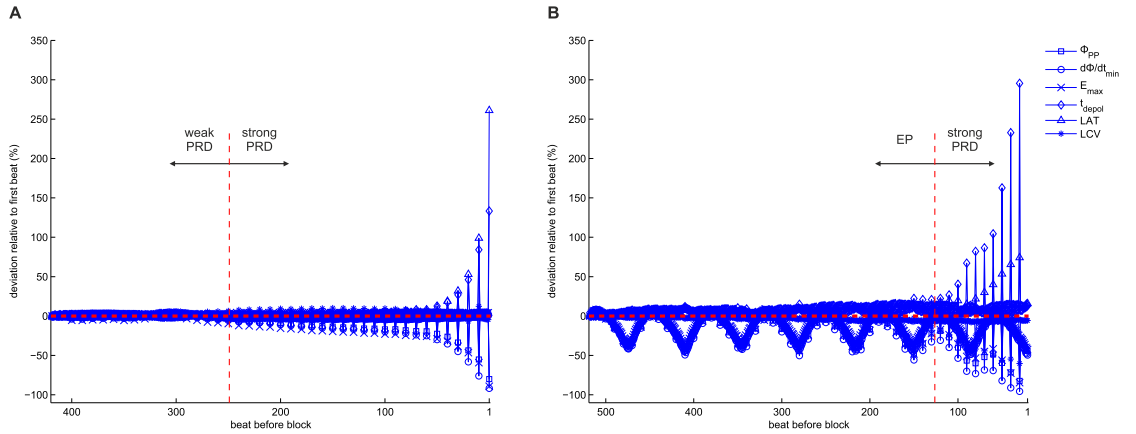

Figure 6.8.: Pacing rate dependency (PRD) for 2 premature beat (S1S2) pacing protocols. Both protocols showed nonlinear trends for the S2 beats. (**A**) During EP only weak PRD was present. (**B**) EP with periodic excursions from weak PRD was present for Φ_{PP}, $\dot{\Phi}_{min}$, and E_{max}.

Typical evolution of signal waveforms is depicted in Figure 6.9. S1 beats showed only little deviations, whereas consecutive S2 beats showed strong nonlinear behavior. Figure 6.9B illustrates beat-to-beat development of S2 pulses. The last 10 S2 beats showed increasing nonlinear PRD. Extracellular signal waveforms (Figure 6.9C) for the last 60 beats before conduction block revealed increasing latencies and changes of waveform. The last beat before conduction block (dashed red curve) indicates complete segmentation of the wavefront and arising fractionation. The VL of CNF in Figure 6.9D showed increasing deviation of direction for S2 beats.

For statistical analysis $n = 15$ S2 beats were selected. Taking into account multiple recording sites per pacing protocol a total number of $k = 35$ parameter development curves were gathered. Boxplots of evolution of parameters shown in Figure 6.10a are plotted without outliers for better readability. Original plots are found in Appendix A.7.3. Parameter development of S2 beats was very similar to ramp-like pacing.

S2 beat clusters were compared using a Mann-Whitney U-test. Results of comparison are shown in Figure 6.10b as significance matrix SM as described in 3.5.2. $\alpha_{E,LAT}$, a, and LCV showed no statistically significant differences between S2 beats. E_{max}, LAT, Φ_{PP}, and $\dot{\Phi}_{min}$ showed statistically significant differences 5 – 6 beats before conduction block arises.

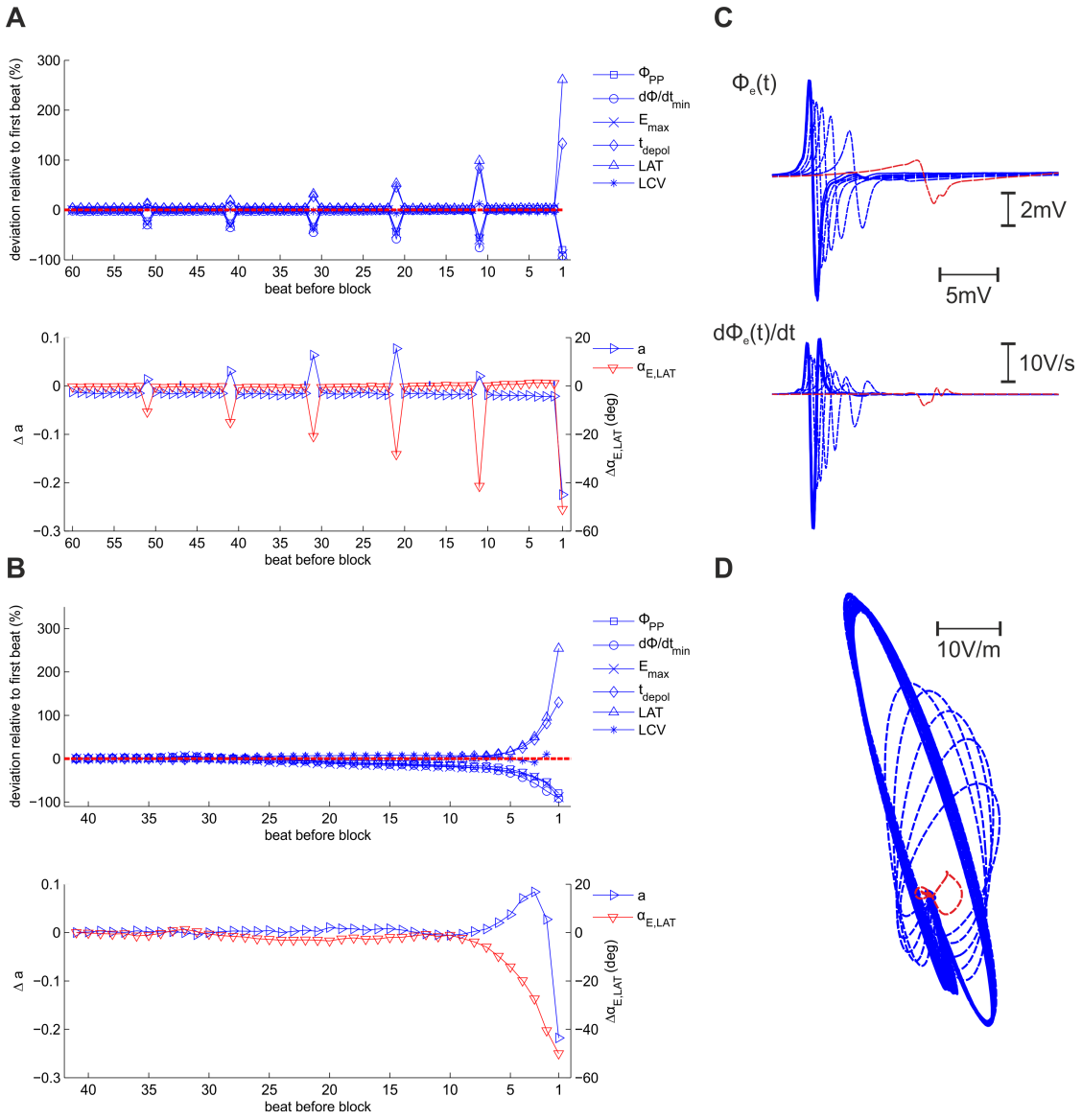

Figure 6.9.: Nonlinear response of a premature beat pacing protocol. (**A**) Typical parameter development of premature beat pacing protocol. (**B**) Development of S2-pulses. (**C**) Φ_e and $\dot{\Phi}_e$. First beat of protocol is drawn as solid lines, last beat before conduction block is shown in red. Dashed lines are last 60 beats before last beat. Note increasing latencies and waveform deviations of S2 beats. (**D**) VL of CNF. Direction of VL changes for consecutive S2 beats.

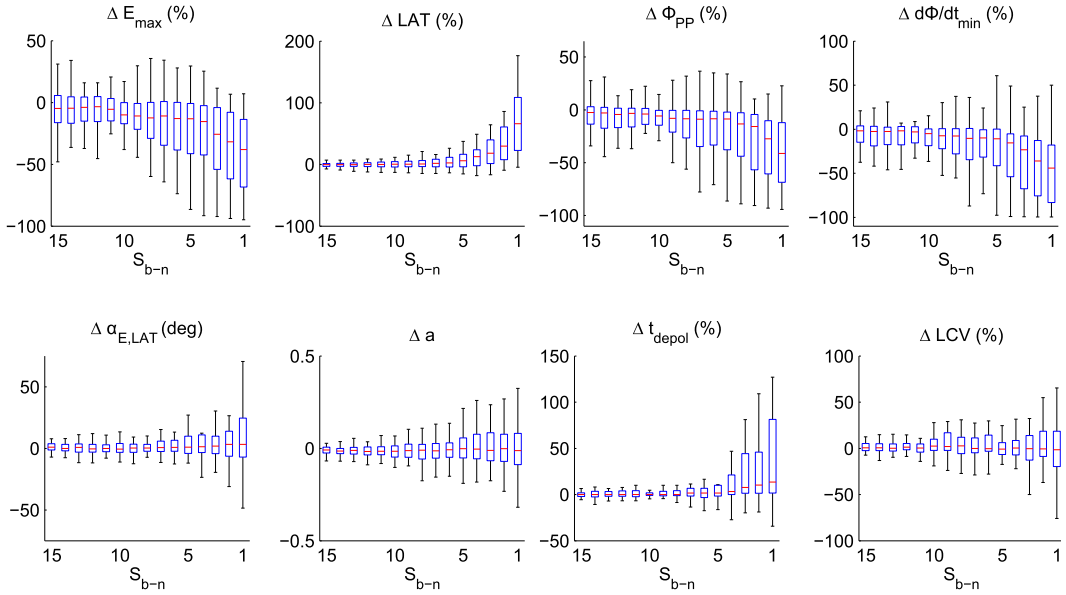

(a) Development of last 15 premature (S2) beats. Parameters in top row showed distinct deviations from first beat of the pacing protocol. Parameters in bottom row showed only minor or no differences between consecutive beats.

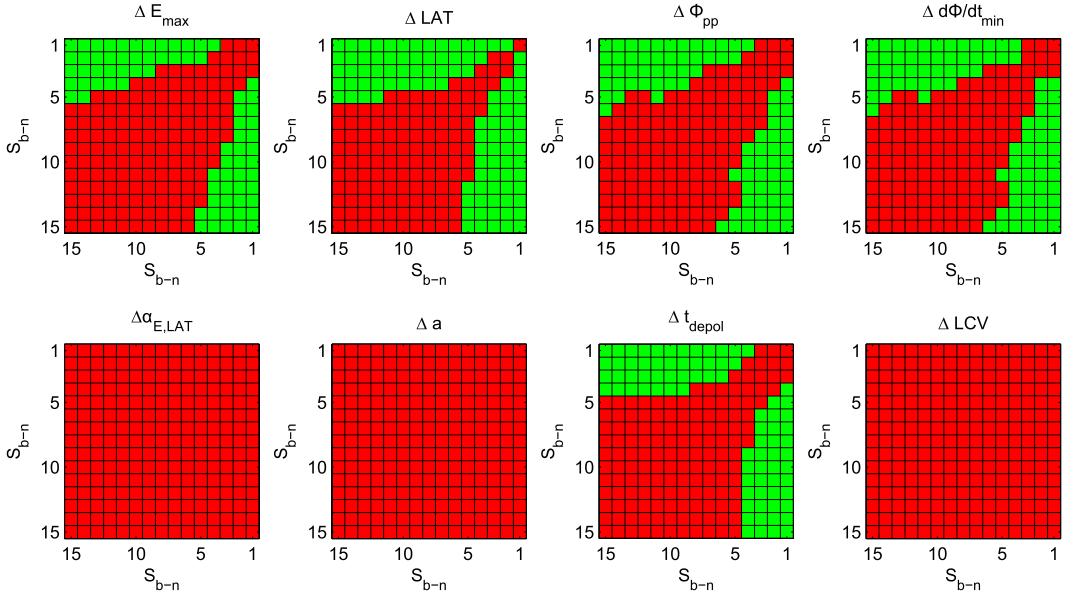

(b) Significance Matrix SM. S2 beats were compared using a Mann-Whitney U-test. Matrix element $a_{i,j}$ is the result of comparison of pre-block beat S_{b-i} with pre-block beat S_{b-j} from **(a)**. Red, no statistically significant difference; green, statistically significant difference.

Figure 6.10.: Pre-block behavior of premature beat pacing protocols.

6.3. Wavefront Segmentation

Shortly before conduction block (2 – 5 beats) the activation wavefront can become highly fractionated and segmented into individual micro-wavefronts. Figure 6.11 shows such a behavior for a ramp-like pacing protocol with retrograde pacing. The measurement site was in the proximal section of a PectM above a branching site where the PectM split into two muscle fibers (for retrograde pacing this represented a merging area of PectMs).

Extracellular potentials Φ_e and $\dot{\Phi}_e$ at the baseline PCL of 350 ms showed a fractionation index $FI = 2$ with a latency of 0.85 ms between the two activation wavefronts. Local conduction velocity LCV of the two wavefronts was 0.99 m s^{-1} and 0.78 m s^{-1}, respectively (LCV calculated by manual determination of LATs for each activation event and applying equation (3.3)). Taking the mean LCV of 0.89 m s^{-1} the two activation wavefronts were separated by 0.76 mm in space, which was approximately the diameter of the pectinate muscle. This indicates two activation wavefronts within the proximal section of the PectM. With decreasing PCL the activation wavefronts first moved closer together in time but at a PCL of 85 ms activation wavefronts dispersed and finally broke up into multiple activation wavefronts before conduction block arised.

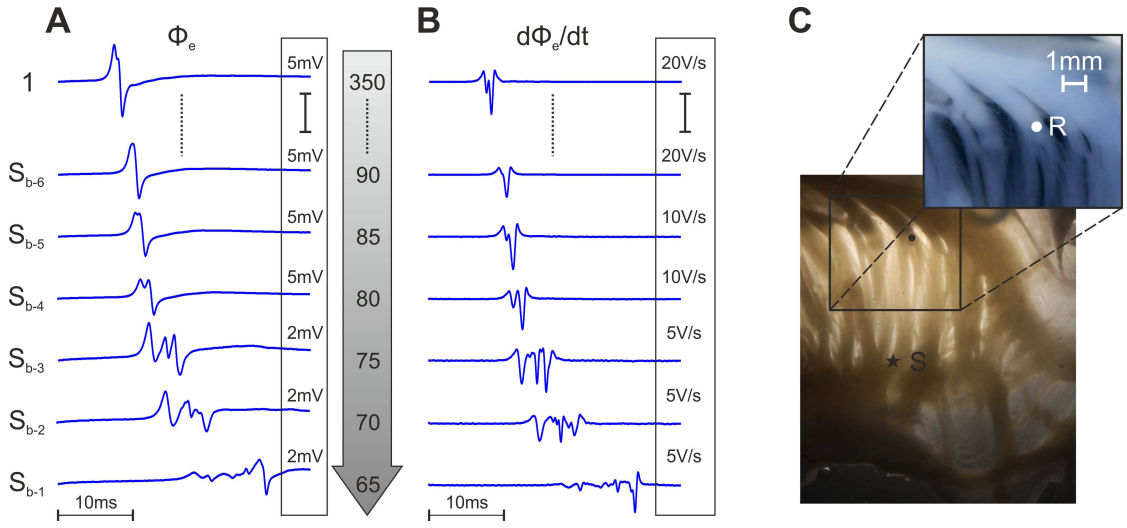

Figure 6.11.: Wavefront segmentation during final phase of ramp-like pacing. S_{b-n} is the n^{th} beat before conduction block S_b. (**A**, **B**) Extracellular signals Φ_e and $\dot{\Phi}_e$. Note different scales for amplitudes. (**C**) Tissue preparation (guinea pig, right atrium) with stimulus site S and recording site R.

6.4. Pacing Protocols at Sites of Interest

6.4.1. Branching of Pectinate Muscles

The PCL at which conduction block occurs varies in different structures and regions of the atrium. This is especially interesting at branching sites of pectinate muscles. At these sites one conduction pathway might be preferred at high pacing rate because of source-sink-mismatch. Figure 6.12 illustrates this behavior recorded in a guinea pig atrial preparation: A stair-like pacing protocol was applied at stimulus site S and extracellular potentials Φ_e were recorded at sites P1, P2, and P3. P1 was located on the terminal crest, P2 and P3 were located at 2 distinct muscle fibers which branched from one PectM.
At the transition from 75 ms to 70 ms PCL conduction failed at P3 (right branch of PectM) whereas conduction was successful at the other recording sites. Conduction failed at P2 when PCL was decreased from 45 ms to 40 ms. Impulse propagation was maintained longest at recording site P1 where conduction block occurred at 20 ms. Figure 6.12B shows the applied pacing stimuli at S in the bottom row. Pacing responses at the recording sites are drawn above.

A ramp-like pacing protocol applied at the same stimulus site S did not show the behavior described above (Figure 6.12C). In this case conduction block occurred simultaneously at all recording sites.

It has to be noted that the conduction time between stimulus site and recording sites P2 and P3 is quite large (≈ 35 ms). If PCL is in the same range or below this conduction time correlation between stimulus and activation response is difficult. Nevertheless, Figure 6.12B and C are valid until first occurrence of conduction block.

6.4.2. Initiation of Tachyarrhythmia

In 2 rabbit atrial tissue preparations tachyarrhythmias were initiated by stair-like pacing protocols whereas ramp-like pacing protocols did not. Figure 6.13A shows a rabbit right atrium with stimulus site S (retrograde) and recording sites P1, P2, and P3 in the PectM network. Application of a stair-like pacing protocol caused persistent tachyarrhythmia with a cycle length of 100 ms. Decreasing PCL showed first deviations in stimulus response at 150 – 130 ms. Pacing at a PCL of 100 ms initiated self-sustaining

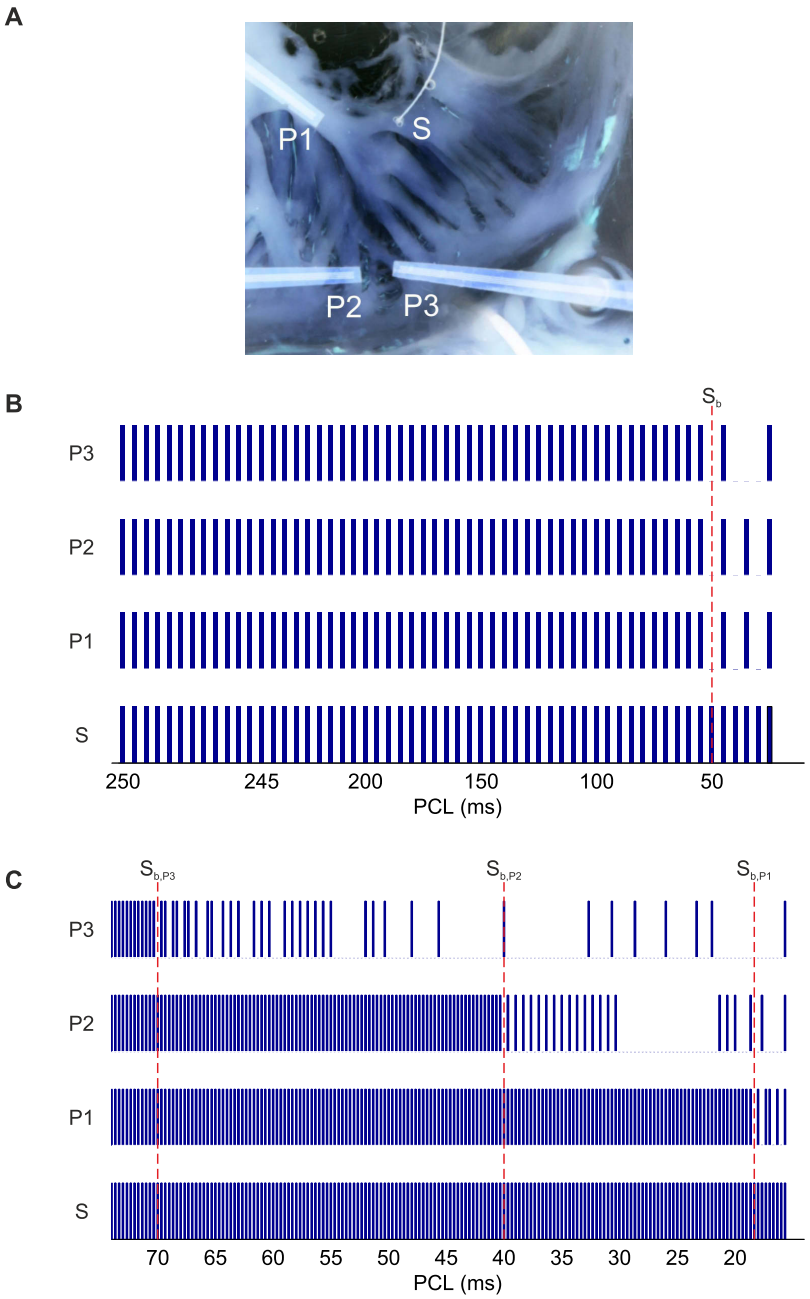

Figure 6.12.: Conduction block at branching site of PectM. (**A**) Guinea pig atrium. S, stimulus site; P1, P2, and P3, recording sites. (**B**) Application of ramp-like pacing evoked simultaneous conduction block S_b at all recording sites. (**C**) Stair-like pacing resulted in different occurrence of conduction block $S_{b,P1...3}$ at all 3 recording sites. Bars in graphs represent the pacing stimuli (S) and the response at the recording sites.

activation of the tissue which is no more affected by the pacing impulse train delivered to the tissue, i.e. cycle length remained constant at 100 ms although pacing was continued as shown in Figure 6.13B. Extracellular parameters showed alternans during the tachyarrhytmia (Figure 6.13C).

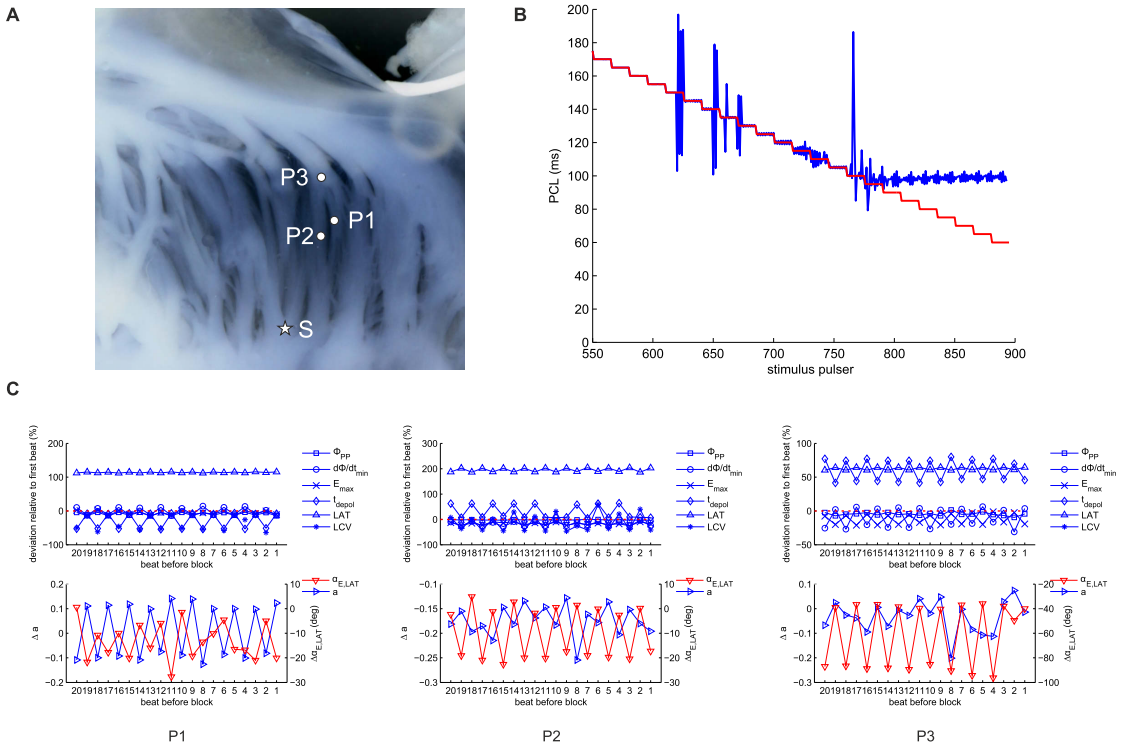

Figure 6.13.: A stair-like pacing protocol initiated self-sustaining tachyarrhythmia in a rabbit atrium. (**A**) Location of recording sites $P_{1...3}$ and pacing site S. (**B**) Development of stimulus response. Red curve shows stair-like pacing impulses applied to the tissue, blue curve shows the measured cycle length between activation events. (**C**) Signal parameters during tachyarrhythmia showed alternans.

6.5. Shifting of the Primary Pacemaker Location

The activation sequence of the atrium strongly depends on where first activation is initiated. It has been shown by Fedorov, Schuessler, et al. (2009) that there is only a discrete number of exit pathways from the SAN into the surrounding myocardium. To elucidate this point overdrive pacing with constant PCL was applied at varying stimulus sites. Figure 6.14 illustrates the effect of altered primary pacemaker location on excitation patterns. A rabbit atrial tissue preparation was paced at two distinct

stimulus sites S_A and S_B in the area where the SAN is assumed to be located. The two stimulus sites triggered different characteristics of extracellular waveforms at three recording sites P1, P2, and P3. If compared to signal waveforms recorded at sinus rhythm, excitation spread induced by pacing at site S_A differed, whereas excitation spread induced by pacing at site S_B was almost identical to sinus rhythm. Therefore it can be assumed that the primary pacemaker is located close to stimulus site S_B.

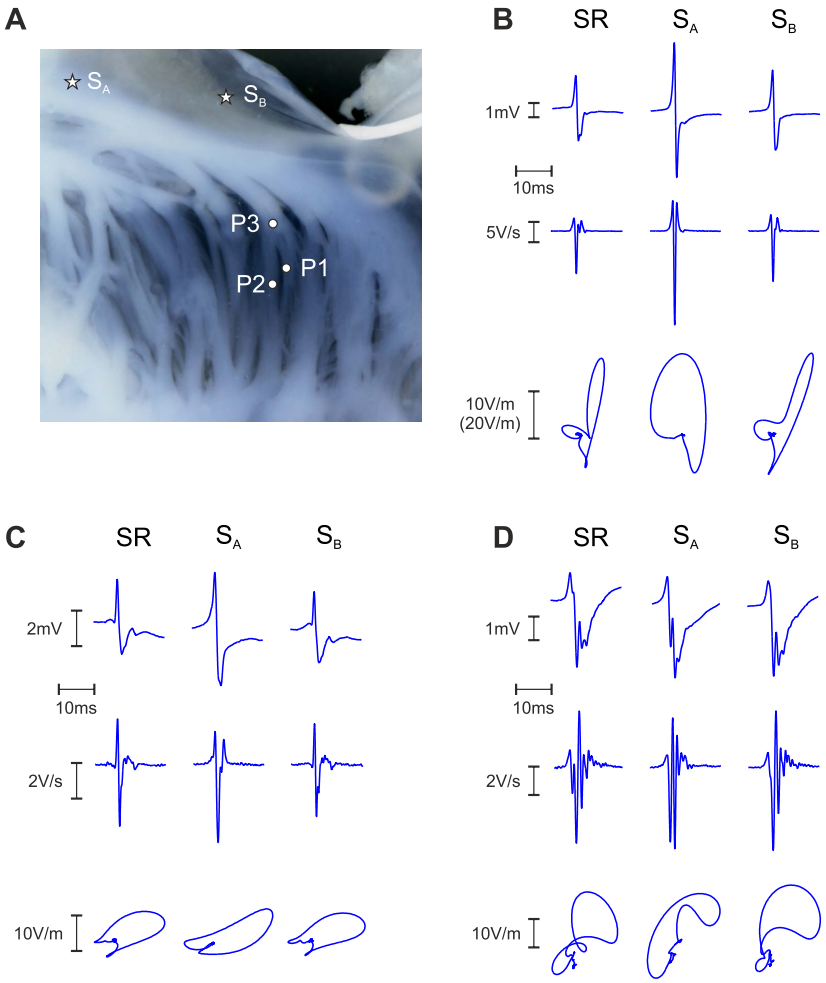

Figure 6.14.: Shift of primary pacemaker by electrical pacing. (**A**) Rabbit atrial tissue preparation. S_A, S_B, pacing sites; P1-P3, recording sites. (**B-D**) Extracellular signals at P1-P3. Φ_e top, $\dot{\Phi}_e$ middle, VL bottom. Column SR shows signals during sinus rhythm. Pacing at S_A changed local potential waveforms whereas pacing at S_B was identical to SR.

Part III.

Discussion and Outlook

7. Discussion

7.1. Anatomy

There was a considerable variability in size, diameter, and length of structures within the CTI. Also branching topology as well as number of PectM segments showed a wide range. This is due to the facts that (i) rabbits were not selected from a small range of weight and age and (ii) morphology is inherently variable between different hearts.

Experiments in this thesis were carried out with tissue preparations from small animals. The question arises if these results are applicable to human atria. Disregarding the size of the tissue preparations, anatomical structures found in human atria are comparable to rabbit and guinea pig right atria: The right atria comprise the appendage, the venous part, the vestibule, and the interatrial septum (Anderson and Cook, 2007; Ho et al., 2002). The prominent terminal crest with emerging pectinate muscles and the cavotricuspid isthmus also shows similar branching and merging topologies (Sánchez-Quintana, Anderson, et al., 2002).

The size of the cavotricuspid isthmus is clearly larger in human atria and was found to be 30 ± 3 mm (ILI) and 24 ± 4 mm (PSI) as shown by Cabrera and Sánchez-Quintana (2013). Compared to a mean human body weight of 70.8 kg (Walpole et al., 2012) rabbits in this thesis weighed less by a factor of ≈ 17. Assuming that lengths are related to volume by the 3^{rd} root, a length ratio of ≈ 2.6 is expected. This is in accordance with the size of the CTI found in rabbits: ILI is shorter by a factor of 2.03 and PSI is shorter by a factor 3.29.

Inducibility of reentry, i.e. self-sustaining circular wavefronts, is hence generally easier in human atria since available pathways are longer. Nevertheless, reentry is also possible in small animals if refractory period is short enough and conduction velocity is low

(Nattel et al., 2008). It has been shown by Wu et al. (1998) that ridge-like structures in the PectM network of dogs with lengths of 10.5 ± 0.9 mm serve as anchoring sites for reentrant wavefronts. Although the authors used Acetylcholine (ACh) for initiation of reentry the same would be possible in the preparations used in this work if functional heterogeneities arise since PectM structures are comparable in size (8.81 ± 2.27 mm) and therefore reentry would be inducible by premature pacing techniques.

Topology of the pectinate muscle network showed large inter-individual diversity. In average the number of PectMs doubled in the central sections or equivalently one proximal segment branched into two central segments in average. Taking the mean diameter of PectM sections as a measure for current sources, i.e. the number of myocytes involved in excitation spread, there is a source-sink mismatch: 0.85 mm of the proximal segments compared to 2×0.68 mm of the emerging central segments. This suggest potential sites for conduction block at elevated heart rates and the accompanied functional divergence.

7.2. Autorhythm

The observed episodes of arrhythmic activation during the accommodation phase in the tissue bath and the corresponding signal recordings in Section 5.3 suggest delayed or slow remote pathways entering the PectMs retrograde. It has to be noted that no self-sustaining reentry activation occurred thus retrograde activation did not enter the CT. This might be due to unidirectional conduction block related to complex microstructure at the transitional zone or elongated ERP in the CT with $ERP > 160$ ms.

Representative signal waveforms shown in Section 5.5.1 reflect underlying microstructure and excitation spread properties. Uniform excitation spread with smooth and symmetrical biphasic deflections in Φ_e are typical for a free-running activation wavefront in well-coupled tissue mainly found in the central segments of PectM. In case of fibrotic inlays oriented parallel to myocytes extracellular potentials with $FI = 2$ are observed if activation on either side of the fibrotic inlay is time-delayed. Extracellular potentials with $FI = 2$ also may arise if remote activation events are present, i.e. activation of neighboring or crossing muscle fibers. Discrimination between local and distant events is challenging and a complex inverse problem (Spach and Dolber, 1986; Wiener, 2012). At the transition from CT to PectM and from PectM to VB fiber orientation has to change and hence excitation wavefronts are forced into intricate pathways leading to

highly fractionated extracellular potentials. Interpretation of fractionated electrograms, however, is difficult and often ambiguous since various effects lead to fractionation as shown by de Bakker and Wittkampf (2010). Of particular interest is the direction of local excitation spread estimated from CNF. Therefore, a separation of superimposed electrograms would be beneficial in distinguishing for example parallel spreading but time-delayed activation wavefronts from antiparallel or colliding wavefronts. If activation events are separated sufficiently in time this can be done easily by windowing in the time domain. Otherwise sophisticated signal analysis algorithms are necessary. An algorithm for decomposition of fractionated potentials with time delays of only 0.6 ms was introduced recently by Wiener et al. (2012).

Analysis of signal recordings from different regions within the CTI showed characteristic distribution of extracellular signal parameters:
Peak-to-peak amplitude Φ_{PP} was significantly larger in PectM than in the CT or VB suggesting uniform microscopic structure with well coupled and simultaneously activated myocytes, little changes in fiber orientation, and little amount of fibrosis (cf. Figure 5.6). Distribution of FI supports this: The largest portion of uniform, free-running activation was found in PectM. Altogether $\approx 75\,\%$ of signals in PectM had a FI of $1-2$. The same applies for the minimum of the first temporal derivative $\dot{\Phi}_{min}$ reflecting fast longitudinal propagation of activation in PectM with little dispersion of ionic currents.

LCV was statistically significant higher in CT than in PectM and VB indicating either well coupled myocytes or reduced surface-to-volume ratio (larger fiber diameter or reduced packing density of fibers). In all regions within CTI very high values of LCV ($2.01-2.93\,\mathrm{m\,s^{-1}}$) were found. Such high values are likely to arise if excitation spread is not parallel to the tissue surface, thus, leading to erroneous estimation of LCV. The lowest value of LCV in this work was measured with $0.2\,\mathrm{m\,s^{-1}}$ in the CT. A potential mechanism for this slow conduction is the branching topology between CT and PectM as shown by Kucera et al. (1998) in cell cultures of complex geometries. Also reduced electrical coupling between cells or reduced excitability may be responsible for local slow conduction (Rohr, Kucera, et al., 1998). In PectM the lowest LCV was $0.3\,\mathrm{m\,s^{-1}}$. Taking a typical APD of 50 ms (Aslanidi et al., 2009) a critical path length of 15 mm for reentry activation can be calculated. Therefore, two neighboring PectMs in the rabbit atrium could theoretically sustain a reentry wavefront.

Duration of depolarization t_{depol} and therefore the spatial extent of the activation wavefront was significantly larger in VB. Since conduction velocity LCV in VB is the same

as in PectM this arises probably from different ion kinetics of myocytes in this region. Also determination of t_{depol} from ending potentials which are expected to be more frequent in the VB is difficult and might lead to erroneous estimation of t_{depol}.

Fractionation in CT was moderate with FI between $1-5$. At the transition from CT to PectM fiber orientation has to change and therefore fractionation of Φ_e arises. In VB the largest amount of highly fractionated electrograms with $FI \geq 10$ was found. This suggests either a large number of independent pathways, disorder in microstructure with sudden changes in fiber direction associated with zig-zag spread of activation, or crossing fibers (de Bakker and Wittkampf, 2010).

Waveform symmetry a showed the highest amount of starting potentials in CT with 25 % of the recordings. The largest amount of ending/colliding potentials was found in VB again in 25 % of the recordings.

Parameter distribution in sections of PectMs was almost identical for proximal, central, and distal segments. Only waveform symmetry a showed a larger portion of starting potentials in the proximal sections of PectMs as expected.

Pectinate muscles within the CTI are well defined macroscopic cable-like structures with 8.81 ± 2.27 mm length and 0.68 ± 0.32 mm diameter in the central section (cf. Chapter 4). As mentioned above, PectMs are more complex in structure at a microscopic scale, i.e. connective tissue inlays are present within the muscle fiber. These connective tissue inlays divide the macroscopic uniform structure into separated microscopic conduction pathways. Connective tissue can exhibit different spatial characteristics like compact, diffuse, interstitial, and patchy (de Jong et al., 2011) each accompanied by characteristic influence on wavefront propagation and therefore extracellular electrograms (Jacquemet and Henriquez, 2009). Assuming that connective tissue inlays in the central section of a PectM are of interstitial type and oriented parallel to myocardial fibers, these inlays have only minor effects on extracellular electrograms if an excitation wavefront spreads in longitudinal direction. However, at merging areas of 2 or more individual PectMs wavefront collision occurs revealing complex microscopic structures and resulting in fractionated electrograms. Figure 5.14 illustrates this case with a small pectinate muscle merging with a larger one. Signal recordings along the left border of the larger PM showed uniform non-fractionated signals. Along the medial line extracellular potentials showed fractionation beneath the merging area demonstrating the influence of anisotropic microstructure in case of oblique spread of activation.

An activation wavefront in the CTI does not start simultaneously in all neighboring PectMs of the CTI. The sequence in which the individual PectMs are activated depends on the conduction of depolarization in the CT and the transitional area between CT and PectM. Activation sequence within the CT depends on the location of the primary sinoatrial pacemaker, and on the site where primary activation enters the CT (discrete exit pathways of the SAN as shown by Fedorov, Schuessler, et al., 2009). Conduction in the transitional area to PectMs depends on the microstructure and can be expected to be complex.

Retrograde conduction in individual PectM during sinus rhythm is shown in Section 5.8. Reasons for this might be (i) conduction block between CT and PectM or (ii) bypassing epicardial conduction pathways. The retrograde conduction observed in 3 atria occurred without formation of reentry at stable sinus rhythm but in case of functional heterogeneities this could constitute a potential substrate for reentry.

Intracellular action potential recordings shown in Section 5.9 are in accordance to literature, i.e. there is shift of APD along CT (Boyett et al., 1999; Li-jun et al., 2012).

7.3. Pacing

In the applied pacing protocols the absolute values of ERP differed slightly between rabbit and guinea pig tissue. Analysis was performed "species-independent" since only parameter development relative to control conditions was of interest. Nevertheless, analysis was also performed for species separately (see Appendix A.6) and parameter development curves showed the same characteristics as expected.

Pacing rate dependency (PRD) of extracellular parameters showed deviations in the early phase for some experiments. This might be due to incomplete achievement of steady state conditions prior to the pacing protocol. Especially in stair-like and premature beat pacing protocols (cf. Section 6.2.3 and 6.2.4) periodic excursions of signal parameters occurred. Interpretation of this excursions is difficult since periodicity is not correlated to PCL and differs between recordings. Therefore, it is possible that these excursion are measurement artifacts due to sensor movement and/or contraction movement of the tissue preparations. Nevertheless, in the final phase of pacing protocols PRD is clearly stronger correlated with PCL in terms of beat-to-beat changes than during the early phase.

Parameter development curves shown in this work theoretically enable the prediction of conduction block from extracellular parameters. During ramp-like pacing protocols the most prominent changes were present in LAT. This is deceptive since there are only small changes in LCV and macroscopic conduction velocity (estimated from latencies between electrograms of multiple CNF sensors, data not shown) despite large changes in LAT which suggests that increased LAT is rather caused by delayed initiation of excitation spread at the stimulus site. The most promising parameters for prediction of conduction block are Φ_e, $\dot{\Phi}_{min}$, and E_{max} for which significant changes arise 10 beats before conduction block, or equivalently 50 ms in PCL for a decremental interval of 5 ms.
In stair-like pacing protocols deflections of extracellular parameters were smaller than for ramp-like pacing protocols. Nevertheless, the parameter development is very characteristic and accompanied by alternans. Hence the amplitude of alternans could be a potential candidate for prediction of conduction block although mean amplitude change was less than 10 %.
Parameter development of S2-pulses in premature beat pacing protocols was very similar to ramp-like protocols. Therefore, again Φ_e, $\dot{\Phi}_{min}$, and E_{max} are the most promising precursors for conduction block but significant changes occur later, i.e 5 beats before conduction block arises.
It has to be noted that variance of all parameters was large. Microstructural complexity is heterogeneous throughout the CTI and therefore the anisotropic nature of excitation spread, which becomes more prominent at high pacing frequencies and is responsible for parameter development, is different leading to varying amplitudes of parameter evolution.
Actual prediction of conduction block would require sophisticated algorithms and models like time-series analysis or neuronal networks.

Microstructural influence on excitation spread becomes more prominent at high pacing rates as mentioned above. This can lead to segmentation of otherwise uniform conduction into multiple micro-wavefronts as shown in Section 6.3.

Beat-to-beat behavior at branching sites of PectM is of particular interest since these sites represent points of critical source-sink mismatch and might lead to local disturbance of conduction at high pacing rates. Berenfeld et al. (2002) showed that unidirectional block occurs at branching sites of the CT and the PectM network at higher pacing frequencies. Signal recordings at a branching site in Section 6.4.1 showed frequency-dependent preference of pathways in individual single muscle fibers. This introduces a

large gradient in refractoriness and thus might enable the incidence of reentry arrhythmias.
Mechanisms for preferential conduction in one excitation pathway may again be found in microstructure since fiber orientation can be expected to change. Depending on the excitation spread above the branching site one PectM might be activated by transverse conduction which has been shown to have a higher safety factor of propagation than longitudinal propagation (Spach, Miller, et al., 1982).
The different block behavior of ramp-like and stair-like pacing protocols suggests that pacing history and cardiac memory (Kalb et al., 2004) plays a vital role in impulse propagation. A rapid increase in PCL during ramp-like pacing protocols apparently results in more uniform distributed adaption dynamics.

Pacing dynamics and cardiac memory are obviously also important in the initiation of tachyarrhythmias as shown in Section 6.4.2. Ramp-like pacing protocols did not lead to tachyarrhythmias whereas stair-like protocols did. This again indicates that stair-like protocols result in more heterogeneous restitution, creating substrates for the initiation of tachyarrhythmias (Clayton and Taggart, 2005). It has also been shown that alternans, as introduced by stair-like pacing protocols, can result in arrhythmias (Pastore et al., 2006; Weiss, Karma, et al., 2006; Wilson and Rosenbaum, 2007).

Activation sequence of CTI is determined by (i) the site of primary pacemaker activation, (ii) the exit pathways from SAN into CT, (iii) the conduction along CT, and (iv) the transition from CT into the PectM network. It has been shown by Fedorov, Hucker, et al. (2006) and Lang et al. (2011) that location of the primary pacemaker site shifts at elevated heart rates. This was mimicked in this work by varying the stimulus site along CT as shown in Section 6.5 and resulted in variations of local excitation spread and extracellular potentials. Thus characterization of potential arrhythmogenic substrates has to take into account this alterations of activation patterns with increased heart rate.

7.4. Action Potential Restitution

APD is a function of the preceding diastolic interval (DI), i.e. the time between repolarization of a cell and the subsequent action potential. Plotting APD against the preceding DI yields characteristic curves referred to as restitution curves. Classically conduction block and incidence of arrhythmias was associated with APD restitution

curves when the slope of the curve exceeds unity (Weiss, Garfinkel, et al., 1999). This concept had to be reviewed after recognizing that arrhythmias also may arise despite steep restitution slopes as shown for example by Banville and Gray (2002). This was attributed by the principle of cardiac memory which states that APD restitution is a function of pacing history and not solely of the preceding DI (Watanabe and Koller, 2002). Sophisticated pacing protocols have been developed to characterize effects of cardiac memory and pacing rate (Kalb et al., 2004). Creating restitution curves, however, is challenging since intracellular action potential recordings or monophasic action potential (MAP) recordings (Franz, 1999) have to be obtained and pacing protocols are long-lasting.

Although attempted, comprehensive studies of APD restitution were not possible in this work since achievement of stable microelectrode impalement for the duration of pacing protocols was not feasible. The contraction movement, especially in the PectM network, is large in amplitude and therefore the tip of the microelectrode was frequently forced out of myocytes. The number of signal recordings therefore was too small to generate reliable data and this aspect was not included in this work.

Nevertheless, cardiac memory and the dependency on pacing history is also evident in extracellular parameters obtained from pacing protocols with different timing dynamics as shown in this work.

8. Conclusion and Outlook

In this work three major topics concerning excitation spread and activation patterns in the CTI have been covered: (i) detailed description of the anatomical structure and the resulting macroscopic conduction pathways, (ii) electrograms and conduction during sinus rhythm, and (iii) development of electrograms and excitation spread with increasing heart rate.

Results from comprehensive morphometry as performed in this work for rabbit atria can serve as basis for rule-based computer models to generate artificial atrial structures with appropriate branching and merging topologies.

Electrical characterization of different regions within the right atrium during sinus rhythm facilitates the development of electro-anatomical maps. These maps could be used to verify results from computer simulation studies and to determine subregions of increased structural complexity.

From a clinical point of view the development of extracellular parameters before conduction block arises is of particular interest. The obtained characteristic parameter development curves open the possibility to predict conduction block and to identify potential arrhythmogenic substrates without the need to induce arrhythmias in patients. The provocation of self-sustaining arrhythmias could be avoided since conversion to normal sinus rhythm is associated with high energy stimulus pulses which could further damage the tissue (Epstein et al., 1998; Wang, Efimov, et al., 2012). Application of appropriate pacing protocols for "mild pacing" in terms of arrhythmia free characterization of substrates thus becomes a possible feature for improved catheter ablation procedures.

Atrial flutter and fibrillation are related to aging and the associated changes in cardiac microstructure, i.e. an increasing amount of cardiac fibrosis. Not only the mere

amount but also spatial distribution of fibrosis is vitally important for initiating and maintaining tachyarrhythmias (Tanaka et al., 2007). As shown in this work microstructure becomes apparent in extracellular potentials by application of electrical pacing. Therefore, adequate pacing techniques along with spatial highly resolving CNF recordings could promote detection and classification of cardiac fibrosis as shown in recent computer simulations (Campos, Wiener, et al., 2013) and electrophysiological experiments (Arnold, Wiener, Schwarz, et al., 2012).

Bibliography

Adam et al. (2003). *Physikalische Chemie und Biophysik*. 4. Auflage. Springer-Verlag Berlin Heidelberg New York (cit. on p. 5).

Anderson, Robert H. and Andrew C. Cook (Nov. 2007). "The structure and components of the atrial chambers." eng. In: *Europace* 9 Suppl 6, pp. vi3–vi9 (cit. on p. 71).

Arnold, R. (2009a). *DataViewer - Erweiterung des Messsystem HARMS*. Tech. rep. Institute of Biophysics, Medical University of Graz (cit. on p. 31).

Arnold, R. (2009b). "Measurement System for the Study of Cardiac Excitation Patterns in Rapidly Paced Animal Hearts." MA thesis. Graz University of Technology (cit. on pp. 24, 26).

Arnold, R., T. Wiener, and E. Hofer (2010). "System zur Stimulation und Datenauswertung zur Untersuchung der Erregungsausbreitung in Herzpräparaten unter erschwerten Leitungsbedingungen." In: *CD-ROM, Walter de Gruyter: Biomedizinische Technik / Biomedical Engineering - Proceedings2010; Supplement 2010: BMT 2010; OCT 5-8, 2010; Rostock-Warnemünde, Germany* (cit. on p. 31).

Arnold, R., T. Wiener, D. Sanchez-Quintana, et al. (2011). "Topology and conduction in the inferior right atrial isthmus measured in rabbit hearts." eng. In: *Conf Proc IEEE Eng Med Biol Soc* 2011, pp. 247–250 (cit. on pp. 34, 49).

Arnold, R., T. Wiener, M. Schwarz, et al. (Aug. 2012). "Circumferential Pacing Reveals Microstructure of Cardiac Tissue Preparations from Small Animals - An Approach to Classify Microfibrosis." eng. In: *Biomed Tech (Berl)* (cit. on p. 80).

Aslanidi, Oleg V. et al. (Feb. 2009). "Mechanisms of transition from normal to reentrant electrical activity in a model of rabbit atrial tissue: interaction of tissue heterogeneity and anisotropy." eng. In: *Biophys J* 96.3, pp. 798–817 (cit. on p. 73).

Bähring, Robert and Manuel Covarrubias (Feb. 2011). "Mechanisms of closed-state inactivation in voltage-gated ion channels." eng. In: *J Physiol* 589.Pt 3, pp. 461–479 (cit. on p. 7).

Banville, Isabelle and Richard A. Gray (Nov. 2002). "Effect of action potential duration and conduction velocity restitution and their spatial dispersion on alternans and the stability of arrhythmias." eng. In: *J Cardiovasc Electrophysiol* 13.11, pp. 1141–1149 (cit. on p. 78).

Berenfeld, Omer et al. (June 2002). "Frequency-dependent breakdown of wave propagation into fibrillatory conduction across the pectinate muscle network in the isolated sheep right atrium." eng. In: *Circ Res* 90.11, pp. 1173–1180 (cit. on p. 76).

Bogdanov, Konstantin Y. et al. (Oct. 2006). "Membrane potential fluctuations resulting from submembrane Ca2+ releases in rabbit sinoatrial nodal cells impart an exponential phase to the late diastolic depolarization that controls their chronotropic state." eng. In: *Circ Res* 99.9, pp. 979–987 (cit. on p. 13).

Boyett, M. R. et al. (Feb. 1999). "Downward gradient in action potential duration along conduction path in and around the sinoatrial node." eng. In: *Am J Physiol* 276.2 Pt 2, H686–H698 (cit. on p. 75).

Bucchi, Annalisa et al. (July 2007). "Modulation of rate by autonomic agonists in SAN cells involves changes in diastolic depolarization and the pacemaker current." eng. In: *J Mol Cell Cardiol* 43.1, pp. 39–48 (cit. on p. 13).

Cabrera, José Angel and Damián Sánchez-Quintana (Mar. 2013). "Cardiac anatomy: what the electrophysiologist needs to know." eng. In: *Heart* 99.6, pp. 417–431 (cit. on p. 71).

Cabrera, José Angel, Damian Sánchez-Quintana, et al. (Apr. 2005). "The inferior right atrial isthmus: further architectural insights for current and coming ablation technologies." eng. In: *J Cardiovasc Electrophysiol* 16.4, pp. 402–408 (cit. on p. 17).

Calkins, Hugh et al. (Apr. 2012). "2012 HRS/EHRA/ECAS Expert Consensus Statement on Catheter and Surgical Ablation of Atrial Fibrillation: recommendations for patient selection, procedural techniques, patient management and follow-up, definitions, endpoints, and research trial design." eng. In: *Europace* 14.4, pp. 528–606 (cit. on p. 22).

Campos, Fernando O., Anton J. Prassl, et al. (May 2012). "Influence of ischemic core muscle fibers on surface depolarization potentials in superfused cardiac tissue preparations: a simulation study." eng. In: *Med Biol Eng Comput* 50.5, pp. 461–472 (cit. on p. 40).

Campos, Fernando, Thomas Wiener, et al. (Apr. 2013). "Electro-Anatomical Characterization of Atrial Microfibrosis in a Histologically Detailed Computer Model." eng. In: *IEEE Trans Biomed Eng* (cit. on p. 80).

Clayton, Richard H. and Peter Taggart (2005). "Regional differences in APD restitution can initiate wavebreak and re-entry in cardiac tissue: a computational study." eng. In: *Biomed Eng Online* 4, p. 54 (cit. on p. 77).

Crozatier, B. (July 1996). "Stretch-induced modifications of myocardial performance: from ventricular function to cellular and molecular mechanisms." eng. In: *Cardiovasc Res* 32.1, pp. 25–37 (cit. on p. 7).

de Bakker, Jacques M T. and Fred H M. Wittkampf (Apr. 2010). "The pathophysiologic basis of fractionated and complex electrograms and the impact of recording techniques on their detection and interpretation." eng. In: *Circ Arrhythm Electrophysiol* 3.2, pp. 204–213 (cit. on pp. 15, 22, 73, 74).

de Jong, Sanne et al. (June 2011). "Fibrosis and cardiac arrhythmias." eng. In: *J Cardiovasc Pharmacol* 57.6, pp. 630–638 (cit. on p. 74).

DiFrancesco, Dario (Feb. 2010). "The role of the funny current in pacemaker activity." eng. In: *Circ Res* 106.3, pp. 434–446 (cit. on p. 13).

Efimov, Igor R. et al. (July 2004). "Optical imaging of the heart." eng. In: *Circ Res* 95.1, pp. 21–33 (cit. on p. 15).

EHRA et al. (Oct. 2010). "Guidelines for the management of atrial fibrillation: the Task Force for the Management of Atrial Fibrillation of the European Society of Cardiology (ESC)." eng. In: *Europace* 12.10, pp. 1360–1420 (cit. on p. 1).

Epstein, A. E. et al. (Oct. 1998). "Gross and microscopic pathological changes associated with nonthoracotomy implantable defibrillator leads." eng. In: *Circulation* 98.15, pp. 1517–1524 (cit. on p. 79).

Fedorov, Vadim V., William J. Hucker, et al. (Aug. 2006). "Postganglionic nerve stimulation induces temporal inhibition of excitability in rabbit sinoatrial node." eng. In: *Am J Physiol Heart Circ Physiol* 291.2, H612–H623 (cit. on p. 77).

Fedorov, Vadim V., Richard B. Schuessler, et al. (Apr. 2009). "Structural and functional evidence for discrete exit pathways that connect the canine sinoatrial node and atria." eng. In: *Circ Res* 104.7, pp. 915–923 (cit. on pp. 68, 75).

Feng, J. et al. (Sept. 1998). "Ionic mechanisms of regional action potential heterogeneity in the canine right atrium." eng. In: *Circ Res* 83.5, pp. 541–551 (cit. on p. 24).

Franz, M. R. (Jan. 1999). "Current status of monophasic action potential recording: theories, measurements and interpretations." eng. In: *Cardiovasc Res* 41.1, pp. 25–40 (cit. on p. 78).

Gami, Apoor S. et al. (Feb. 2010). "Electrophysiological anatomy of typical atrial flutter: the posterior boundary and causes for difficulty with ablation." eng. In: *J Cardiovasc Electrophysiol* 21.2, pp. 144–149 (cit. on pp. 17, 18).

Goldstein, S. S. and W. Rall (Oct. 1974). "Changes of action potential shape and velocity for changing core conductor geometry." eng. In: *Biophys J* 14.10, pp. 731–757 (cit. on p. 11).

Grant, Augustus O. (Apr. 2009). "Cardiac ion channels." eng. In: *Circ Arrhythm Electrophysiol* 2.2, pp. 185–194 (cit. on p. 8).

Hagiwara, N. et al. (Oct. 1992). "Stretch-activated anion currents of rabbit cardiac myocytes." eng. In: *J Physiol* 456, pp. 285–302 (cit. on p. 7).

Ho, Siew Yen et al. (May 2002). "Atrial structure and fibres: morphologic bases of atrial conduction." eng. In: *Cardiovasc Res* 54.2, pp. 325–336 (cit. on p. 71).

Hofer, E., F. Keplinger, et al. (June 2006). "A new floating sensor array to detect electric near fields of beating heart preparations." eng. In: *Biosens Bioelectron* 21.12, pp. 2232–2239 (cit. on p. 20).

Hofer, E., T. Wiener, et al. (2011). "A novel transillumination device allows improved resolution in reconstruction of surface electrode positions with cardiac tissue topology." In: *Proceedings of the 45th annual conference of the german society of biomedical engineering* (cit. on p. 28).

Hoyt, R. H. et al. (Mar. 1989). "Distribution and three-dimensional structure of intercellular junctions in canine myocardium." eng. In: *Circ Res* 64.3, pp. 563–574 (cit. on p. 12).

Jacquemet, Vincent and Craig S. Henriquez (June 2009). "Genesis of complex fractionated atrial electrograms in zones of slow conduction: a computer model of microfibrosis." eng. In: *Heart Rhythm* 6.6, pp. 803–810 (cit. on pp. 22, 23, 74).

Li-jun, Jin et al. (Mar. 2012). "Electrophysiologic characteristics of the Crista terminalis and implications on atrial tachycardia in rabbits." eng. In: *Cell Biochem Biophys* 62.2, pp. 267–271 (cit. on p. 75).

Kalb, Soma S. et al. (June 2004). "The restitution portrait: a new method for investigating rate-dependent restitution." eng. In: *J Cardiovasc Electrophysiol* 15.6, pp. 698–709 (cit. on pp. 77, 78).

Kléber, A. G. and Y. Rudy (Apr. 2004). "Basic mechanisms of cardiac impulse propagation and associated arrhythmias." eng. In: *Physiol Rev* 84.2, pp. 431–488 (cit. on pp. 11, 12).

Kucera, J. P. et al. (Oct. 1998). "Slow conduction in cardiac tissue, II: effects of branching tissue geometry." eng. In: *Circ Res* 83.8, pp. 795–805 (cit. on p. 73).

Lakatta, Edward G. and Dario DiFrancesco (Aug. 2009). "What keeps us ticking: a funny current, a calcium clock, or both?" eng. In: *J Mol Cell Cardiol* 47.2, pp. 157–170 (cit. on p. 13).

Lang, Di et al. (2011). "Spatiotemporal control of heart rate in a rabbit heart." eng. In: *J Electrocardiol* 44.6, pp. 626–634 (cit. on p. 77).

Larsen, Anders Peter et al. (Sept. 2012). "The voltage-sensitive dye di-4-ANEPPS slows conduction velocity in isolated guinea pig hearts." eng. In: *Heart Rhythm* 9.9, pp. 1493–1500 (cit. on p. 15).

Lavallée, M. et al. (1969). *Glass Microelectrodes*. Wiley (cit. on p. 14).

Lynch, Patrick J. and C. Carl Jaffe (2007). *RLS 12blauLeg.png*. URL: `http://commons.wikimedia.org/wiki/File:RLS_12blauLeg.png` (visited on 02/15/2013) (cit. on p. 14).

Maltsev, Victor A. and Edward G. Lakatta (Jan. 2008). "Dynamic interactions of an intracellular Ca2+ clock and membrane ion channel clock underlie robust initiation and regulation of cardiac pacemaker function." eng. In: *Cardiovasc Res* 77.2, pp. 274–284 (cit. on p. 13).

MathWorks. *boxplot*. URL: `http://www.mathworks.de/de/help/stats/boxplot.html` (visited on 04/20/2013) (cit. on p. 31).

Monfredi, Oliver et al. (Nov. 2010). "The anatomy and physiology of the sinoatrial node–a contemporary review." eng. In: *Pacing Clin Electrophysiol* 33.11, pp. 1392–1406 (cit. on pp. 10, 13).

Nattel, Stanley et al. (Apr. 2008). "Atrial remodeling and atrial fibrillation: mechanisms and implications." eng. In: *Circ Arrhythm Electrophysiol* 1.1, pp. 62–73 (cit. on p. 72).

Oppenheim, A.V. et al. (1999). *Discrete-Time Signal Processing*. 2nd ed. Prentice-Hall, Inc. (cit. on p. 24).

Pastore, Joseph M. et al. (June 2006). "Importance of spatiotemporal heterogeneity of cellular restitution in mechanism of arrhythmogenic discordant alternans." eng. In: *Heart Rhythm* 3.6, pp. 711–719 (cit. on p. 77).

Pérez, Francisco J. et al. (Aug. 2009). "Long-term outcomes after catheter ablation of cavo-tricuspid isthmus dependent atrial flutter: a meta-analysis." eng. In: *Circ Arrhythm Electrophysiol* 2.4, pp. 393–401 (cit. on p. 17).

Plank, G. and E. Hofer (2000). "Model study of vector-loop morphology during electrical mapping of microscopic conduction in cardiac tissue." eng. In: *Ann Biomed Eng* 28.10, pp. 1244–1252 (cit. on pp. 20, 22).

Plank, G., E. J. Vigmond, et al. (Nov. 2003). "Cardiac near-field morphology during conduction around a microscopic obstacle–a computer simulation study." eng. In: *Ann Biomed Eng* 31.10, pp. 1206–1212 (cit. on p. 23).

Rohr, S., J. P. Kucera, et al. (Oct. 1998). "Slow conduction in cardiac tissue, I: effects of a reduction of excitability versus a reduction of electrical coupling on microconduction." eng. In: *Circ Res* 83.8, pp. 781–794 (cit. on p. 73).

Rohr, S. and B. M. Salzberg (Aug. 1994). "Characterization of impulse propagation at the microscopic level across geometrically defined expansions of excitable tissue: multiple site optical recording of transmembrane voltage (MSORTV) in patterned growth heart cell cultures." eng. In: *J Gen Physiol* 104.2, pp. 287–309 (cit. on p. 11).

Ruiz, Mariana (2006a). *Bluebaby syndrom.svg*. URL: `http://commons.wikimedia.org/wiki/File:Bluebaby_syndrom.svg` (visited on 08/03/2012) (cit. on p. 13).

Ruiz, Mariana (2006b). *Gap cell junction-en.svg*. URL: `http://commons.wikimedia.org/wiki/File:Gap_cell_junction-en.svg` (visited on 08/03/2012) (cit. on p. 10).

Ruiz, Mariana (2007). *Cell membrane detailed diagram en.svg*. URL: `http://commons.wikimedia.org/wiki/File:Cell_membrane_detailed_diagram_en.svg` (visited on 07/29/2012) (cit. on p. 6).

Sánchez-Quintana, D., R. H. Anderson, et al. (Oct. 2002). "The terminal crest: morphological features relevant to electrophysiology." eng. In: *Heart* 88.4, pp. 406–411 (cit. on p. 71).

Sánchez-Quintana, D., J. A. Cabrera, et al. (Feb. 2005). "Sinus node revisited in the era of electroanatomical mapping and catheter ablation." eng. In: *Heart* 91.2, pp. 189–194 (cit. on p. 13).

Schaffer, P. et al. (Apr. 1994). "Di-4-ANEPPS causes photodynamic damage to isolated cardiomyocytes." eng. In: *Pflugers Arch* 426.6, pp. 548–551 (cit. on p. 15).

Schmidt et al. (2000). *Physiologie des Menschen*. 28. Auflage. Springer-Verlag Berlin Heidelberg New York (cit. on p. 6).

Severs, Nicholas J. et al. (Oct. 2008). "Remodelling of gap junctions and connexin expression in diseased myocardium." eng. In: *Cardiovasc Res* 80.1, pp. 9–19 (cit. on p. 12).

Shih, H. T. (1994). "Anatomy of the action potential in the heart." eng. In: *Tex Heart Inst J* 21.1, pp. 30–41 (cit. on p. 10).

Sidorov, Veniamin Y. et al. (July 2011). "Regional increase of extracellular potassium leads to electrical instability and reentry occurrence through the spatial heterogeneity of APD restitution." eng. In: *Am J Physiol Heart Circ Physiol* 301.1, H209–H220 (cit. on p. 24).

Spach, M. S. and P. C. Dolber (Mar. 1986). "Relating extracellular potentials and their derivatives to anisotropic propagation at a microscopic level in human cardiac muscle.

Evidence for electrical uncoupling of side-to-side fiber connections with increasing age." eng. In: *Circ Res* 58.3, pp. 356–371 (cit. on p. 72).

Spach, M. S., J. F. Heidlage, et al. (Feb. 2000). "Electrophysiological effects of remodeling cardiac gap junctions and cell size: experimental and model studies of normal cardiac growth." eng. In: *Circ Res* 86.3, pp. 302–311 (cit. on p. 12).

Spach, M. S. and J. M. Kootsey (Oct. 1985). "Relating the sodium current and conductance to the shape of transmembrane and extracellular potentials by simulation: effects of propagation boundaries." eng. In: *IEEE Trans Biomed Eng* 32.10, pp. 743–755 (cit. on pp. 11, 16, 21).

Spach, M. S., WT Miller 3rd, et al. (Feb. 1982). "The functional role of structural complexities in the propagation of depolarization in the atrium of the dog. Cardiac conduction disturbances due to discontinuities of effective axial resistivity." eng. In: *Circ Res* 50.2, pp. 175–191 (cit. on p. 77).

Tanaka, Kazuhiko et al. (Oct. 2007). "Spatial distribution of fibrosis governs fibrillation wave dynamics in the posterior left atrium during heart failure." eng. In: *Circ Res* 101.8, pp. 839–847 (cit. on p. 80).

Ulbricht, Werner (Oct. 2005). "Sodium channel inactivation: molecular determinants and modulation." eng. In: *Physiol Rev* 85.4, pp. 1271–1301 (cit. on p. 10).

Valderrábano, Miguel (2007). "Influence of anisotropic conduction properties in the propagation of the cardiac action potential." eng. In: *Prog Biophys Mol Biol* 94.1-2, pp. 144–168 (cit. on p. 12).

Vigmond, E. J. et al. (May 2009). "Estimating atrial action potential duration from electrograms." eng. In: *IEEE Trans Biomed Eng* 56.5, pp. 1546–1555 (cit. on p. 16).

Walpole, Sarah Catherine et al. (2012). "The weight of nations: an estimation of adult human biomass." eng. In: *BMC Public Health* 12, p. 439 (cit. on p. 71).

Wang, Y. and Y. Rudy (Apr. 2000). "Action potential propagation in inhomogeneous cardiac tissue: safety factor considerations and ionic mechanism." eng. In: *Am J Physiol Heart Circ Physiol* 278.4, H1019–H1029 (cit. on p. 11).

Wang, Yves T., Igor R. Efimov, et al. (Aug. 2012). "Electroporation induced by internal defibrillation shock with and without recovery in intact rabbit hearts." eng. In: *Am J Physiol Heart Circ Physiol* 303.4, H439–H449 (cit. on p. 79).

Watanabe, Mari A. and Marcus L. Koller (Apr. 2002). "Mathematical analysis of dynamics of cardiac memory and accommodation: theory and experiment." eng. In: *Am J Physiol Heart Circ Physiol* 282.4, H1534–H1547 (cit. on p. 78).

Weiss, J. N., A. Garfinkel, et al. (June 1999). "Chaos and the transition to ventricular fibrillation: a new approach to antiarrhythmic drug evaluation." eng. In: *Circulation* 99.21, pp. 2819–2826 (cit. on p. 78).

Weiss, James N., Alain Karma, et al. (May 2006). "From pulsus to pulseless: the saga of cardiac alternans." eng. In: *Circ Res* 98.10, pp. 1244–1253 (cit. on p. 77).

Wiener, T. (2012). "Analysis of Cardiac Near Field Signals." PhD thesis. Graz University of Technology, Institute of Electrical Measurement and Measurement Signal Processing (cit. on pp. 16, 22, 23, 72).

Wiener, Thomas et al. (Oct. 2012). "Decomposition of fractionated local electrograms using an analytic signal model based on sigmoid functions." eng. In: *Biomed Tech (Berl)*, pp. 1–12 (cit. on p. 73).

Wilensky, R. L. et al. (Nov. 1986). "The subendocardial border zone during acute ischemia of the rabbit heart: an electrophysiologic, metabolic, and morphologic correlative study." eng. In: *Circulation* 74.5, pp. 1137–1146 (cit. on p. 40).

Wilson, Lance D. and David S. Rosenbaum (Nov. 2007). "Mechanisms of arrythmogenic cardiac alternans." eng. In: *Europace* 9 Suppl 6, pp. vi77–vi82 (cit. on p. 77).

Wu, T. J. et al. (Aug. 1998). "Role of pectinate muscle bundles in the generation and maintenance of intra-atrial reentry: potential implications for the mechanism of conversion between atrial fibrillation and atrial flutter." eng. In: *Circ Res* 83.4, pp. 448–462 (cit. on p. 72).

Zeng, T. et al. (Feb. 2000). "Stretch-activated whole cell currents in adult rat cardiac myocytes." eng. In: *Am J Physiol Heart Circ Physiol* 278.2, H548–H557 (cit. on p. 7).

Appendix

A.1. Tyrode's Solution

The nutrition solution used in this work contains (in $\mathrm{mmol\,l^{-1}}$):

Table A.1.: Tyrode solution

Substance	Concentration
$NaCl$	132.10
KCl	5.40
$CaCl_2$	2.50
$MgCl_2$	1.15
$NaHCO_3$	24.00
NaH_2PO_4	0.42
$D-glucose$	5.60

A.2. Glass Microelectrodes

Settings for DMZ-Universal Puller (Zeitz-Instruments, Munich, Germany) for pulling glass microelectrodes with $20-30\,\mathrm{M\Omega}$ resistance. Electrodes were filled with 2.5 M KCl solution.

Table A.2.: Settings

1^{st} stage:		
Heat	H	500
Force Preliminary Pull	F(TH)	040
Distance Threshold	s(H)	040
Adjust	AD	010
2^{nd} stage:		
Heat	H	500
Force Preliminary Pull	F(TH)	020
Distance Threshold	s(H)	012
Delay Heatstop	t(H)	100
Distance Heatstop	s(H)	000
Delay Pull 1	t(F1)	310
Force Pull 1	F1	400
Distance Pull 2	s(F2)	003
Force Pull 2	F2	700
Adjust	AD	000

A.3. Morphometry of ROI

Table A.3.: Areas within ROI. PectM, Pectinate Muscle; CT, Crista Terminalis; VB, Vestibule; NPT, non pectinate tissue; Weight, body weight.

CTI/mm^2	PectM/mm^2	CT+VB/mm^2	NPT/mm^2	Weight/kg
83.7	31.2	33.7	18.8	3.00
58.0	19.7	25.8	12.5	3.00
134.4	43.0	43.4	48.0	2.75
64.8	17.4	23.4	24.0	2.95
182.0	71.1	73.1	37.8	3.90
168.8	50.9	53.9	64.0	3.30
126.0	51.1	47.2	27.7	4.80
114.8	34.3	46.8	33.7	3.40
91.2	20.5	46.7	24.0	3.85
140.7	45.2	45.7	49.8	6.05
122.8	56.1	36.2	30.5	4.30
108.0	44.7	32.2	31.3	5.90
89.7	44.6	27.8	17.4	6.20
114.2 ± 35.7	40.8 ± 15.1	41.2 ± 13.0	32.2 ± 14.0	4.11 ± 1.20

Table A.4.: Length, diameter, and number of structures ($n_{segment}$) within the ROI. ILI, Inferolateral Isthmus; PSI, Paraseptal Isthmus; CT, Crista Terminalis; VB, Vestibule; PectMp, proximal; PectMc, central; PectMd, distal.

Lengths		Diameters		$n_{segment}$		
ILI/mm	PSI/mm	CT/mm	VB/mm	PectMp	PectMc	PectMd
17.4	7.4	1.9	2.6	9	8	4
11.3	4.9	1.4	1.8	3	6	3
16.2	7.2	1.3	3.3	9	9	5
11.5	5.4	2.1	1.7	7	5	4
18.7	8.8	2.5	3.3	4	6	4
17.6	8.7	2.3	3.3	4	8	4
12.6	6.9	1.5	1.9	4	12	6
15.1	4.7	1.8	2.3	4	7	5
13.7	8.2	1.7	2.9	3	4	2
15.4	10.9	1.6	2.8	2	7	3
15.2	9.0	1.2	1.6	1	7	6
14.7	8.0	1.1	2.7	4	10	3
13.5	5.4	1.6	1.4	4	11	4
14.8 ± 2.2	7.3 ± 1.8	1.7 ± 0.4	2.4 ± 0.7	4[1 9]	7[4 12]	4[2 6]

A.4. BCL in Atrial Tissue Preparations

BCL obtained from all recordings per experiment. Variation is large since animals were not selected from a narrow range of weight and age.

Table A.5.: Overview of BCL in atrial tissue preparations. All values are *mean* ± *std.*

BCL / ms	
Rabbit	**Guinea Pig**
514.23 ± 41.27	366.07 ± 13.84
434.75 ± 21.46	579.32 ± 74.74
397.83 ± 9.92	260.76 ± 125.62
390.03 ± 42.73	
356.42 ± 9.60	
575.48 ± 42.15	
631.89 ± 35.46	
351.72 ± 51.15	
365.42 ± 42.88	
826.89 ± 41.73	
462.11 ± 66.18	
354.51 ± 12.43	
350.23 ± 13.57	
536.95 ± 31.33	
261.61 ± 4.57	
358.65 ± 13.42	
306.56 ± 20.43	
349.05 ± 26.39	
422.31 ± 22.93	
$\mathbf{468.25 \pm 99.99}$	$\mathbf{366.34 \pm 170.80}$

A.5. Signals in Parts of ROI

Analysis of extracellular signal recordings obtained from different regions within CTI is shown in Figure A.1.

Analysis of extracellular signal recordings obtained from different sections within PectMs is shown in Figure A.2.

A.6. Occurence of conduction block in different species

Statistically significant differences of ERP were found between species only during ramp-like pacing protocols (Figure A.3).

Directional and species dependency of ERP shows significant differences only for antegrade application of ramp-like pacing protocols (Figure A.4).

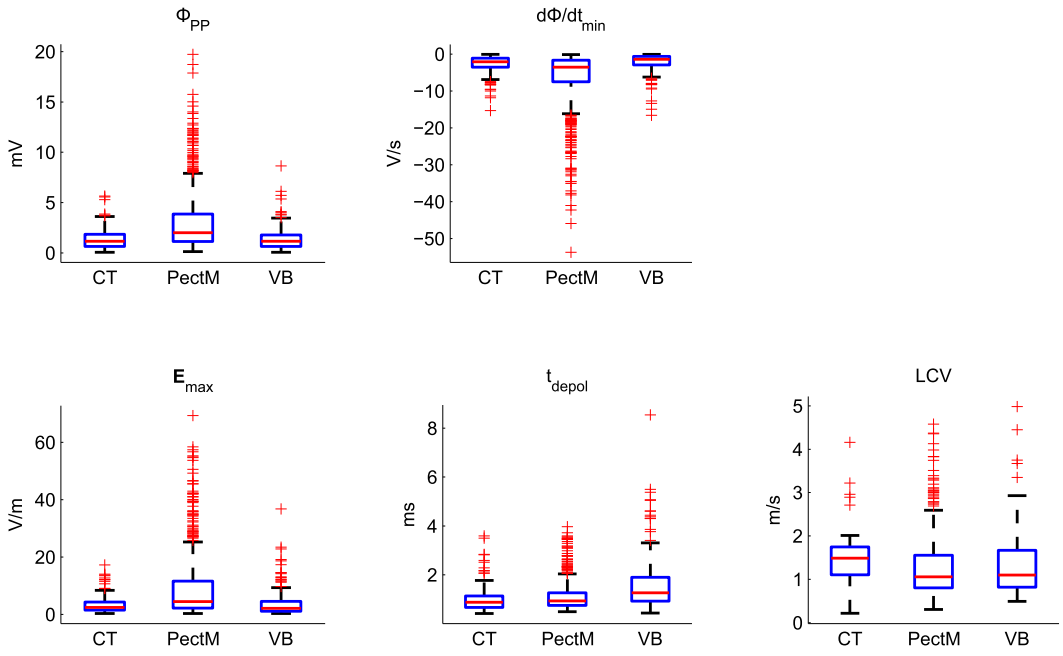

Figure A.1.: ROI parts

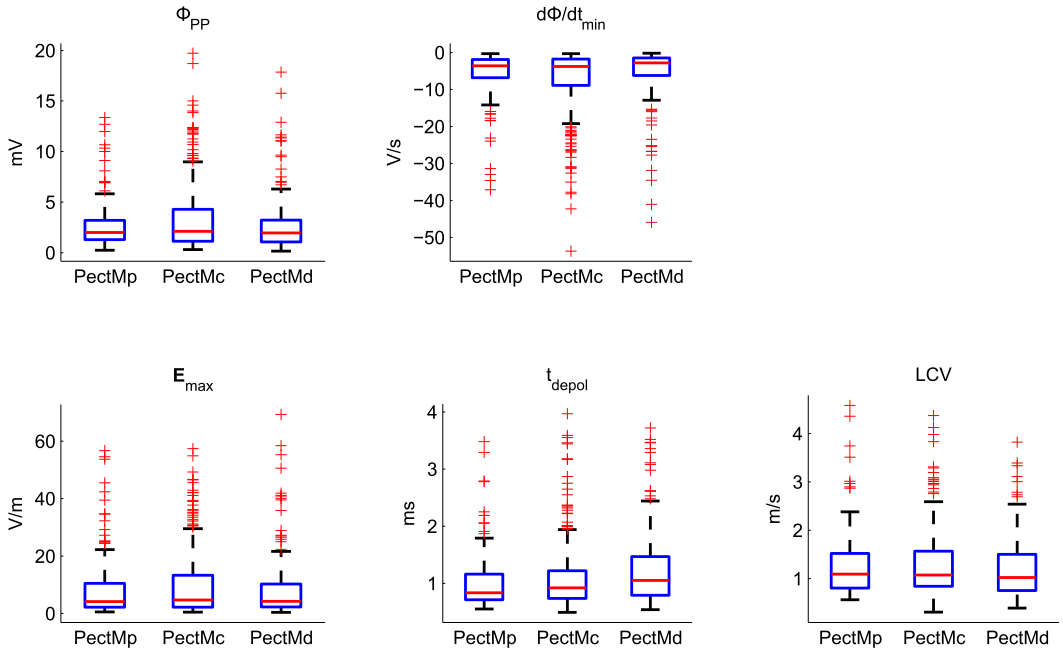

Figure A.2.: PM sections

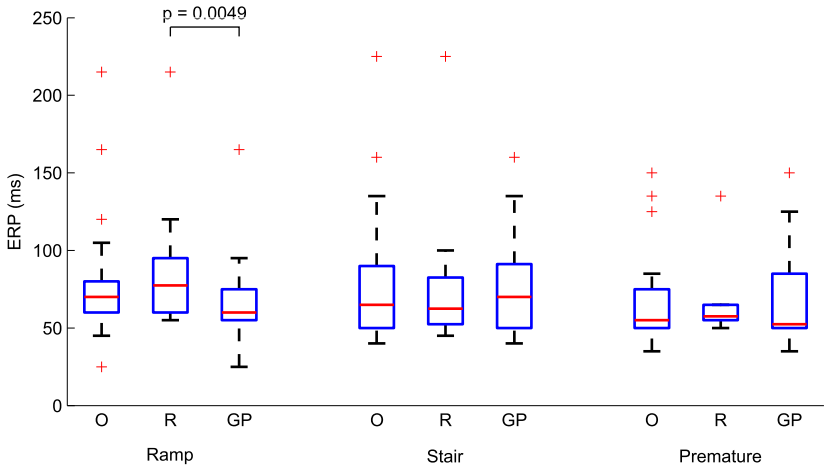

Figure A.3.: Occurrence of conduction block (ERP) in species. O, overall; R, rabbit; GP, guinea pig.

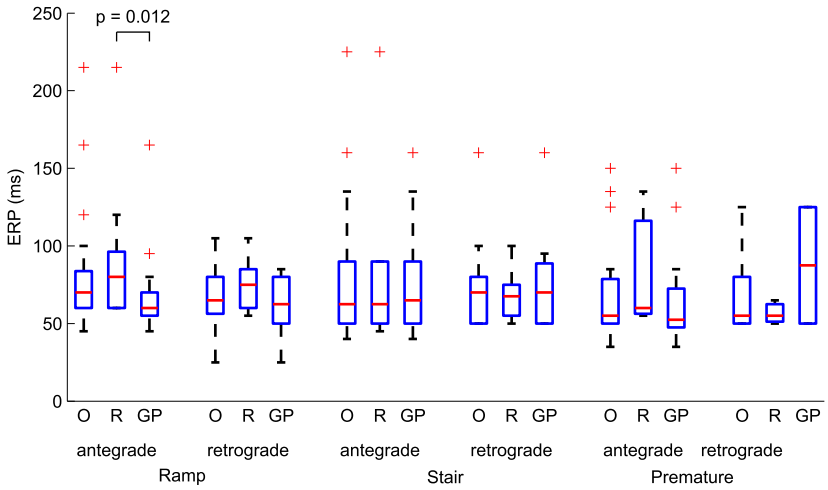

Figure A.4.: Directional and species dependence of ERP. O, overall; R, rabbit; GP, guinea pig.

A.7. Parameter Development of Pacing Protocols

A.7.1. Ramp-like Pacing Protocols

For better readability plots in results were shown without outliers (for definition of outliers see Section 3.7). Figure A.5 shows the same plot as in Figure 6.4a but with outliers included.

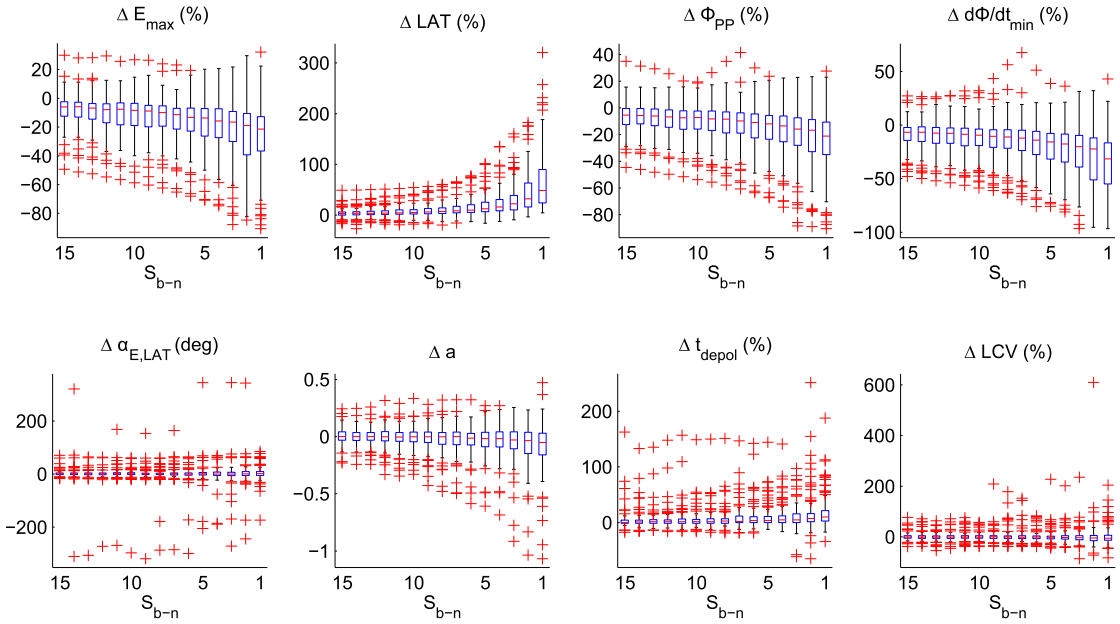

Figure A.5.: Non-linear parameter development during ramp-like pacing protocols. Original plot with outliers.

Parameter development was analyzed separately for species:
Development of extracellular parameters obtained from rabbit tissue is shown in Figure A.6. Significance matrix of pre-block behavior from rabbit tissue is shown in Figure A.7.
Development of extracellular parameters obtained from rabbit tissue is shown in Figure A.8. Significance matrix of pre-block behavior from rabbit tissue is shown in Figure A.9.

A.7.2. Stair-like Pacing Protocols

Development of alternans amplitude obtained from rabbit tissue is shown in Figure A.10 and from guinea pig tissue in Figure A.11.

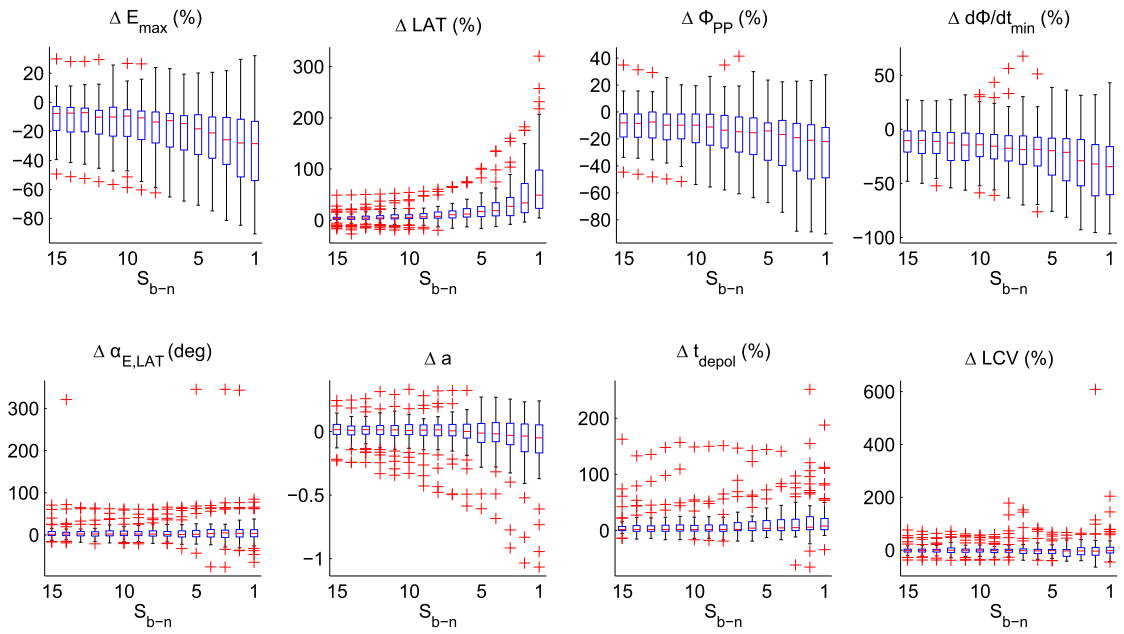

Figure A.6.: Non-linear parameter development during ramp-like pacing protocols in rabbit tissue. Original plot with outliers.

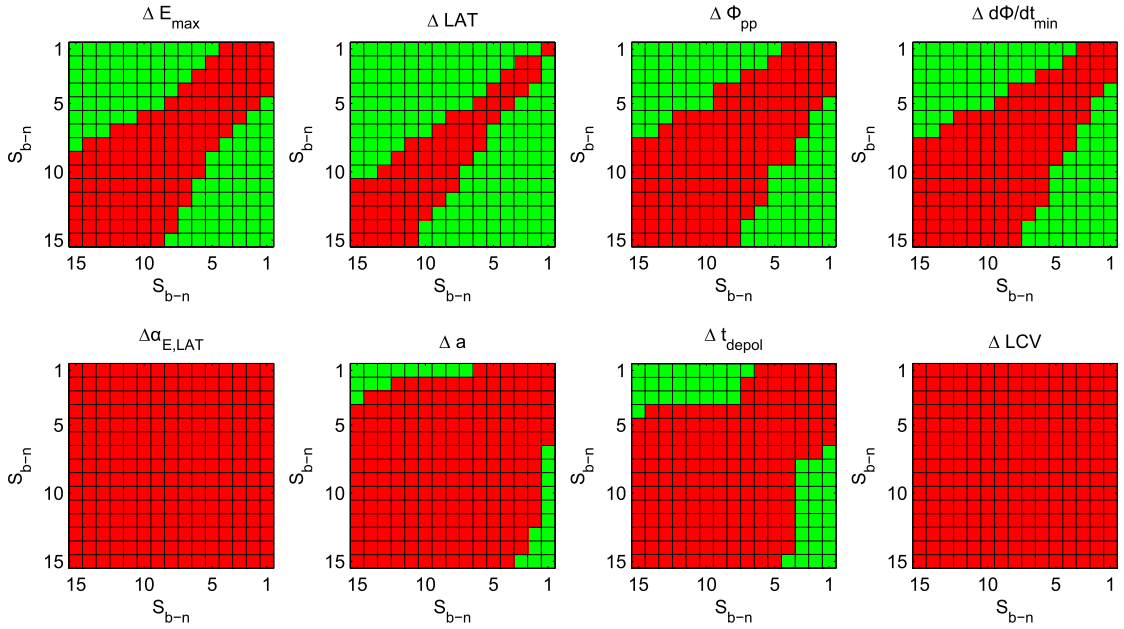

Figure A.7.: Significance matrix of pre-block beats during ramp-like pacing protocols in rabbit tissue.

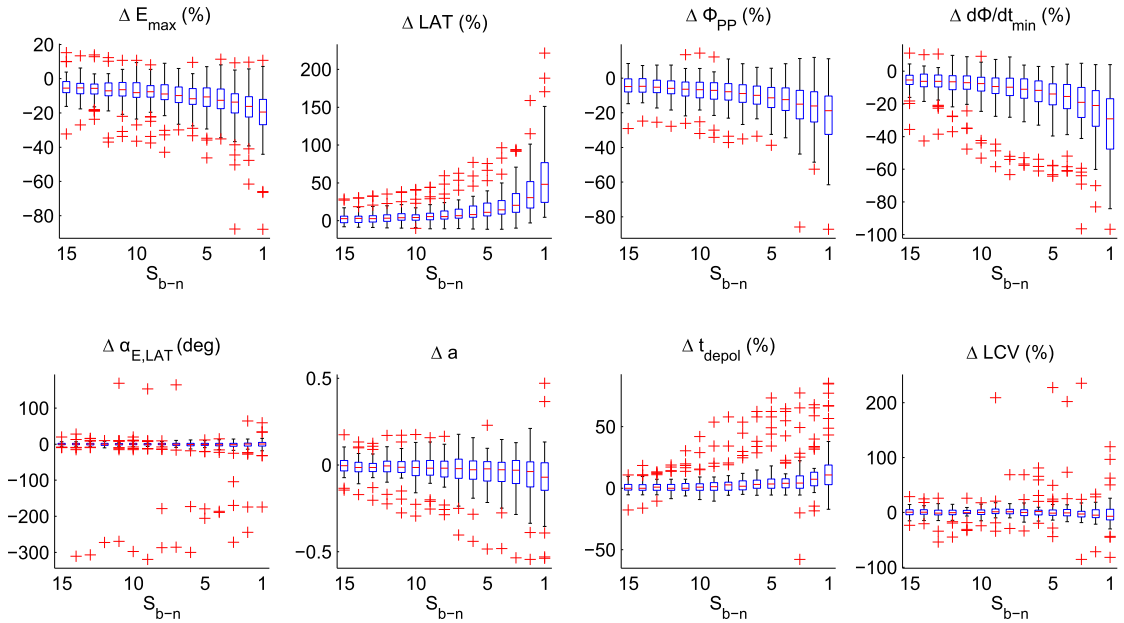

Figure A.8.: Non-linear parameter development during ramp-like pacing protocols in guinea pig tissue. Original plot with outliers.

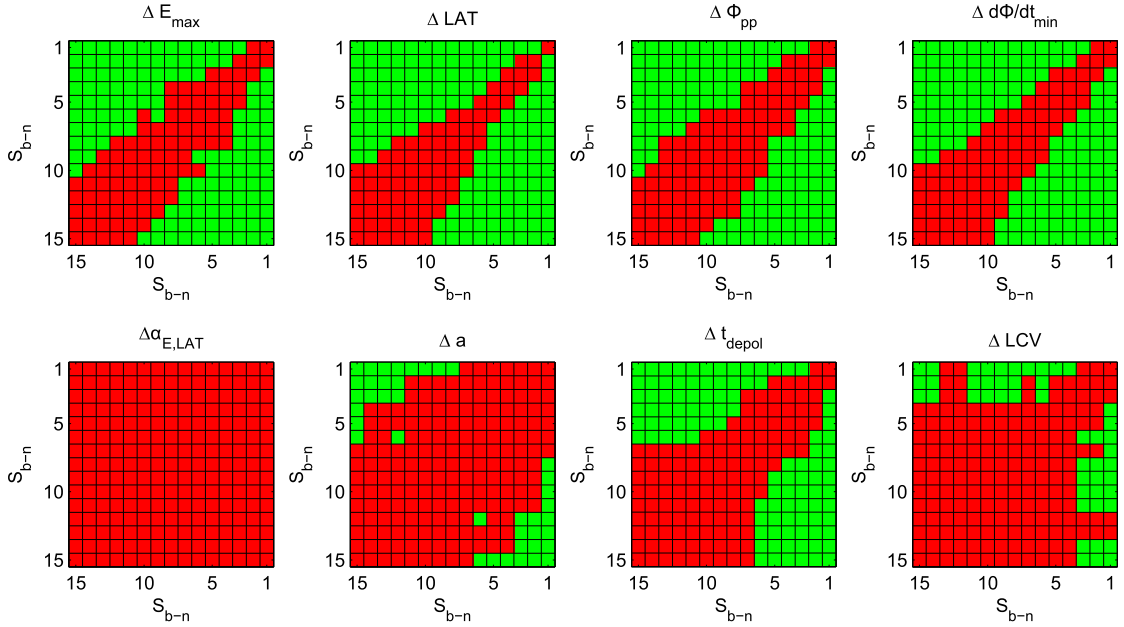

Figure A.9.: Significance matrix of pre-block beats during ramp-like pacing protocols in guinea pig tissue.

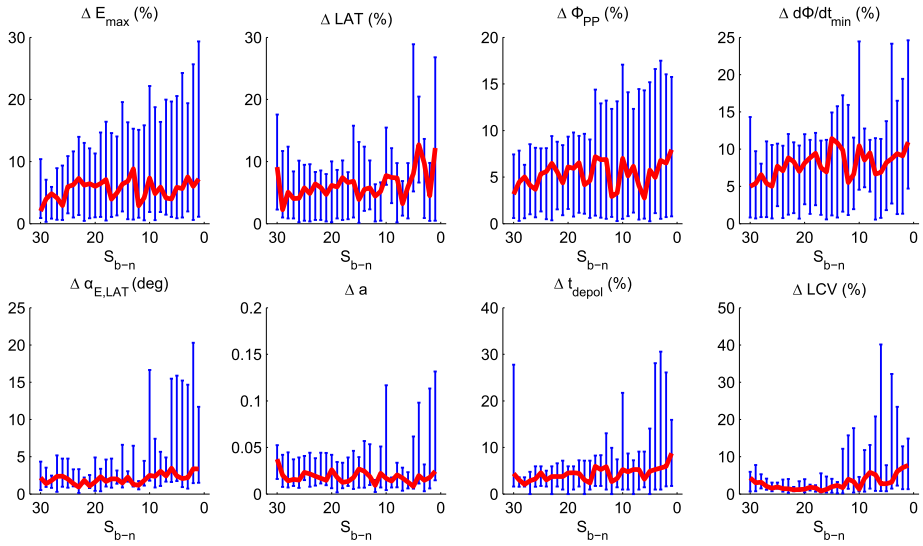

Figure A.10.: Alternans amplitude during stair-like pacing protocols in rabbit tissue.

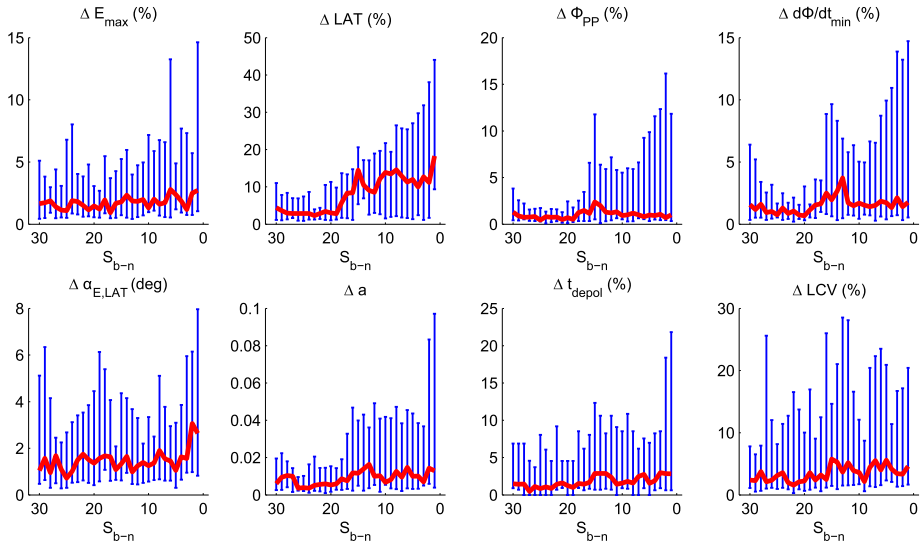

Figure A.11.: Alternans amplitude during stair-like pacing protocols in guinea pig tissue.

A.7.3. Premature beat Pacing Protocols

For better readability plots in results were shown without outliers (for definition of outliers see Section 3.7). Figure A.5 shows the same plot as in Figure 6.10a but with outliers included.

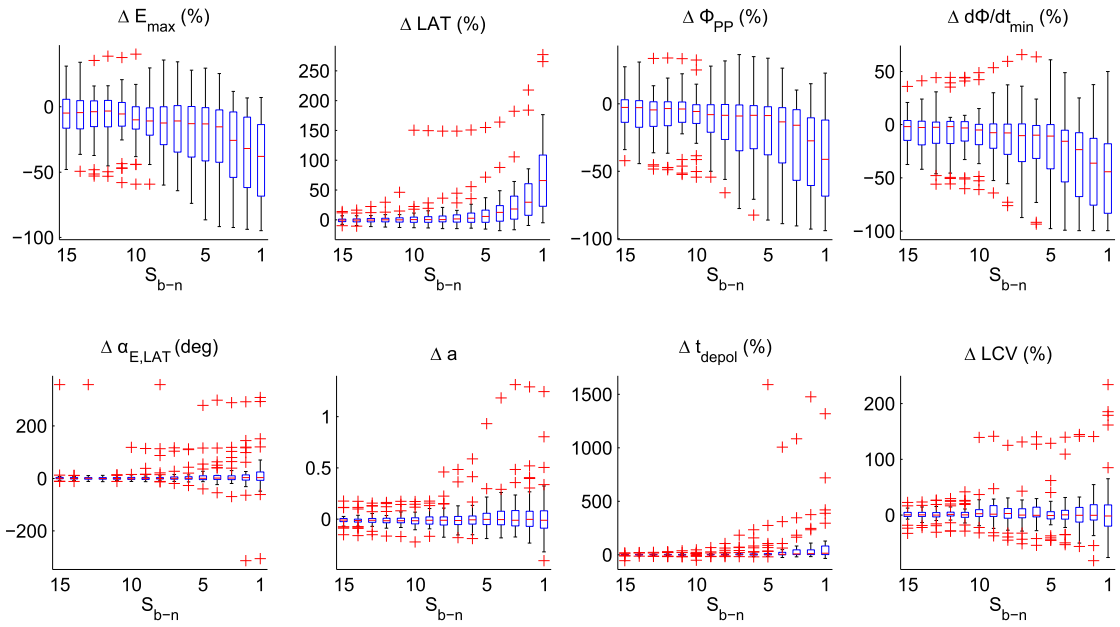

Figure A.12.: Non-linear parameter development during ramp-like pacing protocols. Original plot with outliers.

Parameter development was analyzed separately for species:
Development of extracellular parameters obtained from rabbit tissue is shown in Figure A.13. Significance matrix of pre-block behavior from rabbit tissue is shown in Figure A.14.
Development of extracellular parameters obtained from rabbit tissue is shown in Figure A.15. Significance matrix of pre-block behavior from rabbit tissue is shown in Figure A.16.

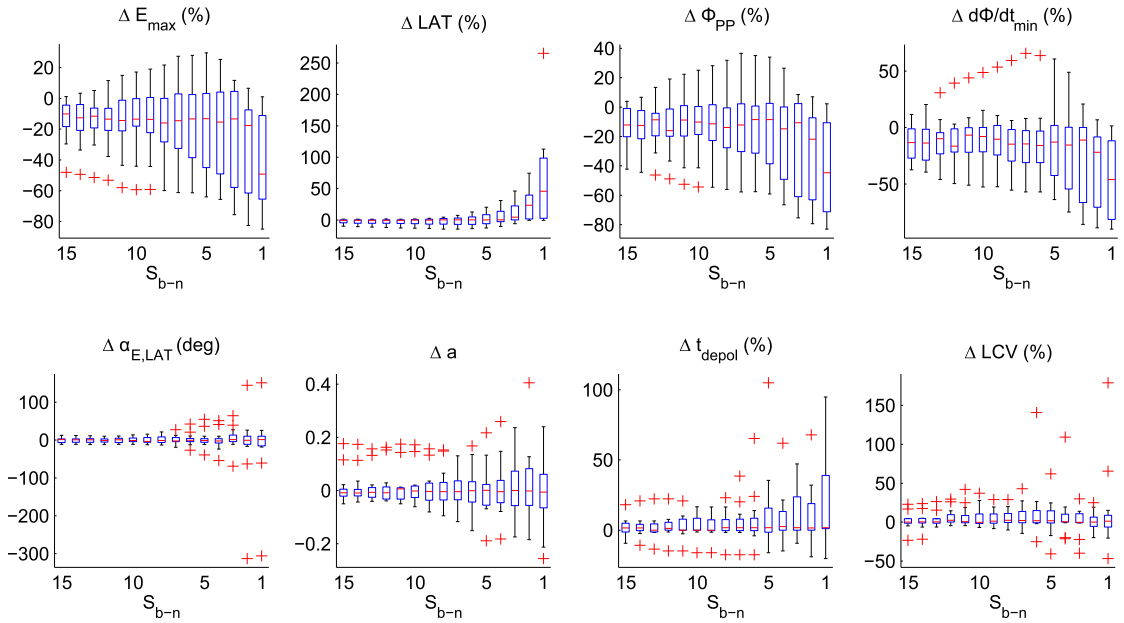

Figure A.13.: Non-linear parameter development during ramp-like pacing protocols in rabbit tissue. Original plot with outliers.

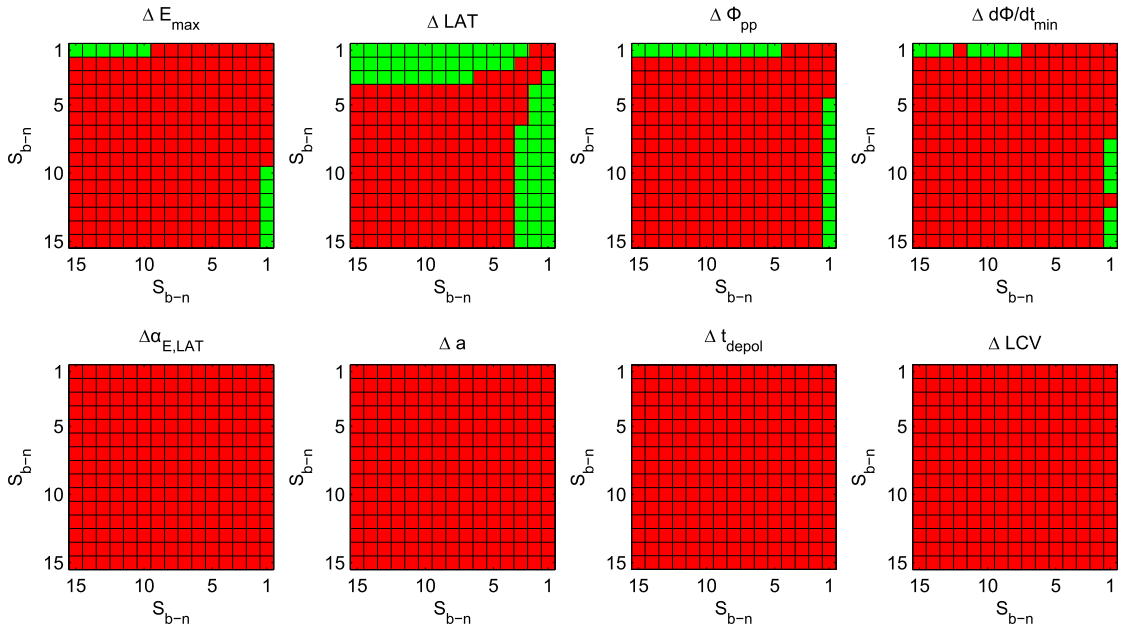

Figure A.14.: Significance matrix of pre-block beats during ramp-like pacing protocols in rabbit tissue.

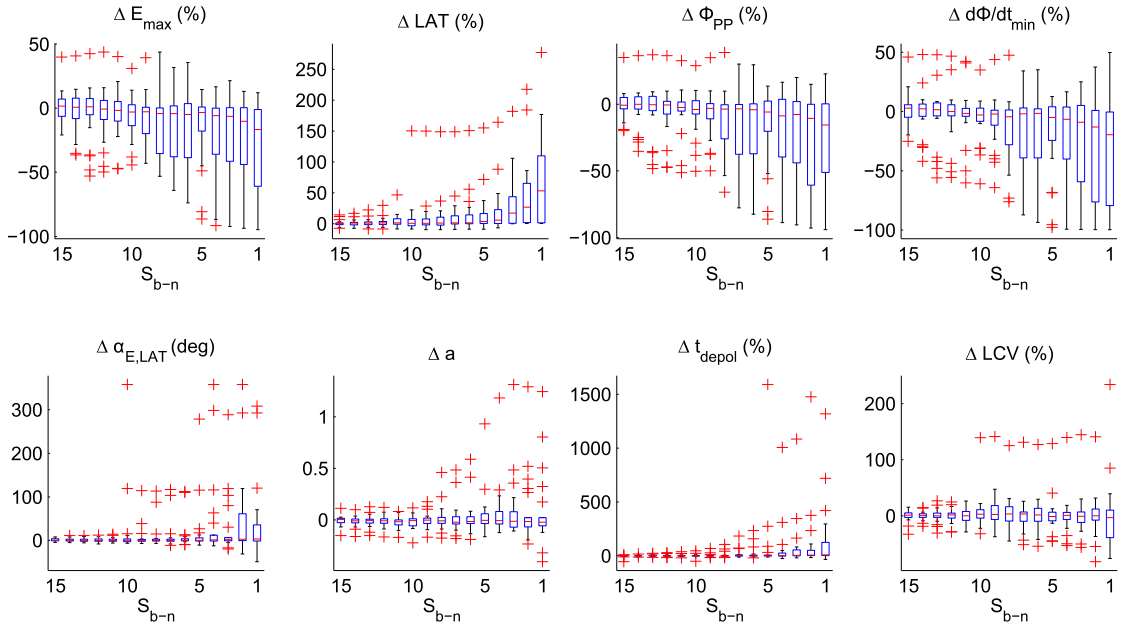

Figure A.15.: Non-linear parameter development during ramp-like pacing protocols in guinea pig tissue. Original plot with outliers.

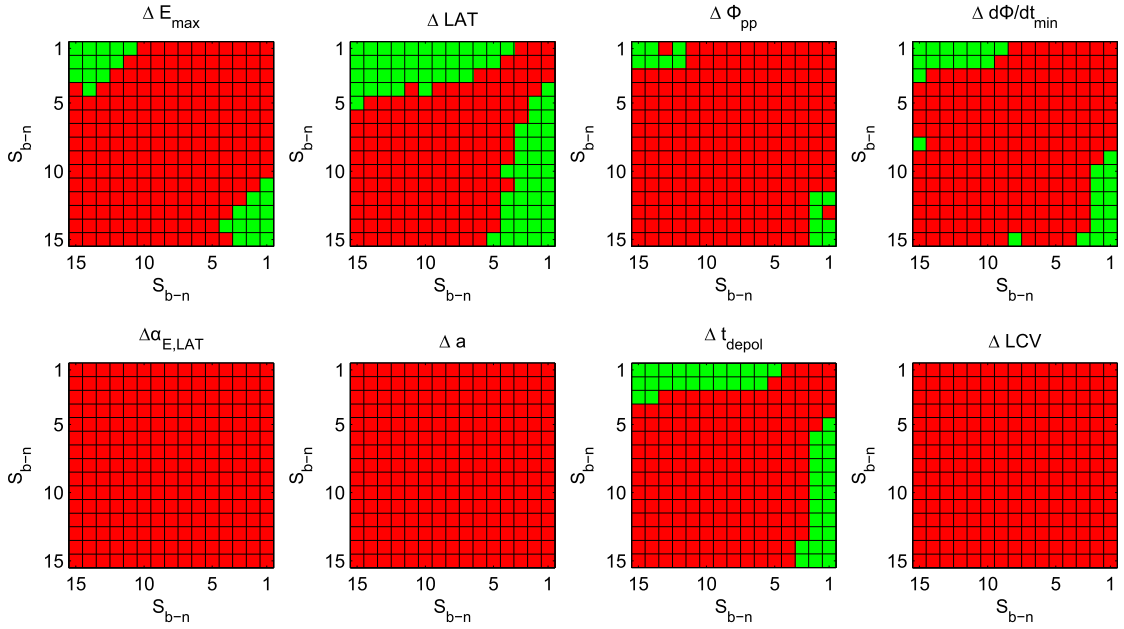

Figure A.16.: Significance matrix of pre-block beats during ramp-like pacing protocols in guinea pig tissue.